UNIVERSITÀ
DEGLI STUDI
DI PADOVA

Head Office: Università degli Studi di Padova

Department of Geosciences

_____

Ph.D. COURSE IN EARTH SCIENCES
SERIES XXX

Apatite (U-Th)/He and Fission Track thermochronometry
in the Northern Patagonian Andes:
New insights into the exhumation history of the thrust belt foreland sector

Coordinator: Ch.mo Prof. Fabrizio Nestola
Supervisor: Ch.mo Prof. Massimiliano Zattin
Co-Supervisor: Ch.mo Prof. Stefano Mazzoli
                    Prof. Marta Franchini

                    Ph.D. student: Elisa Savignano

TABLE OF CONTENTS

2

Abstract

The study of the Cretaceous–Cenozoic evolution of the North Patagonian Andes represents a great opportunity to investigate the effects of coupling between deep lithospheric processes and near-surface deformation. Despite the general along-strike continuity, this mountain belt is characterized by a pronounced internal tectonic segmentation (marked by the variable position of the magmatic arc and of the deformation front to the east). Thus, this plate margin results in a more complex configuration with respect to the simplified notion of "Andean-type" subduction system.

Being located in the retro-wedge of the Andes, this sector of the Southern Cordillera experienced a complex evolution characterized by alternating flat- and steep-slab subduction stages, which controlled shortening and extension episodes in the overriding plate. Furthermore, the deformation in this whole retroarc sector varied not only in time (i.e. with major 'cycles' of mountain building and orogenic collapse), but also in space, due to the variable transmission of horizontal compressive stress away from the orogen, that produced an irregular unroofing pattern, recorded by obtained low-temperature (low-T) thermochronometric ages. Indeed, low-T thermochronological systems are ideally suited for detecting events involving rocks in the uppermost part of the crust because they record time and rates of cooling related to exhumation of the top few kilometers of the crust.

In this study, apatite (U-Th)/He (AHe) and apatite fission track (AFT) dating are integrated with structural methods in the region located between 40° and 44°S. Two fieldwork periods were carried out throughout the Neuquén, Rio Negro, and Chubut Provinces in order to sample for thermochronological analyses and conduct structural surveys. These methods allowed us comparing the exhumation patterns both between the frontal part of the orogen and its adjacent foreland, and in the same morpho-structural domain at different latitudes.

A total of 48 samples have been collected, processed and analyzed. AHe dating was performed at the University of Paris Sud, while AFT dating was done at the University of Padua. Detailed structural surveys were mainly conducted in the less studied zones of the foreland, and in the entire studied area to check major structures. Integrating the different methods allowed us to unravel the complex tectonic scenario characterizing the study

area. Three balanced and sequentially restored cross-sections have been integrated with thermochronological information in order to produce a thermo-kinematic model along two different transects located at 40° and 42°S. To do this, the analyzed transects were processed with FetKin, a dedicated software for forward modeling of thermochronometric ages and age prediction along the present-day profile. This in turn, was used to validate the proposed tectonic scenario. New AFT and AHe data obtained in this study highlight two major tectonic events that occurred in North Patagonia: a Late Cretaceous to Paleogene inversion and exhumation stage, that involved the entire fold-and-thrust belt–foreland basin system, and a Miocene-Pliocene inversion stage of focused exhumation in the Andean fold-and-thrust belt. The suggested tectonic scenario was successfully tested with FetKin along the two transects, allowing us to unravel the role and extent of each tectonic stage that occurred since the Mesozoic.

The recorded pattern may be interpreted as the result of a variable degree of propagation of the deformation from the Andean chain to the foreland. This appears to be controlled by two main parameters: (i) slab configuration (i.e. steep- vs. flat-subduction, which plays a fundamental role in foreland deformation), and (ii) convergence rate between the Pacific and South-America plates, which rules shortening and exhumation processes in the fold-and-thrust belt.

Riassunto

Lo studio dell'evoluzione Cretacico–Cenozoica delle Ande Nord Patagoniche offre l'opportunità di comprendere le relazioni intercorrenti tra processi profondi riguardanti la dinamica della litosfera e la deformazione più superficiale che coinvolge la crosta. Benché la catena andina sia caratterizzata da un generale andamento lineare nord-sud, nel dettaglio essa è fortemente segmentata da un punto di vista tettonico, come si evince dalla posizione variabile dell'arco magmatico e del fronte di deformazione verso le zone di avampaese. Pertanto, questo margine di placca risulta avere una complessa configurazione, che va oltre la comune nozione di sistema di subduzione di "tipo andino". Localizzato nella zona di retrocatena, il settore Nord Patagonico della Cordigliera ha subito una complessa evoluzione, caratterizzata dall'alternanza di fasi di subduzione a basso e alto angolo, che ha controllato le fasi rispettivamente di raccorciamento e di estensione in corrispondenza della placca superiore. La variabilità deformativa in questa zona di retroarco è stata sia temporale—dunque legata a fasi di orogenesi e collasso della catena—sia spaziale, data la variabile trasmissione dello stress compressivo verso le zone esterne dell'orogene.

La termocronologia di bassa temperatura è in grado di registrare i pattern irregolari di denudamento risultanti, essendo molto sensibile alle variazioni entro i primi chilometri della crosta. Tali sistemi termocronometrici sono ideali per identificare eventi tettonici a livello crostale, poiché sono in grado di registrare il momento e la velocità del raffreddamento legato all'esumazione. In particolare, i metodi (U-Th)/He (AHe) e tracce di fissione (AFT), entrambi su apatite, sono stati integrati in questa tesi con i metodi strutturali.

L'area investigata è la regione ubicata tra 40° and 44°S, nel nord della Patagonia argentina. Durante le due campagne, condotte nelle Province di Neuquén, di Rio Negro e del Chubut, sono state campionate le rocce sulle quali compiere le analisi termocronologiche di bassa temperatura e sono stati analizzati dal punto di vista strutturale i lineamenti tettonici più importanti. Questi metodi hanno permesso sia di comparare i pattern di esumazione nella parte frontale della catena e nell'adiacente avampaese sia, al contempo, di comparare le differenze, a diverse latitudini, all'interno di uno stesso dominio morfo-strutturale.

Complessivamente, sono stati raccolti, processati e analizzati quarantotto campioni. Le analisi (U-Th)/He sono state eseguite presso l'Università di Parigi Sud mentre quelle di tracce di fissione presso l'Università di Padova.

Dal punto di vista geologico-strutturale, le maggiori strutture dell'area di studio sono state rilevate sul terreno e analizzate nel dettaglio, con particolare attenzione nelle zone meno studiate dell'avampaese. Infine, per un'analisi più approfondita di questo complesso scenario i due metodi sono stati integrati. Infatti, sono state costruite tre sezioni bilanciate e retrodeformate integrate con le informazioni termocronologiche al fine di produrre un modello termo-cinematico lungo due diversi transetti posti a 40° e 44°S, mediante l'utilizzo di un software dedicato in grado di modellare le età termocronometriche e fare previsione di queste lungo il profilo topografico odierno, che, a sua volta, è stato usato per validare lo scenario tettonico proposto. I nuovi dati AFT e AHe ottenuti nell'area di studio evidenziano due eventi tettonici principali interessanti l'area settentrionale della Patagonia: una fase d'inversione ed esumazione tra il tardo Cretacico e il Paleogene, che ha coinvolto l'intero sistema dalla catena all'avampaese, e una successiva, Mio-Pliocenica, in cui l'esumazione si è concentrata nella zona di catena. Questo scenario tettonico proposto è stato con successo testato lungo i due transetti analizzati attraverso FetKin, permettendo di chiarire il ruolo e l'entità di ogni fase tettonica avvenuta dal Mesozoico.

Il pattern di esumazione così ottenuto è stato interpretato come il risultato del variabile grado di propagazione della deformazione dalla catena andina verso l'avampaese. Quest'ultimo sembra essere controllato principalmente da due parametri: (i) la configurazione della placca in subduzione, in altre parole la sua geometria più o meno orizzontale che gioca un ruolo fondamentale nella deformazione dell'avampaese, e (ii) la velocità di convergenza tra le placche pacifica e sud americana, che governa i processi di raccorciamento ed esumazione nella catena a pieghe e sovrascorrimenti.

Chapter 1

Introduction

1.1 Overview

The presented work is aimed to reconstruct the Meso-Cenozoic exhumation history of the North Patagonian fold-and-thrust belt and its adjacent foreland.

In this chapter an introduction to the geodynamic framework of the Southern Andes is provided highlighting the main scientific open question of this region. In the last paragraphs the main goals of the thesis are exposed and the structure of the thesis is briefly outlined.

1.2 Geological framework

The Southern Andes of Central Argentina and Chile (also known as Northern Patagonia) are a mostly linear orogenic belt which has been formed by the subduction of several Pacific plates (Nazca and Antarctic plate in the nowadays configuration) beneath the South American Plate. This process is documented to have been started after the generalized rift stage that occurred in conjunction with the opening of the Atlantic Ocean and the formation of several basins in the interior during the Jurassic (Franzese et al., 2003). This mountain belt appears to be morphologically continuous along its strike for more than 4000 km and, thus, is often used to explain how the "simple" mountain building at subducting plate boundaries works (Dewey and Bird, 1970; James, 1971). Since the works of Jordan et al. (1983) an internal tectonic segmentation has been recognized at different sectors of latitudes. Considering the Southern Andes, in fact, at least six-separated fold-and-thrust belt are distinguishable in the main Andean axis, even characterized by temporal variation in their growth (Folguera and Ramos, 2011). Moreover, also the position of the magmatic arc is differentially eastward shifted at different latitudes (Folguera and Ramos, 2011).
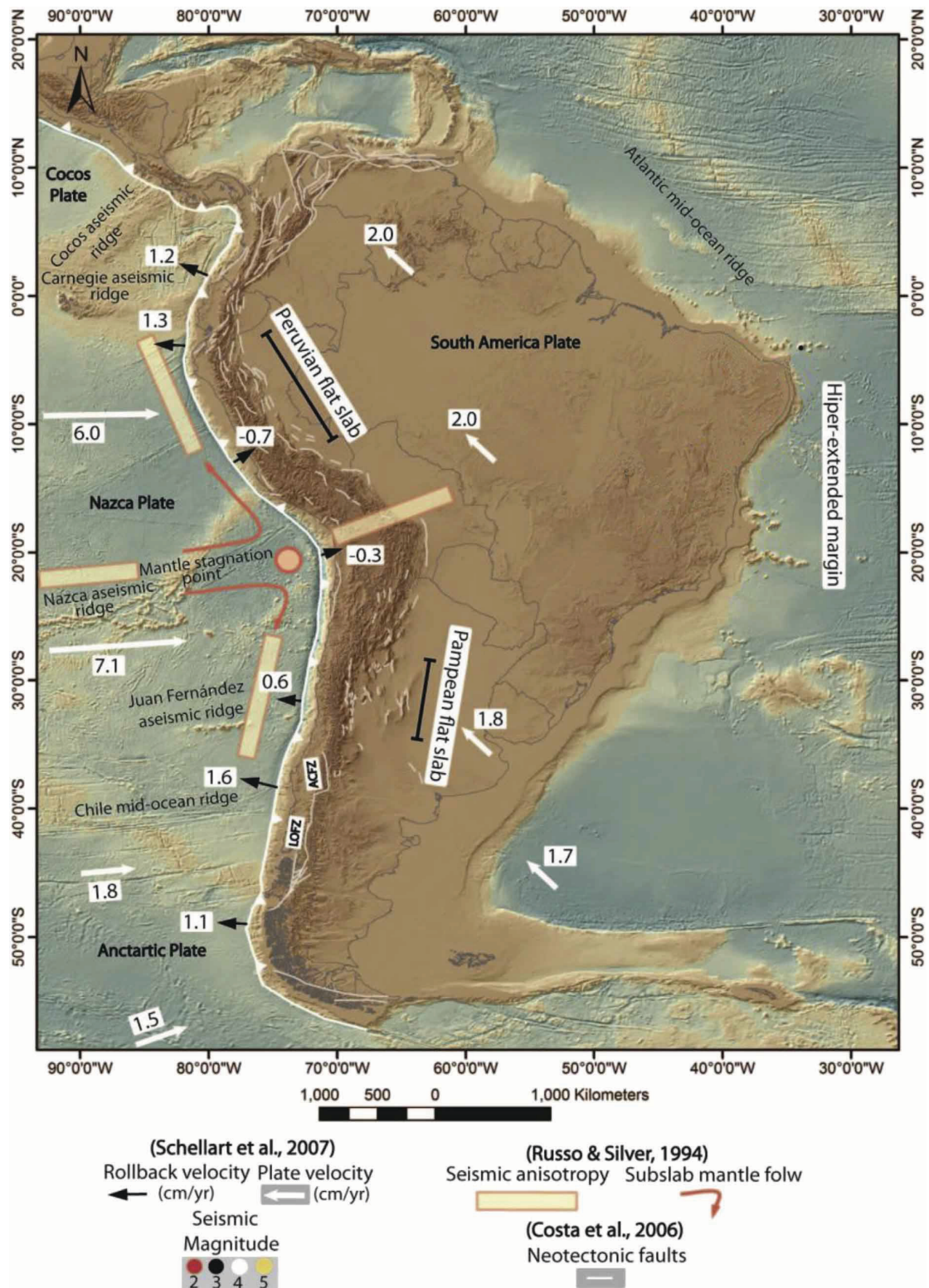
Figure 1.1 – Present-day mechanisms associated with deformation and regional uplift in the Central and Southern Andes. In the figure is possible to note the maximum amplitude of the Andean orogen in the correspondence of the Altiplano region, that correlate with the position of stationary trench; north and south of this region two flat slabs regions characterized by thick-skinned deformation in the foreland are marked (modified from Folguera et al., 2015).

These present-day spatial upper plate variations have been related to the subduction angle of the lower plate (Figure 1.1), which has been recognized studying the seismic distribution (Gütscher et al., 2000). However, their identification in past times requires detailed observations on a number of geologic processes, such as the evolution of sedimentary basins, cycles of magmatism from extensional to compressional regimes, exhumation and mountain building. On the basis of the distribution of magmatic bodies in the interior of the Argentina, several past flat segments have been hypothesized (Figure 1.2; Ramos and Folguera, 2009; Folguera and Ramos, 2011).

Figure 1.2 – Cenozoic segments characterized by flat-slab geometries (Ramos and Folguera, 2011).

More in detail, the present-day setting of the Patagonian Andes is shown in Figure 1.3. One of the most prominent feature of this area is represented by the Chile Triple Junction (CTJ) that is the position (at latitude of 46°12'S) where the active South Chile spreading Ridge (Lagabrielle et al., 2004) is colliding with the active margin. It also represents the southern boundary of the Nazca Plate, which is characterized by a subduction angle of c. 25 - 30° (Barazangi and Isacks, 1976, Bohm et al., 2002) and an ENE direction of convergence beneath the South American Plate and a rate of ca. 66 mm/a (Angermann et al., 1999). In this sector the Liquiñe-Ofqui Fault Zone (LOFZ) is a major dextral transpressional intra-arc fault system (Figure 1.3) that accommodates this oblique convergence, occurring basically throughout the Cenozoic, and along which most of the Quaternary volcanism and faulting have been focused (Hervé, 1994; Cembrano et al., 1996; Rosenau et al., 2006; Vargas Easton et al., 2013). Differently, the Antarctic Plate is characterized by an almost perpendicular direction of subduction and minor rates (DeMets et al., 1994).
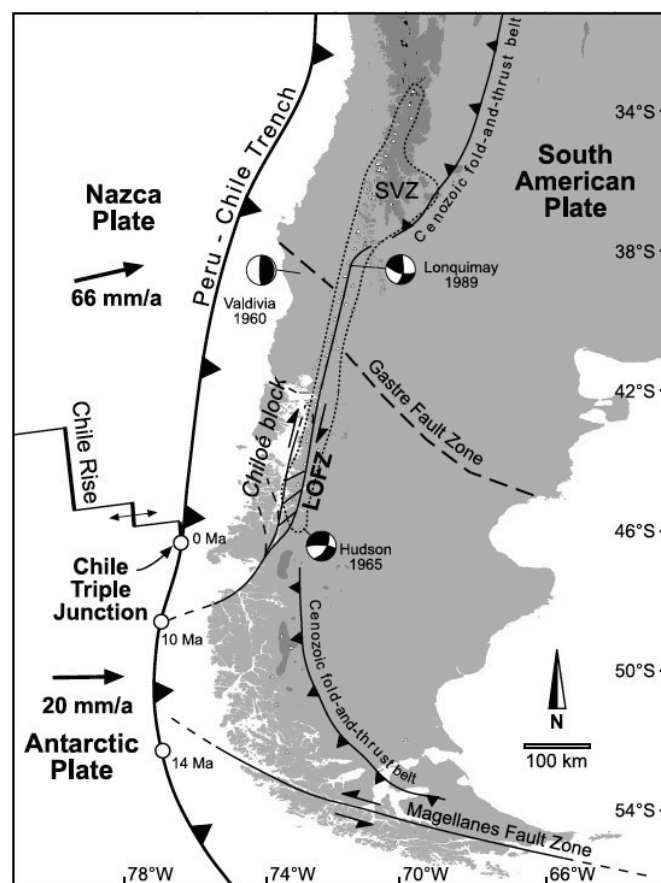
Figure 1.3 – Plate-tectonic setting in the Patagonian Andes with the indication of: LOFZ = Liquiñe-Ofqui Fault Zone, MFZ = Magellanes Fault Zone, CTJ = Chile Triple Junction (dots indicate the northward migration of the CTJ during the Neogene), SVZ = Southern Volcanic Zone of the Andes (Rosenau et al., 2006).
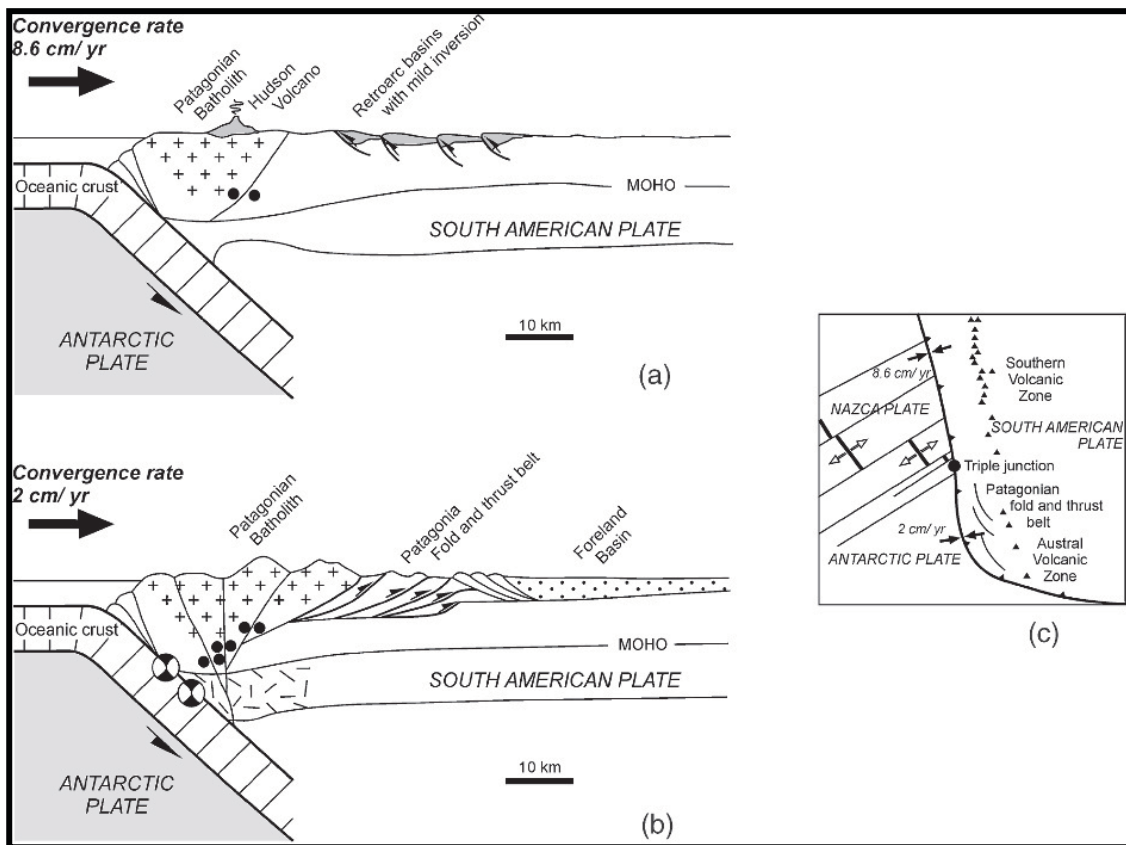
Figure 1.4 – Present tectonic setting of the Patagonian Cordillera (a) North and (B) South of the triple junction. Note the active different features such as the volcanic arc, the mild deformation of the retroarc region vs. the fold and thin-skinned thrust-belt driving shortening and uplift. In the inset is indicated the plate kinematics of the triple junction between Nazca, South America and Antarctic plates (Ramos and Ghiglione, 2008).
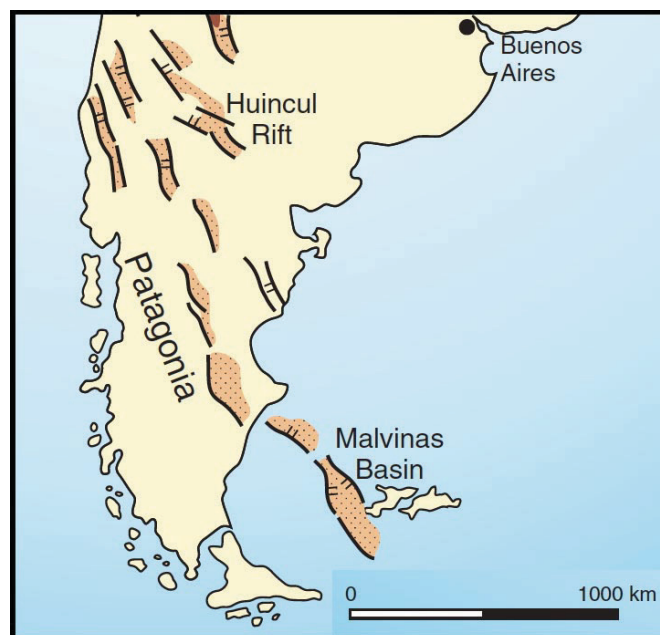
Figure 1.5 – Late Triassic–Early Jurassic generalized extension in the Andean basement (modified after Ramos et al., 2009).

13

The CTJ represents also the latitudinal limit at which a change in structural style is recognized for this sector, from thick- to thin-skinned thrust-belts (Figure 1.4; Kley et al., 1999; Ramos and Ghiglione, 2008), influencing the propagation of deformation to the east. In fact, foreland deformation is strongly influenced by the preexisting heterogeneities of the crust that act as preferential zones of weakness and can localize contractional deformation (e.g. Holdsworth et al., 2001; Ziegler et al., 1987; 1998; Cloetingh et al., 2008). In this context, positive inversion tectonics served of inherited rift-related normal faults to accommodate compressional deformation (Figure 1.5; Coward, 1994; Lacombe and Mouthereau, 2002; Butler and Mazzoli, 2006; Ramos et al., 2009). Thus, the study of these basin located in the so-called "broken foreland" represents a great opportunity to investigate the processes of far-field propagation related to orogen construction as they can preserve a record of the various stage of the Andean building. In this study we focussed our attention in the Gastre basin (Figure 1.6; Bilmes, 2014; Coira et al., 1975; Dalla Salda and Franzese, 1987) as a key-area to evaluate the magnitude of the Andean stages since the Cretaceous in the different sectors of the retroarc area and possibly to relate crustal processes to mantle geodynamics.
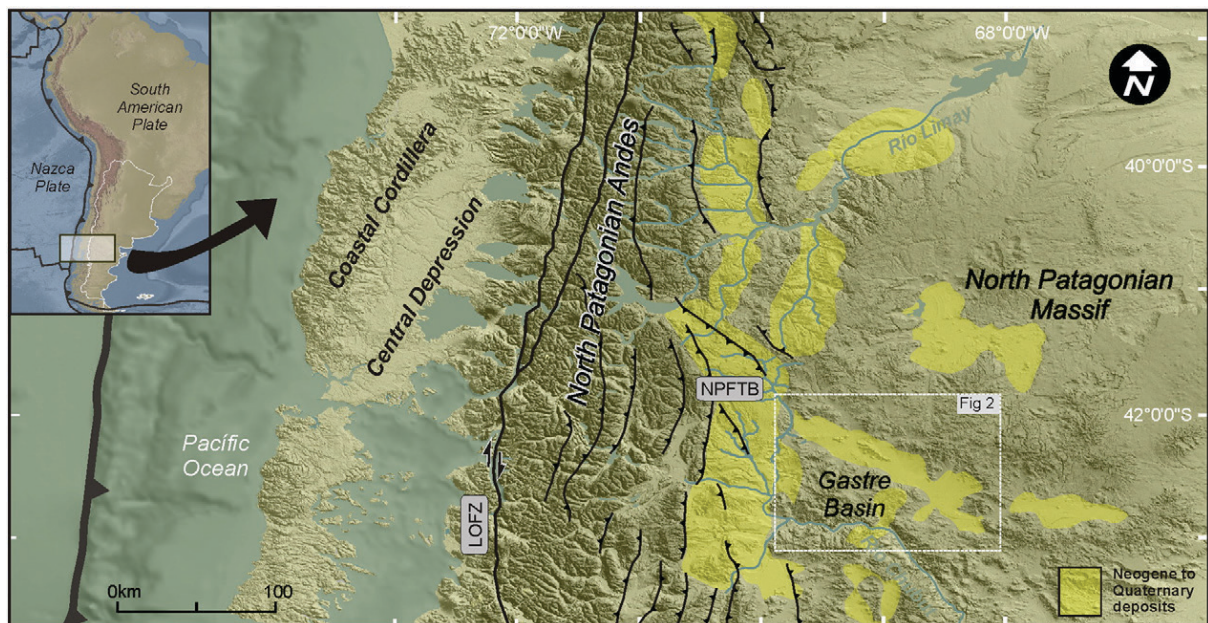
Figure 1.6 – Simplified map of the North Patagonian Andes and the adjacent foreland where the Gastre Basin is located, showing main structures and distribution of Neogene to Quaternary deposits (yellow areas). LOFZ: Liquiñi-Ofqui Fault Zone; NPFTB: North Patagonian fold and thrust belt (Bilmes et al., 2014).

1.3 Goals of the study

This study was aimed to reconstruct the Meso-Cenozoic evolution of the North Patagonian Andes in the last 100 Ma by constraining them with the help of low-T thermochronology and structural geology. In particular the goals of this study can be summarized in the following points:

- Give time and spatial constraints to the main tectonic events occurred in the Argentinian North Patagonia at latitudes between 40° and 44°S, with a particular focus on the debated Miocene evolution in the foreland zones;

- Compare times, rates and modes of the exhumation in the orogenic belt and adjacent foreland;

- Understand the link between deep geodynamic processes, deformation propagation in foreland regions, and erosion patterns recorded by low-T thermochronometers;

- Integrate structural model with LT-thermochronological data in order to provide a thermo-kinematic model of the study area.

1.4 Thesis outline

Low-Temperature thermochronology and structural methods were applied in this work to address the questions listed above. Sampling, analysis and data discussion were first performed in restricted key areas, and finally discussed at a regional scale.

Chapter 2 contains a synthesis of the materials and methodologies used in this thesis. Chapter 3 presents the results of the first part of the work, based on Apatite (U-Th)/He dating and structural survey at latitudes between 41.5° and 43° S and a first interpretation for this area. Chapter 4 is focuses on the thermo-kinematic model developed starting from AFT data along two cross-sections located at different latitudes. In Chapter 5, a second part of the AHe dataset is presented. These data, integrated with those presented in chapter 3, allow covering an area between 40° and 44° S, giving the possibility to extend at a regional scale the previously suggested geodynamic interpretation.

Chapter 6 summarizes the main conclusions of this thesis.

Chapter 2

Materials and Methods

In this work, low-temperature (low-T) thermochronology and structural methods have been applied in the North Patagonian Andes to understand the times and modes of the exhumation between 40° and 44° S, considering not only the well-studied axial part of the chain, but unravelling the complex evolution of this region even in the external part of the fold and thrust belt system. Moreover, an integration of these two basic methods has been carried out in order to produce the thermo-kinematic model along two transects, allowing the simulation of the evolution of the thermal field through time, predict thermochronometric ages along all the considered sections and, in turn, validate the proposed structural model. The next paragraphs give a short overview on both low-T thermochronometry—in this case for what concerning (U-Th)/He and fission track dating on apatite—, principles of cross-section balancing and restoration, and their integration in the production of a thermo-kinematic model.

2.1 Materials

During this thesis, a total of 48 samples has been collected and processed to perform thermochronometric analyses. Rocks have been sampled between 40° and 44°S covering the whole external parts of the orogen from the fold and thrust belt to the foreland in a range of longitudes going from c. 71.5°W to 68.5°W. Sampled rocks belong to basement outcrops (generally Paleozoic in age), Mesozoic intrusive rocks and sedimentary cover representing the infill of syn-rift basin formed during the upper Jurassic. Three to five kilos of rock from each sample have been processed at the Geosciences Department of Padua to extract apatite crystals. Samples rock information and type of analyses carried out on each sample are listed in Table 2.1 and their locations are shown in Figure 2.1. For both methods, sample preparation consists in an initial phase of apatites concentration starting from whole rock. Thus, rocks are crushed using a jaw crusher. A water table may be used to provide the first level of density-based separation, followed by sieving, drying, and magnetic and heavy-liquid density separations (Donelick et al., 2005).

Sample	Latitude	Longitude	Formation	Lithology	Age	AHe	AFT
G01	42°11'34,0"	69°09'56,3"	Lipetren	granite	(Permo)-Triassic	✓	✓
G02	42°15'57,4"	69°24'31,3"	Mamil Choique	granite	Lower Paleozoic to upper Paleozoic (Permian)	✓	✓
G03	42°20'17,2"	69°22'32,0"	Lipetren	granite	(Permo)-Triassic		
G04	42°23'16"	69°31'19"	Mamil Choique	granite	Lower Paleozoic to upper Paleozoic (Permian)	✓	✓
G05	42°22'10"	69°37'45"	Cañadón Asfalto	conglomerate	Upper Jurassic	✓	✓
G06	42°26'40,2"	68°46?49,2"	Cañadón Asfalto	arkose	Upper Jurassic	✓	✓
G07	42°33'35,6"	69°00'14,4"	Mamil Choique	granite	Lower Paleozoic to upper Paleozoic (lower Permian)	✓	✓
G08	42°33'50,5"	69°00'15,4"	Mamil Choique	granite	Lower Paleozoic to upper Paleozoic (lower Permian)	✓	✓
G09	42°24'47,7"	69°46'56,4"	Cañadón Asfalto	arkose	Upper Jurassic	✓	✓
G10	42°05'43,6"	69°46'30,1"	Mamil Choique	granite	Lower Paleozoic to upper Paleozoic (lower Permian)	✓	
G11	42°18'41,3"	70°02'12,9"	Mamil Choique	granitic dyke	Lower Paleozoic to upper Paleozoic (lower Permian)	✓	
G12	42°02'07,3"	70°17'57,7"	Mamil Choique	granite	Lower Paleozoic to upper Paleozoic (lower Permian)	✓	✓
G13	42°22'25,6"	69°36'14,2"	Cañadón Asfalto	sandstone	Upper Jurassic	✓	✓
G14	42°25'31"	68°50'05"	Cañadón Asfalto	sandstone	Upper Jurassic	✓	
G15	42°35'10"	68°48'46"	Mamil Choique	granite	Lower Paleozoic to upper Paleozoic (lower Permian)	✓	✓
G16	42°35'18"	69°44'05"	Paso del sapo	sandstone	Upper Jurassic		
G17	41°42'43,8"	69°37'09,5"	Mamil Choique	granite	Lower Paleozoic to upper Paleozoic (lower Permian)	✓	✓
G18	42°55'50,2"	71°15'38,0"	Subcordilleran Plutonic Belt	granite	Lower Jurassic	✓	
G19	42°48'23"	71°39'39,4"	Patagonian Batholith	granitoid	Upper Cretaceous	✓	
G20	42°23'05,4'	71°14'43,3"	Leleque	granite	Upper Jurassic	✓	
G21	42°10'02,9	71°21'26,7"	Subcordilleran Plutonic Belt	granodiorite	Lower Jurassic	✓	✓
G22	42°01'49,6"	71°34'34,0"	Patagonian Batholith	granite	Upper Cretaceous	✓	✓
G29	43°59'53"	68°49'18"	La Rueda	granite	Upper Jurassic		
G30	43°44'38"	69°49'07"	Osta Arena	sandstone	Lower Jurassic	✓	
G31	43°39'54"	70°05'02"	Tepuel Group	sandstone	Carboniferous to Permian	✓	
G32	43°34'22"	70°21'34"	Tepuel Group	sandstone	Carboniferous to Permian		
G33	43°31'49"	70°42'26"	Tepuel Group	sandstone	Carboniferous to Permian		
G34	43°46'14"	70°55'48"	Rio Hielo	granitoid	Cretaceous		
G35	43°19'28"	70°53'46"	Rio Hielo	granitoid	Cretaceous	✓	
G36	43°34'24"	71°08'12"	Rio Hielo	granitoid	Cretaceous		
G37	43°31'30"	71°31'05"	Rio Hielo	granodiorite	Cretaceous	✓	
G38	41°51'03"	71°25'19"	Complejo Colohuincul	granodiorite	Lower Paleozoic to upper Paleozoic (lower Permian)	✓	
G39	41°33'23"	71°28'50"	Batolito Patagonico Cordillerano	granite	Cretaceous	✓	
G40	41°20'41"	71°30'23"	Complejo Colohuincul	granodiorite	Lower Paleozoic to upper Paleozoic (lower Permian)	✓	
G41	41°06'22"	71°28'59"	Batolito Patagonico Cordillerano	granite	Cretaceous	✓	
G42	41°04'33"	70°40'14"	Plutonitas Pilcaniyeu	granite	Lower Jurassic		
G43	41°02'22"	70°15'21"	Comallo Granodiorite	granodiorite	Carboniferous		
G44	41°12'32"	70°10'00"	Mamil Choique	granodiorite	Ordovician	✓	
G45	40°55'05"	70°13'29"	Mamil Choique	granodiorite	Ordovician		
G46	40°54'06"	70°02'46"	Mamil Choique	granodiorite	Ordovician	✓	

| G47	40°48'09"	69°53'00"	Mamil Choique	granodiorite	Ordovician	✓
G48	40°53'37"	71°29'42"	Los Machis	granodiorite/tonalite	Upper Jurassic to Cretaceous	✓
G49	40°29'07"	71°35'22"	Los Machis	granodiorite/tonalite	Upper Jurassic to Cretaceous	✓
G50	40°11'44"	71°21'41"	Complejo Colohuincul	granodiorite	Devonian to Carboniferous	✓
G51	40°07'44"	71°38'40"	Los Machis	tonalite	Upper Jurassic to Cretaceous	✓
G52	39°59'06"	71°17'02"	Complejo Colohuincul	granodiorite	Devonian to Carboniferous	
G53	40°22'06"	70°39'43"	Cushamen	granite	Devonian to Carboniferous	✓
G54	40°16'56"	70°22'49"	Mamil Choique	granodiorite	Carboniferous to Permian	✓

Table 2.1 – sample information.
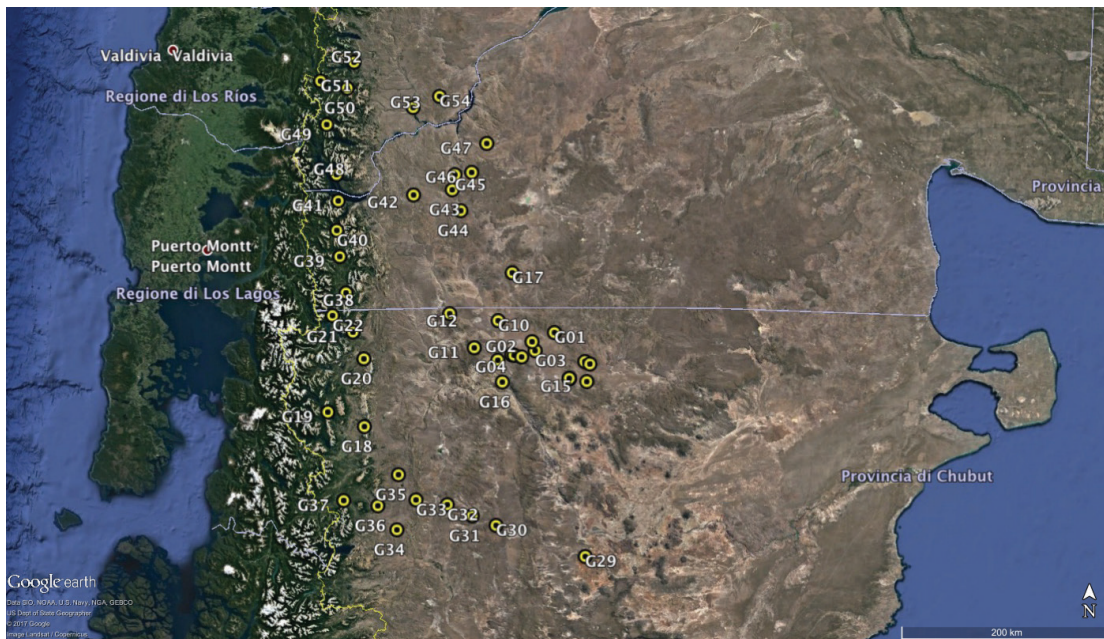
Figure 2.1 – Landsat image showing samples location.

2.2 Low-T thermochronologic techniques

Low-T thermochronology measures the timing and rates at which rocks approach the surface and cool as a result of exhumation, that can be caused by tectonic and/or surficial processes (Ring et al., 1999; Reiners and Brandon, 2006). In this work, apatite (U-Th)/He (AHe) and apatite fission track (AFT) have been used to define the uplift and erosion patterns in the North Patagonian region from the Main Cordillera.

The two used methods are based on the radioactive decay of a parent nuclide and the accumulation of a corresponding daughter product (nuclide or effect of the fission in the crystal lattice) to date the cooling age of a mineral. In both the cases the cooling age is defined, in its simplest form, in relation with the specific closure temperature (T_c) (Dodson, 1973) of the system above which time *zero* is recorded by the "clock" – represented by the thermochronometer – that starts to register the time-temperature history of the sample. Other thermochronometers currently in use, and the approximate closure temperature ranges of application, are shown in Figure 2.2.
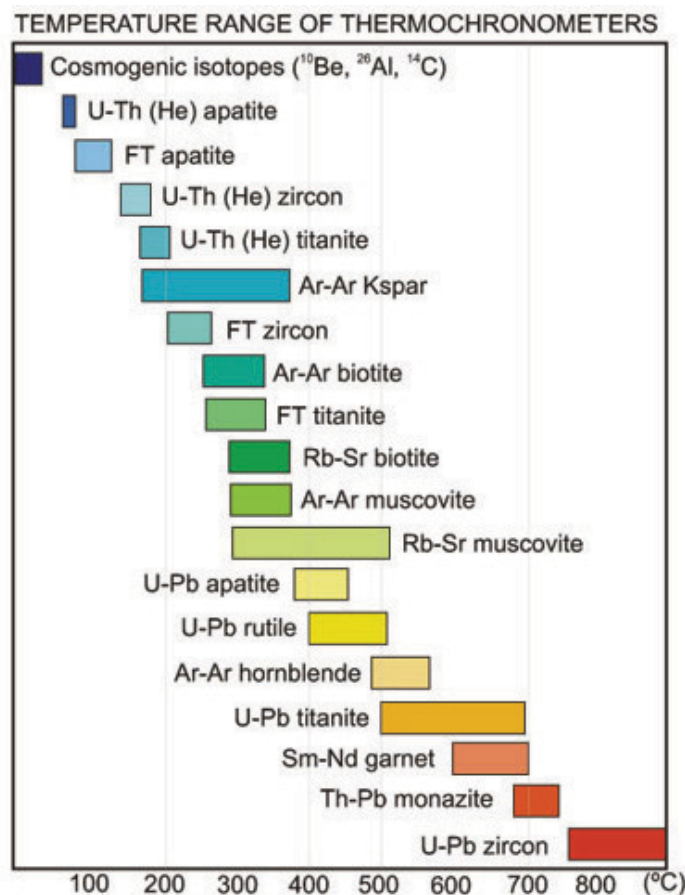

Figure 2.2 – Nominal closure temperatures of various geochronometers and thermochronometers in current use (Cloetingh, et al., 2007).

However, the closure of a thermochronometer occurs through a range of decreasing temperatures for which the retention of the decay products progressively increases. This temperature window is called Partial Retention Zone (PRZ) for AHe system and Partial Annealing Zone (PAZ) for FT system (Wagner, 1979). In the following two paragraphs the two systems are discussed more in detail.

2.2.1 Apatite (U-Th)/He thermochronometry

AHe system is one of the most sensitive thermochronometers. It is based on the decay of ^{238}U, ^{235}U, and ^{232}Th in the stable ^{206}Pb, ^{207}Pb, and ^{208}Pb, and the emission of ^{4}He nuclei (alpha particles) at each step as daughter nuclides.

The decay equation for (U-Th)/He dating is:

$$^{4}\text{He} = 8^{238}\text{U}\left[e^{\lambda_{238}t} - 1\right] + 7^{235}\text{U}\left[e^{\lambda_{235}t} - 1\right] + ^{232}\text{Th}\left[e^{\lambda_{232}t} - 1\right] + ^{147}\text{Sm}\left[e^{\lambda_{147}t} - 1\right]$$

where ^{4}He, ^{238}U, ^{235}U and ^{232}Th and ^{147}Sm are the present-day atoms, λ are their relevant decay constants and t is the accumulation time or Helium age (Farley, 2002; Reiners, 2002). The coefficients preceding the Uranium and Thorium abundances account for the α multiple particles emitted within each decay series (Farley, 2002). This equation assumes that no initial ^{4}He is present in the crystal and secular equilibrium among all daughters in the decay chain is maintained.

The He ingrowth with time can be also written as a function of U, Th and Sm concentration taking into account the ^{238}U/^{235}U ratio is constant.

When AHe cooling ages are calculated, several factors must be considered: (i) the α-ejection, that takes into account the distance travelled by the α particles during the decay process and cause the ejection of He particles out of the apatite crystal causing younger calculated AHe ages (Farley et al., 1996); (ii) the presence of zonation, (iii) the distribution of U and Th within the crystal (Meesters and Dunai, 2002); (iv) the possible presence of U-rich inclusions, that can affect the total helium budget and let register older age. Another basic issue regarding this system is that the passage from an open to a closed system is gradual, in a temperature interval ranging between 40°C and 80°C (so-called PRZ; Wolf et al., 1998; Farley, 2000) and is characteristic of the diffusional behaviour of Helium into the crystal. Diffusivity has been found to depend exponentially by the temperature through the so-called "Arrhenius relationship":

$$\frac{D}{a^2} = \frac{D_0}{a^2} e^{(-\frac{E_a}{RT})}$$

where D_0 is the frequency factor, that is diffusion at infinite temperature, E_a is the activation energy, T is the temperature, R is the gas law constant and a is the radius of the spherical diffusion domain that can be considered the grain volume (Farley, 2000). In light of this, T_c is a function of the activation energy, frequency factor, cooling rate, and geometry and size of the crystal/grain (Reiners and Brandon, 2006). In the last years, several new diffusional models for He have been proposed, always based on the same equation, but accounting other complication as the radiation damages effect on He diffusivity (i.e. Shuster et al., 2006; Shuster and Farley, 2009; Flowers et al., 2009; Gautheron et al., 2009, 2012; Gautheron and Tassan-Got, 2010).

To perform AHe dating, generally three grains from each sample are selected, digitally photographed and measured along length and width (parallel and perpendicular to the c-axis) on two faces. After measurement they are packed in Nb tubes. A two-stage analytical procedure is commonly used to measure ^{4}He, U, Th and Sm. In the first stage the crystal is degassed by twice heating using a diode laser at 1030±50°C for 5 minutes, allowing total He degassing and to check the presence of He trapped in small inclusions (see Fillon et al. [2013] for more details) and ^{4}He is measured by gas-source mass spectrometry. In the second stage, apatite grains are dissolved for 3 hours at 70°C in a 50 µL HNO$_3$ 5N$^-$ solution containing a known content of ^{235}U, ^{230}Th, and ^{149}Sm, and additional 50 µL HNO$_3$ 5N$^-$ and then filled with 0.9 mL of ultrapure MQ water. The final solution is then measured for U, Th, and Sm concentrations by quadrupole inductively coupled plasma (ICP-quadrupole) mass spectrometry. External age standards, in our case Limberg Tuff and Durango apatites, are used to calibrate the age. During this project, the two-part analytical procedure has been carried out at the IDES low-temperature thermochronology Laboratory (University of Paris Sud XI, Orsay, France) and LSCE (Laboratoire des Sciences du Climat et de l'Environnement, University of Versailles , Gif/Yvette, France), respectively.

As said above, one of the corrections that need to be done concerns the α-ejection; to do this, sphere equivalent radius, weight, and ejection factors have been determined, assuming a homogeneous distribution of U and Th in apatite, using dedicated software (Gautheron and Tassan-Got, 2010; Ketcham et al., 2011; Gautheron et al., 2012). Corrected age data are first checked for reproducibility between replicate. In case of well

reproducible samples the weighted mean of ages can be used for interpretation (as suggested by Fitzgerald et al. [2006]) and the T_c concept can generally be applied, whereas in case of high dispersion, range of ages are preferably shown. Dispersion in ages can result by several factors. For example, replicates with different grain size of a slowly cooled sample, usually show a correlation between grain age and radius; in this case, further information for the reconstruction of the thermal history of the sample can be extracted. If the age dispersion is due to radiation damages a correlation between grain age and eU should be observed. Age dispersion is typical of partially reset samples and thermal modelling to evaluate the degree of partial resetting and identify possible temperature-time paths is crucial.

2.2.2 Apatite fission track thermochronometry

Similarly to (U-Th)/He thermochronology, apatite fission track analysis (AFT) is a dating technique recording the time at which a rock passed through a closure temperature of roughly 110°C (Wagner, 1968). It is based on the spontaneous fission of naturally occurring [238]U and the damage produced by the two daughter nuclides of roughly similar size, which repeal each other, moving in opposite directions through the crystal lattice. The fission track is, indeed, the damage zone formed during the passage through the crystal lattice ("Ion explosion spike theory", Fleischer et al., 1965; 1975; Figure 2.3). The equation that describe fission tracks accumulation as a function of time (t) is described by the decay equation (Tagami and O'Sullivan, 2005):

$$N_S = \frac{\lambda_f}{\lambda_\alpha} {}^{238}N(e^{\lambda_\alpha t} - 1)$$

where N_s is the number of spontaneous fission tracks per unit volume; [238]N is the number of [238]U atoms per unit volume; λ_f and λ_α are the decay constants for spontaneous fission and α decay of [238]U (λ_f = 8.5 10-17 yr^{-1} and λ_α=1.5 10-10 yr^{-1}). When they form, new fission tracks measure c. 16 μm in apatites.
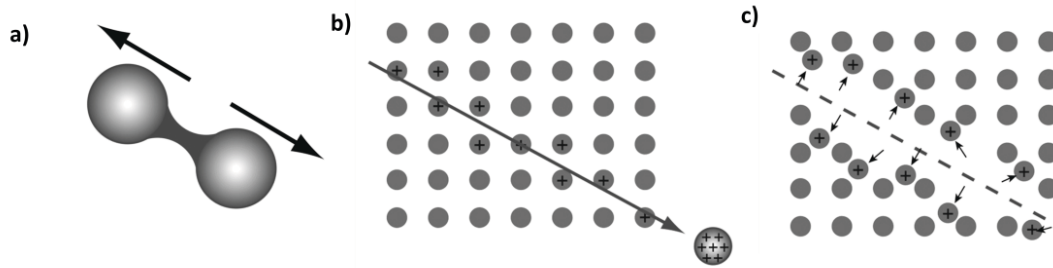
Figure 2.3. –The "Ion Explosion Spike" model for FT formation (from Fleischer et al., 1975). The heavy nucleus splits in two nuclear fragments (a); the two positively charged fragments are pushed away from each other and along their track they tear off electrons from the atoms of the lattice (b); the positively charged atoms along the track dislocate from their lattice position due to repulsive electrostatic forces (c).

The density of fission tracks within a crystal will increase with time and concentration of ^{238}U. However, as for AHe system, it exists a partial annealing zone (PAZ: ~60°C to 120°C; Wagner, 1968; Green et al., 1989) and if the crystal is at a temperature above or within the PAZ for a sufficiently long period of time, the crystal lattice will recover and the tracks will anneal. Differently to other thermochronometric methods which measures the parent and daughter nuclides concentration, in FT dating parent and daughter products are measured indirectly by counting fission tracks (Carrapa and Pyton, 2013). One of the most adopted methods to infer single crystal age is the External Detector Method (EDM; Gleadow, 1981; Hurford and Green, 1982; 1983; Green, 1985; Gleadow et al., 1986; Hurford, 1990; Figure 2.4) in which the following equation give the single grain age:

$$t_i = \frac{1}{\lambda_d} \ln\left(1 + \lambda_d \zeta g \rho_d \frac{\rho_{s,i}}{\rho_{i,i}}\right)$$

Where subscript i refers to grain i; t_i is fission track age of grain i; λ_d is the total decay constant of ^{238}U; ζ is the calibration factor based on EDM of fission track age standards, depending on the microscope, the reactor and the operator; g is the geometry factor for spontaneous fission track registration, ρ_d the induced fission track density for a uranium standard corresponding to the sample position during neutron irradiation, $\rho_{s,I}$ is the spontaneous fission track density for grain i; $\rho_{i,i}$ is the induced fission track density for the grain i (Donelick et al., 2005).

Sample is constitutes by a mount of apatite grains that is polished and chemically etched, revealing the fission tracks on the polished surface of the crystals. U-free muscovite sheets

(the external detectors) are coupled to the grain mounts on the polished surface and are irradiated with low-energy thermal neutrons in a nuclear reactor which induces fission of ^{235}U and producing fission tracks in both the apatite and the mica sheet at contact. The number of induced fission can be then measured on the mica surface after proper chemical etching. As ratio of ^{238}U /^{235}U is constant, ^{238}U content is calculated measuring the amount of ^{235}U obtained by the induced tracks. For standardization a similar mica sheet is also placed in contact with a small chip of 235U doped glass.
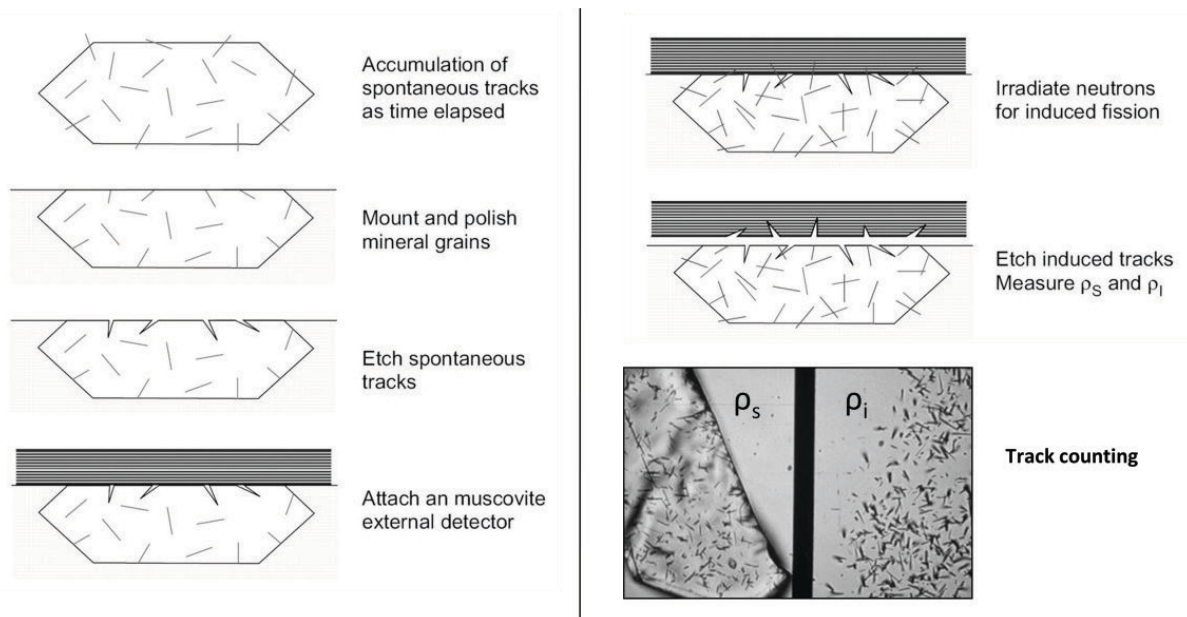
Figure 2.4 –Schematic procedure for FT analysis with the EDM method (from Tagami and O'Sullivan, 2005). Source for the picture of spontaneous and induced tracks is the www.geotrack.com.au website.

The mica monitor and the mount are assembled in the same slide and analysed with an optical microscope implemented with a sliding table and a dedicated software. The operator is then enabled to measure spontaneous and induced track density for the single mineral grains (Reiners and Brandon, 2006).

Similarly to He diffusion, fission track anneals as a function of temperature, following an Arrhenius-type formula. This process is also dependent on the crystallographic orientation, the composition and kinetic characteristics of the apatite crystal—which can be taken into account considering the D_{par} (the diameter of fission-track etch pits parallel to the apatite crystal c-axis) (Donelick, 1993; Carlson et al., 1999; Donelick et al., 1999; Ketcham et al., 1999). One way to quantify the annealing is to measure the lengths of horizontal confined tracks (Gleadow et al., 1986). Their distribution, in fact, contains information on the thermal history experienced by the sample (Braun et al., 2006).

In this work, track densities have been measured on 25 (in intrusive rocks) and 40 (in sedimentary rocks) grains from the same sample, whereas 100 lengths, or less when not possible, were measured per sample. The measured parameters to obtain AFT ages are: (i) the numbers of spontaneous and induced tracks and (ii) the area; while for quantify the annealing: (i) the track lengths, (ii) their orientation with respect to c-axis and (iii) the mean D_{par} for track lengths measurements. Data are processed with a dedicated software (e.g. Trackey; Dunkl, 2002), which calculates single grains ages and display data by radial plots. The χ-square statistical test is then used to determine if counted grains belong to the same population of ages, by comparing the variance of the observed population with the variance predicted for the decay process (Galbraith, 1981; Brandon, 1992). To describe a single population the central age is generally used (Galbraith, 1988).

2.2.3 Multiple dating and thermal modelling

The two techniques described above became particularly powerful when they are applied together on the same sample. This is given by the fact that they are characterized by different thermal sensitivity windows and can significantly enhance the ability to derive comprehensive and self-consistent thermal histories (Stockli, 2005). To integrate the AHe, and AFT data, testing plausible thermal histories, inverse thermal modelling was performed in this work on several samples, using the software HeFTy (Ketcham, 2005). HeFTy is a Monte Carlo simulation based software that allows to find the best-fit thermal history and provides a good statistical match to measured thermochronometer ages (Paython and Carrapa, 2013). Modelling of ages, moreover, allow to "correct" the problems that arise in age distribution of AHe data because it takes into account the effects of grain size, radiation damage, and cooling rate on the thermal history and/or translate the track length distribution for AFT in thermal path (Ketcham , 1999, 2005; Flowers et al. , 2009). Modelled thermal path constituted the starting point in the cross section restoration because it gives a first idea about the range of temperature experienced by lithostratigraphic units and, thus, a preliminary range of depth to deform back in time the geological setting of the studied area, than refined by means of thermo-kinematic model.

2.3 2D kinematic model

The basic idea in cross-section balancing and restoration is that deformation is assumed to neither create nor destroy rock volume; thus, return to the undeformed state from the deformed one should be possible applying geometrical rules and validating the initial interpretation. This method was firstly used to calculating depth of the detachment and shortening (Chamberlain, 1910, 1919; Bucher, 1933) and then extended to the single layers of a sections (Dahlstrom, 1969; Mitra and Namson, 1989) allowing to deform a geological cross-section back in time to provide the undeformed (or a less deformed) state. During this operation effects of fault displacements, folding associated with faulting and flexural slip are removed, such as volume loss generated from compaction and erosion and vertical movement produced by isostasy are taken in account.

Starting from the first works in crustal shortening regime settings, this method has been applied progressively both in extensional and inverted basin areas (Bulness and McClay, 1999 and references therein). In the oil industry, this technique is routinely used to evaluate the position of source rocks and model hydrocarbon generation, expulsion and migration, as well as to analyze structural traps in terms of timing and geometry (Buchanan, 1996). The original concept of cross-section balancing was postulated by Chamberlin (1910) and was the area preservation between the deformed bed of a restored cross-section, then generalized by Dahlstrom (1969) as a constant volume criterion (Groshong, 2006). Ideally, boundary of the section should be such that after the restoration the undeformed state result in a rectangle (in 2D) which two edges are called pin lines and represents the lines where no interbed slip occurs (Groshong, 2006). Another important rule is to choose a section plane normal to the main tectonic transport direction in order to avoid "out of plane" movement. In this Ph.D. project (Chapter 4), the restoration is performed using Move, software developed by Midland Valley Exploration Ltd. This software allows 2D cross-section construction and kinematic restoration offering several algorithms. The most important ones are: flexural slip, simple shear and fault parallel flow.
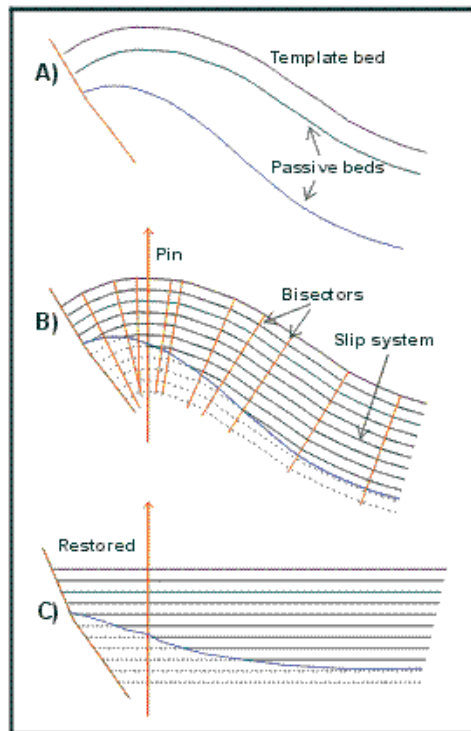
Figure 2.5 – Schematic representation of the flexural slip deformation mechanism

The flexural slip restoration (Figure 2.5) is based on the assumption that bed lengths do not change during deformation (Chamberlin, 1910; Dahlstrom, 1969; Woodward et al., 1986) and deformation occurs only by slip along bedding planes. It is a constant bed length and constant bed thickness model and founds its application in compressive setting when structurally induced folding does not induce appreciable thickness variations (Groshong, 2006).
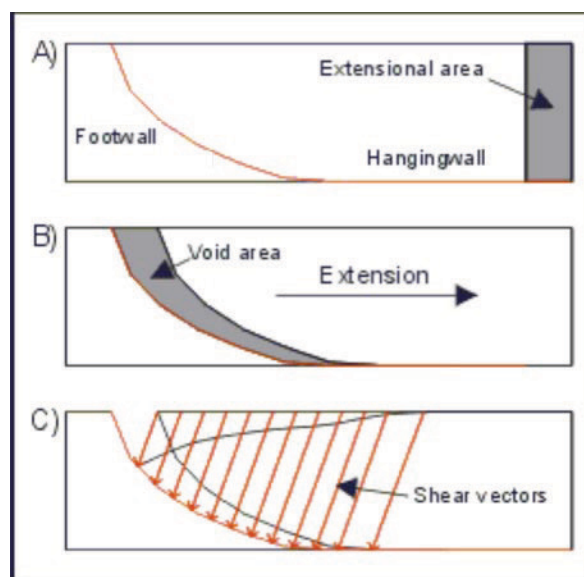
Figure 2.6 – Schematic representation of the simple shear mechanism deforming the hangingwall of a listric normal fault.

Simple shear (Figure 2.6) is an algorithm that relates the geometry of the deformational features found in the hanging wall to the fault's shape (Gibbs, 1983; Withjack and Peterson, 1993). The shear direction is characterized by an α angle with respect to the regional (if α=90° it is called vertical simple shear; for α<90° it is called oblique simple shear). Simple shear restoration is used for restoration/forward modeling of extensional structures, inverted basins and, growth faults. In Move the area of modeled hanging wall is conserved but variation of thickness and bed length can be introduced.
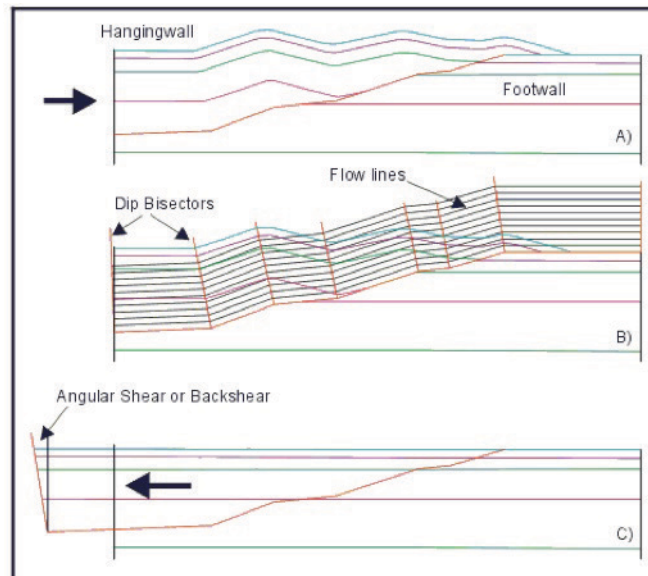
Figure 2.7 – Schematic representation of the fault parallel flow mechanism deforming the hanging-wall of an inverse fault.

The fault parallel flow algorithm (Figure 2.7; Sanderson, 1982; Keetley and Hill, 2000) is based on the principle that material of the hanging wall flows over a fault surface while the footwall remains undeformed and is not translated. The fault plane is divided into discrete dip domains where a change in the fault's dip is marked by a dip bisector. Flow lines are constructed by connecting points on different dip bisectors of equal distance from the fault plane through material particles move. Fault parallel flow algorithm is best suited to be applied in fold and thrust belt settings. In this case bed area is conserved.

Once the restoration leads to the undeformed (or less deformed state) it is possible to validate the structural model also applying the inverse approach, called forward kinematic model (Suppe, 1983; Endignaux and Mugnier, 1990) that geometrically re-deform the cross-section starting from the initial state.

2.4 Thermo-kinematic modeling

One part of the thesis has been focused on the production of a 2D-thermo-kinematic modeling along two transect of the studied area combining information collected from low-T dating and structural analysis. This implies the possibility to use time-temperature histories coming from the data to infer rate of the processes occurred taking into account factors that can profoundly affect the thermal field during deformation, and allowing a correct conversion from the temperature to depth domain. In fact, factors such as heat advection, topography and tectonics can deeply modify the thermal field during deformation. Several works have demonstrated that shallower isotherms are perturbed by the relief, depending on its wavelength (Stuwe et al., 1994; Mancktelow & Grasemann, 1997; Braun, 2002; Reiners and Brandon, 2006) as well as tectonics that is able to deflect the isotherms in correspondence of faults causing lateral heat flow (Ehlers and Farley, 2003). All these factors are considered when a sequential restoration is processed with FetKin - Finite Element Temperature and Kinematics (Almendral et al., 2015). This is a software package designed to model the thermal evolution of a sequence of balanced cross-sections made with programs such as 2D Move (Midland Valley Ltd.) by solving numerically the transient advection–diffusion equation in two dimensions (Carslaw and Jaeger, 1986):

$$\rho c \left(\frac{\delta T}{\delta t} - vx \frac{\delta T}{\delta x} - vy \frac{\delta T}{\delta y} \right) = \frac{\delta}{\delta x} k \frac{\delta T}{\delta x} - \frac{\delta}{\delta y} k \frac{\delta T}{\delta y} + \rho H$$

where: T(x,y,t) represent the temperature in the location (x,y) and at the time t; ρ(x,y) is the (space-dependent) density of the rock; K(x,y) defines the rock thermal conductivity tensor; c(x,y) is the specific heat and v(x,y) is the velocity of the moving grid; H is the radioactive heat production.

The necessary information to model the thermal field (the thermal/rheological parameters) are imported in FetKin by means of an XML file, whereas the velocity field comes from the sequential restoration by exporting the section as ASCII files from Move. By modeling the isotherms through the time is, thus, possible to predict the cooling ages along the present-day topographic profile, for different low-T thermochronometers, using the algorithms developed for HeFTy by Ketcham (2005). This, in turn, allows validating the processed geological scenario comparing the predicted ages and the measured ages from samples lying along the section.

Chapter 3

This chapter is focused on the application of both Apatite (U-Th)/He thermochronology and structural analysis between 41°30′ to 43°S. It represents the first part of the work carried out during the Ph.D. and resulting after the first fieldwork carried out through the Rio Negro and the North Chubut Provinces. In this work the aim was to understand the different pattern of exhumation recorded both in the fold and thrust belt and in the foreland. For understand the foreland behavior during the compressive stages the Gastre Basin was chosen as a key area. Moreover, a model for the propagation of the compressive stress away to the trench related to mantle geodynamics is proposed. In the following chapter the version of the manuscript published on Tectonics is presented.

(Un)Coupled thrust belt-foreland deformation in the northern Patagonian Andes: New insights from the Esquel-Gastre sector (41°30′–43°S)

E. Savignano[1], S. Mazzoli[2], M. Arce[3], M. Franchini[3, 4], C. Gautheron[5], M. Paolini[6], and M. Zattin[1]

[1]Department of Geosciences, University of Padua, Padova, Italy, [2]Department of Earth Sciences, University of Naples Federico II, Napoli, Italy, [3]Instituto de Investigación en Paleobiología y Geología, Universidad Nacional de Río Negro, Rio Negro, Argentina, [4]Centro Patagónico de Estudios Metalogenéticos, Universidad Nacional del Comahue, Neuquén, Argentina, [5]GEOPS, Univ Paris Sud, CNRS, Université Paris-Saclay, Orsay, France, [6]Ciudad Autónoma de Buenos Aires, Pan American Silver, Santa Cruz, Argentina.

Key Points:

• New apatite (U-Th)/He ages were obtained for the Patagonian Andes at latitudes 41°30′-43°S

• The "broken foreland" area was characterized by Late Cretaceous to Paleogene exhumation

• Thrust belt-foreland (un)coupling of the deformation depends on steep- versus flat-slab subduction

Abstract

The Patagonian Andes represents a unique natural laboratory to study surface deformation in relation to deep slab dynamics. In the sector comprised between latitudes 41°30′ and 43°S, new apatite (U-Th)/He ages indicate a markedly different unroofing pattern between the "broken foreland" area (characterized by Late Cretaceous to Paleogene exhumation) and the adjacent Andean sector to the west, which is dominated by Miocene-Pliocene exhumation. These unroofing stages can be confidently ascribed to inversion tectonics involving reverse fault-related uplift and concomitant erosion. Late Cretaceous-Paleogene shortening and exhumation are well known to have affected also the thrust belt sector of the study area during a prolonged stage of flat-slab subduction. Therefore, the different ages of near-surface unroofing documented in this study suggest coupling of the deformation between the thrust belt and its foreland during periods of flat-slab subduction (e.g., during Late Cretaceous-Paleogene times) and dominant uncoupling during periods of steep-slab subduction and rollback, even when these are associated with high convergence rates (i.e., > 4 cm/yr), as those documented in Miocene times for the Patagonian Andes.

3.1 Introduction

The process of far-field stress propagation from the orogen to the foreland plate is well known to occur and has been invoked to explain distributed weak strain recorded in large foreland sectors ahead of the thrust front (e.g., Geiser and Engelder, 1983). However, modes of deformation in the foreland domain are dominantly of localized rather than distributed type. This is interpreted to be due to the fact that the continental lithosphere of the foreland plate is generally cooler and stronger with respect to that of the orogen, which is characterized by a warmer lithosphere and therefore a weaker rheology (Butler and Mazzoli, 2006). In the Andes, basement shortening associated with strong inversion and uplift of the axial zone of the Permo-Triassic rift in the Eastern Cordillera of Peru, although being accommodated by localized shear involving widespread reactivation (at lower greenschist facies conditions) of inherited mesoscopic fractures, has been documented to represent a process of distributed strain at the orogen scale (Mazzoli et al., 2009). This pro- cess has been invoked to explain internal straining of basement blocks in

order to accommodate thick-skinned Andean shortening (e.g., in the Malargüe fold and thrust belt of Argentina, at latitudes 34–36°S) (Mescua et al., 2012). Similarly, in the external Western Alps, the Variscan basement has been documented by Bellahsen et al. (2012) to have accommodated Alpine shortening by distributed slip along greenschist facies shear zones. According to these authors, although no significant reactivation of the inherited Jurassic normal faults took place there, the inherited synrift basins localized thick-skinned shortening due to the weakening associated with both the presence of less competent basin fills (that were disharmonically folded) and the P-T conditions experienced during crustal shortening. On the other hand, in the foreland lithosphere, localized deformation at the kilometer scale may be accommodated by inherited brittle structures that represent preferential zones of weakness (Holdsworth et al., 2001). In this instance, positive inversion tectonics involving major reverse fault reactivation of deep-rooted discrete structures, particularly rift-related normal faults, is favored (Ziegler, 1987; Coward, 1994; Ziegler et al., 1995; Lacombe and Mouthereau, 2002; Butler and Mazzoli, 2006) and has been widely documented for the so-called "broken foreland" of the northern Patagonian Andes (Humphreys, 2009; Ramos and Folguera, 2009; Folguera and Ramos, 2011; Orts et al., 2012, 2015; Gianni et al., 2015a). Classically, shortening is assumed to migrate ahead of the thrust front, progressively involving foreland domains that previously experienced flexure-related stretching (e.g., Tavani et al., 2015). However, the situation is much more complex for the northern Patagonian fold and thrust belt and its foreland analyzed in this study (Figure 3.1a). Being located in the overriding plate of the Andean subduction system, this whole retroarc sector is interpreted to have experienced alternating shortening and upper plate extension during stages of flat- and steep-slab subduction, respectively (Ramos and Folguera, 2009; Folguera and Ramos, 2011; Orts et al., 2012, 2015). More in general, several orogenic cycles of mountain building and subsequent extensional dismembering associated with periods of shallowing and steepening of the subducting plate have been recognized in recent years in the Andes (Kley et al., 1999; Haschke et al., 2002; Kay and Coira, 2009; Ramos et al., 2014). These processes have been especially well documented for the southern Central Andes of Argentina and Chile between 34° and 37°S, where a complete cycle from crustal thickening and mountain building to extensional collapse has been unraveled and related to changes in the subduction geometry (Ramos et al., 2014). On the other hand, the

tectonic evolution of the Patagonian Andes further south is much less well known. Although a recent paper by Echaurren et al. (2016) provided important constraints based on the analysis of syntectonic strata, the degree of coupling versus uncoupling of the deformation between the thrust belt and its foreland during alternating stages of shallow underthrusting (i.e., flat-slab subduction) and of foundering of the subducting plate (i.e., slab rollback) needs to be further investigated. As a matter of fact, shortening and extension in the retroarc sector may vary not only in time (i.e., with major "cycles" of mountain building and orogenic collapse, respectively) but also in space, due to the variable transmission of horizontal compressive stress away from the orogen. Low-temperature (low-T) thermochronological systems are ideally suited for reconstructing thermal histories of rocks in the uppermost part of the crust because they record time and rates of cooling related to exhumation of the first kilometers of the crust. Presently, a rather extensive apatite fission track and apatite (U-Th)/He (AHe) dating database is available for the axial part of the orogen (Thomson et al., 2010; Guillaume et al., 2013; Folguera et al., 2015). However, such type of data are completely lacking from the broken foreland area. Yet this has experienced major tectonic events during Andean orogenesis (Echaurren et al., 2016). In this study, we integrate field structural observations with new AHe data in the Esquel-Gastre area (located at latitudes 41°30′–43°S) in order to analyze and compare the exhumation patterns from the frontal part of the orogen and from the adjacent foreland sector and then use them to gain new insights into the timing and modes of coupling versus uncoupling of the deformation between the northern Patagonian fold and thrust belt and its foreland.

3.2 Geological setting

The southern Andes is a roughly linear orogenic belt produced by the convergence between the Nazca and Antarctic plates beneath the South American plate. The building of the present-day orogen has been interpreted as a result of a series of shortening pulses that took place since the Late Cretaceous (Folguera and Ramos, 2011). Despite the general along-strike continuity of the mountain belt, its internal tectonic segmentation is marked by the variable position of the magmatic arc and of the deformation front in the retroarc area to the east. Thus, this plate margin results in a more complex configuration with respect to the simplified notion of "Andean-type" subduction system proposed in the past

literature (e.g., Gutscher, 2002). Marked variations in convergence rates have been calculated from continuous-GPS measurements and NUVEL-1 models along the chain.
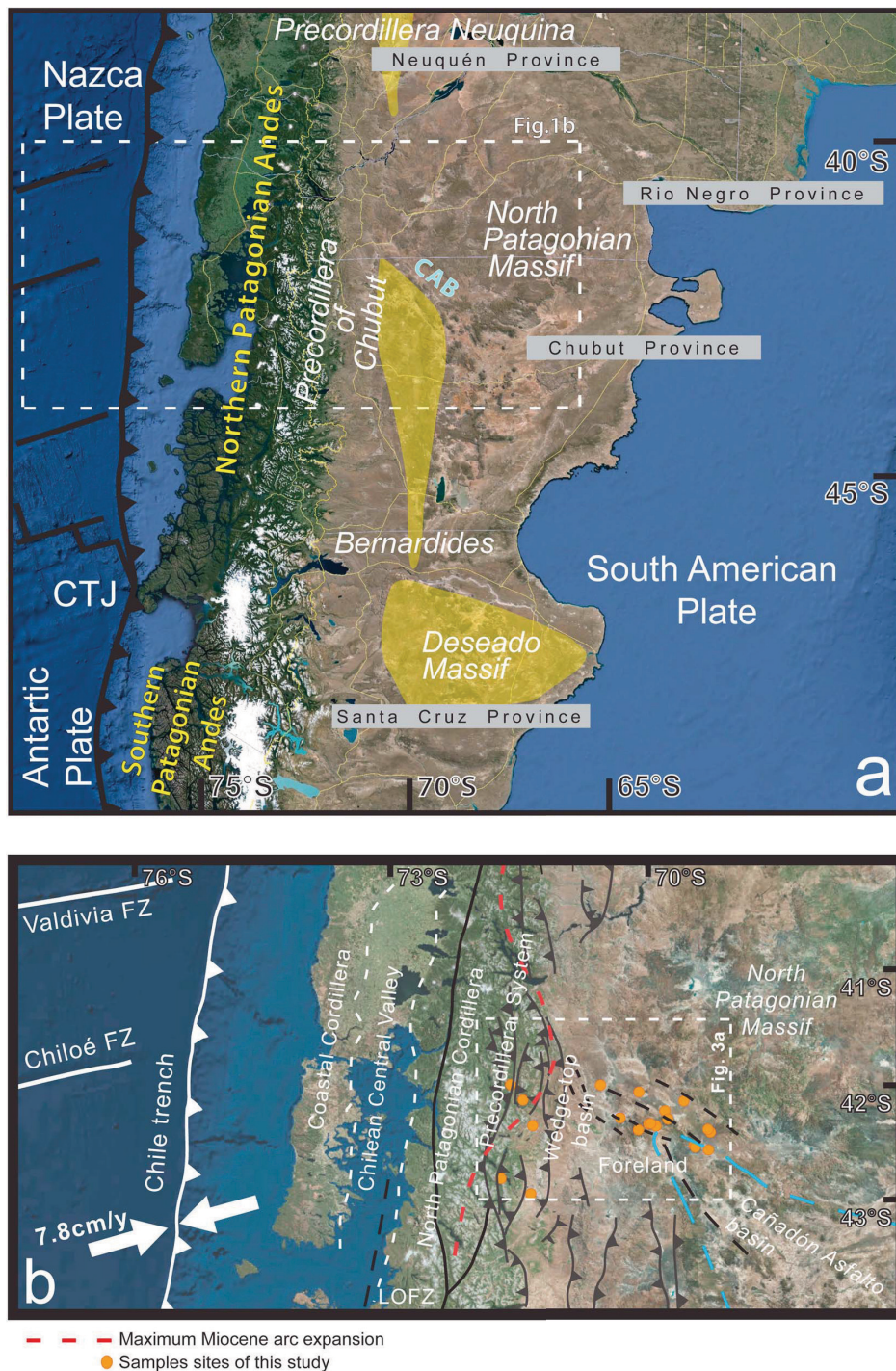
Figure 3.1 – (a) Present tectonic setting of North and Central Patagonia, showing administrative provinces, major tectonic features of the region, and location of Figure 3.1b. Yellow shaded areas represent deformed foreland sectors; CAB: Cañadón Asfalto Basin (boundary marked by blue line), CTJ: Chile Triple Junction. (b) Structural sketch map showing main morphotectonic units and structures of the Andes and adjacent foreland between 40° and 44°S, sampling sites of this study, and location of the geological map of Figure 3.3.; LOFZ: Liquiñe-Ofqui fault zone.

These measurements unraveled relatively high convergence rates (between 6 and 7 cm/yr) in the Nazca-South America sector and lower ones (less than 2 cm/yr) where the Antarctic plate sinks beneath South America (Gripp and Gordon, 1990; DeMets et al., 1990; Kendrick et al., 1999).

The area of this study is located between latitudes 41°30′ and 43°S, where the Andean orogen is constituted by a series of morphotectonic elements including, from west to east (e.g., Orts et al., 2015) (Figures 3.1b and 3.2), (i) the Coastal Cordillera, (ii) the Chilean Central Valley, (iii) the northern Patagonian Cordillera, and (iv) the foreland. The Carboniferous-Triassic units of the Coastal Cordillera, which were deformed during the Gondwanian orogenic cycle, are partly covered by Mesozoic-Cenozoic strata (Thomson and Hervé, 2002; Willner et al., 2004; Orts et al., 2015). The Chilean Central Valley, representing the forearc region, hosts a series of Eocene to Quaternary basins filled by volcaniclastic, marine, and continental deposits (González, 1989; Radic et al., 2009). This area was affected by intense subsidence interpreted as resulting from subduction erosion in early Miocene times (~17 Ma), leading to a Pacific-derived transgression with the deposition of deep marine sediments (Encinas et al., 2012). The northern Patagonian Cordillera includes large Quaternary stratovolcanoes representing the recent volcanic arc (Stern, 2004) and underlying Neogene-Mesozoic volcaniclastic successions. These, in turn, rest on top of the North Patagonian Batholith, which is a ~2000 km long and 120 km wide (on average) plutonic body parallel to the Pacific coastline, with associated smaller satellite intrusions spread along both western and eastern Andean slopes (Orts et al., 2015, and references therein). North to the Chilean Triple Junction, the North Patagonian Batholith includes Middle Jurassic to Miocene rocks of calc-alkaline composition (Castro et al., 2011; Pankhurst et al., 1999) intruding the Upper Paleozoic basement. In this sector the Liquiñe-Ofqui Fault Zone is a major transpressional intra-arc fault system (Figure 3.1b) that accommodates the oblique convergence between the Nazca and South America plates and along which most of the Quaternary volcanism and faulting develop (Hervé, 1994; Cembrano et al., 1996; Rosenau et al., 2006; Vargas Easton et al., 2013). This is an ~ 1000 km long strike-slip fault characterized by dextral motion during the Cenozoic, when it was active within the arc roots in a thermally weakened crust (Cembrano et al., 1996; Lavenu and Cembrano, 1999; Thomson et al., 2010), and by previous left-lateral motion during the Mesozoic, when it favored the emplacement of the Patagonian Cordilleran Batholith

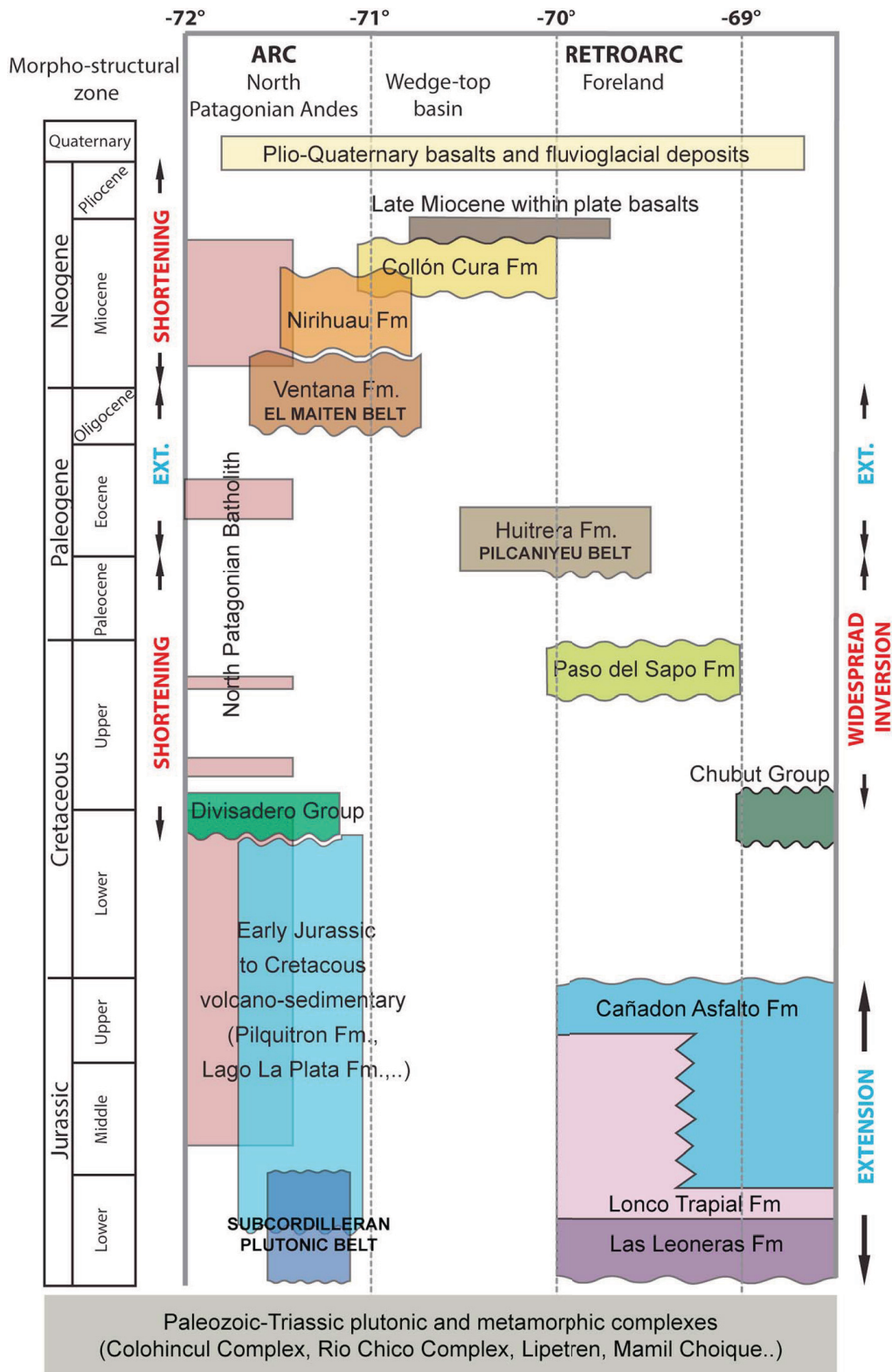(Cembrano et al., 1996; Castro et al., 2011).

Figure 3.2 – Stratigraphic correlations, main magmatic bodies and, tectonic regimes characterizing the various morphostructural domains of the study area.

East of the Liquiñe-Ofqui Fault Zone, the northern Patagonian Cordillera is characterized by a thick-skinned style of thrusting. During Cretaceous-late Paleogene and Neogene shortening phases (Giacosa et al., 2005; Homovc et al., 2011; Orts et al., 2012; Ramos, 1981; Ramos and Cortés, 1984), this type of deformation produced the exhumation of the North Patagonian Batholith and of the igneous-metamorphic basement. Thick-skinned thrusting is related with the reverse fault reactivation of preexisting normal faults and is accompanied by basin inversion (Giacosa and Heredia, 2004a). Reactivated normal faults were originally related with two main extensional stages in the study area: (i) an Early to Middle Jurassic preorogenic stage, accompanied by the accumulation of volcano-sedimentary units in the northern Patagonian Cordillera (Piltriquitrón Formation and equivalents), where interbedded tuff and sedimentary strata were dated as ~197–192 Ma old by U/Pb zircon dating (Orts et al., 2012; Spalletti et al., 2010) and (ii) an Oligocene to early Miocene intraorogenic stage associated with the occurrence of the El Maitén magmatic belt (Rapela et al., 1988). The latter would be related to a regional episode of intra-arc extension affecting the whole Southern Central Andes (Charrier et al., 2002; Godoy et al., 1999; Jordan et al., 2001; Radic et al., 2002). Across the northern Patagonian Andes, these volcanic rocks, interbedded with marine and continental sedimentary rocks (Cazau et al., 1989; Ramos, 1982), have been related to extensional processes, based on geochemistry and structural evidence (Aragón et al., 2011; Bechis and Cristallini, 2006; Bechis et al., 2014; Giacosa and Heredia, 2004b; Rapela et al., 1988). This extensional stage has been unraveled also in the foreland by Mancini and Serna (1989). Early Cretaceous volcanics of calc-alkaline affinity, forming the Divisadero Group (Skármeta and Charrier, 1976; Ramos, 1981; Rapela et al., 1988; Suárez et al., 1996; Suárez and De La Cruz, 2001), cover Jurassic successions and older intrusive rocks in the eastern parts of the northern Patagonian Cordillera. The frontal eastern foothill area, also termed "Precordilleran System" (e.g., Orts et al., 2015), is dominated by Paleozoic basement intruded by the Early Jurassic Subcordilleran Plutonic Belt (Gordon and Ort, 1993). These rocks are covered by roughly coeval volcano-sedimentary successions that were deposited in a NNE trending intra-arc extensional system (Giacosa and Heredia, 2004b; Orts et al., 2012). In this region, two Cenozoic magmatic belts developed, related to extensional intraorogenic events (Giacosa and Heredia, 2004a). The Paleocene to Eocene Pilcaniyeu magmatic belt is characterized by bimodal volcanic rocks ranging from predominant rhyolithic ignimbrite

facies to subordinate andesites and basalts (Mazzoni et al., 1991; Rapela et al., 1988). To the east, the previously mentioned El Maitén magmatic belt (late Oligocene-early Miocene) is characterized by widespread outcrops of andesites and dacitic ignimbrites with subordinate basaltic lava flows and rhyolitic ignimbrites. These two magmatic belts are affected by Cenozoic folds (Ramos et al., 2011; Morabito and Ramos, 2012; Bilmes et al., 2013). Tertiary shortening is particularly well documented by both foreland basin and wedge-top basin synorogenic deposits, which preserve progressive unconformities and effectively record depocenter migration during the Miocene (Ramos et al., 2011; Orts et al., 2012; Bilmes et al., 2013; Echaurren et al., 2016). The overlying flat-lying Pliocene-Pleistocene volcanics, classifying as alkali basalts, basanites, and trachybasalts, indicate a within-plate environment that differs from previous Andean arc-magmatic rocks (Massaferro et al., 2006).

The north Patagonian foreland to the east is dominated by a landscape of faulted basement blocks and intramontane depressions filled by Neogene-Quaternary clastic and volcanic deposits (Bilmes et al., 2013; Echaurren et al., 2016). One of these Neogene-Quaternary depressions, i.e. the Gastre Basin, retraces the Mesozoic rift-related Cañadón Asfalto Basin (Coira et al., 1975; Dalla Salda and Franzese, 1987; Bilmes, 2012). The boundaries of this basin follow regional NW and NNE trending lineaments (Coira et al., 1975). The pre-Jurassic basement of the Cañadón Asfalto Basin consists of granitoids and metamorphic rocks of Carboniferous to Triassic age (Duhart et al., 2002; Pankhurst et al., 2006; von Gosen, 2009) grouped into several lithostratigraphic units. The Cushamen Formation (Volkheimer, 1964) and the Calcatapul Formation (Proserpio, 1978) are part of a metamorphic basement that was intruded by plutonic bodies of the El Platero Formation (Volkheimer, 1964), the Mamil Choique Formation (Ravazzoli and Sesana, 1977) and the Lipetrén Formation (Ravazzoli and Sesana, 1977). The Jurassic-Lower Cretaceous Cañadón Asfalto extensional basin included nonmarine, normal fault-bounded isolated depocenters that were partially inverted during the Cretaceous (Allard et al., 2011; Folguera and Ramos, 2011). In the study area, the infill of the Cañadón Asfalto Basin includes the Early Jurassic Las Leoneras and Lonco Trapial Fms. (radiometrically dated using the zircon Pb/U method by Cúneo et al. [2013]) and the Toarcian to Middle-Late Jurassic Cañadón Asfalto Formation (Pb/U ages of 178.8 ± 0.1 Ma and 157.4 ± 0.6 Ma) (Cúneo et al., 2013). The Cañadón Asfalto Basin has an economic relevance because it

hosts the epithermal world-class polymetallic Ag + Pb (Cu, Zn) Navidad deposit, with resources of 19.670 t Ag; 1,320,000 t Pb; and significant contents of Cu and Zn in eight separate to semicontinuous deposits (Williams, 2010). The Jurassic to Lower Cretaceous succession is unconformably overlain by the Upper Cretaceous to Paleocene marine and continental deposits of the Paso del Sapo and Lefipán Fms. (Lesta and Ferello, 1972). These units, representing the record of the Campanian-Danian transgression (Spalletti and Dalla Salda, 1996), are covered by an Eocene volcanic succession (Cazau et al., 1989) including andesites, dacites, and rhyolites of the Huitrera Formation (Ravazzoli and Sesana, 1977). Stratigraphically overlying Neogene-Quaternary continental deposits are preserved within tectonic depressions (such as the Gastre Basin) and, to a lesser extent, on top of the uplifted fault-bounded blocks.

3.3 Structural constraints from the Gastre-Navidad Area

The map-scale structure of the Gastre-Navidad area (Figures 3.3a and 3.4) is dominated by high-angle faults. Pre-Mesozoic units record internal deformation produced by NE-SW shortening, accompanied by lower greenschist facies metamorphism (von Gosen and Loske, 2004). Map-scale folds are locally well developed in the Mesozoic-Tertiary successions, particularly in the Cañadón Asfalto Fm. Examples of outcrop structural features from the Cañadón Asfalto Fm are shown in Figure 3.5, while orientation data are provided in Figure 3.6. The Cañadón Asfalto Fm. is affected by two sets of faults, striking dominantly NW-SE and NE-SW (Figures 3.6a and 3.6b), often recording a synsedimentary/syndiagenetic extensional activity documented by sediment thickness variations across the faults, disruption of not yet completely lithified beds (Figures 3.5a and 3.5b), and carbonate sediment filling of dilatant structures (hybrid dilation/shear fractures). About 30% of these faults – arguably syndiagenetic in origin – preserve kinematic indicators in the form of striae and/or mineral (dominantly calcite) shear fibers on slickenside surfaces. When slickenlines were present, their pitch has been measured together with sense of shear. These data (Figure 3.6c) have been used to obtain information on the strain field controlling the development of the fault set, using the P-B-T technique (Angelier and Mechler, 1977).
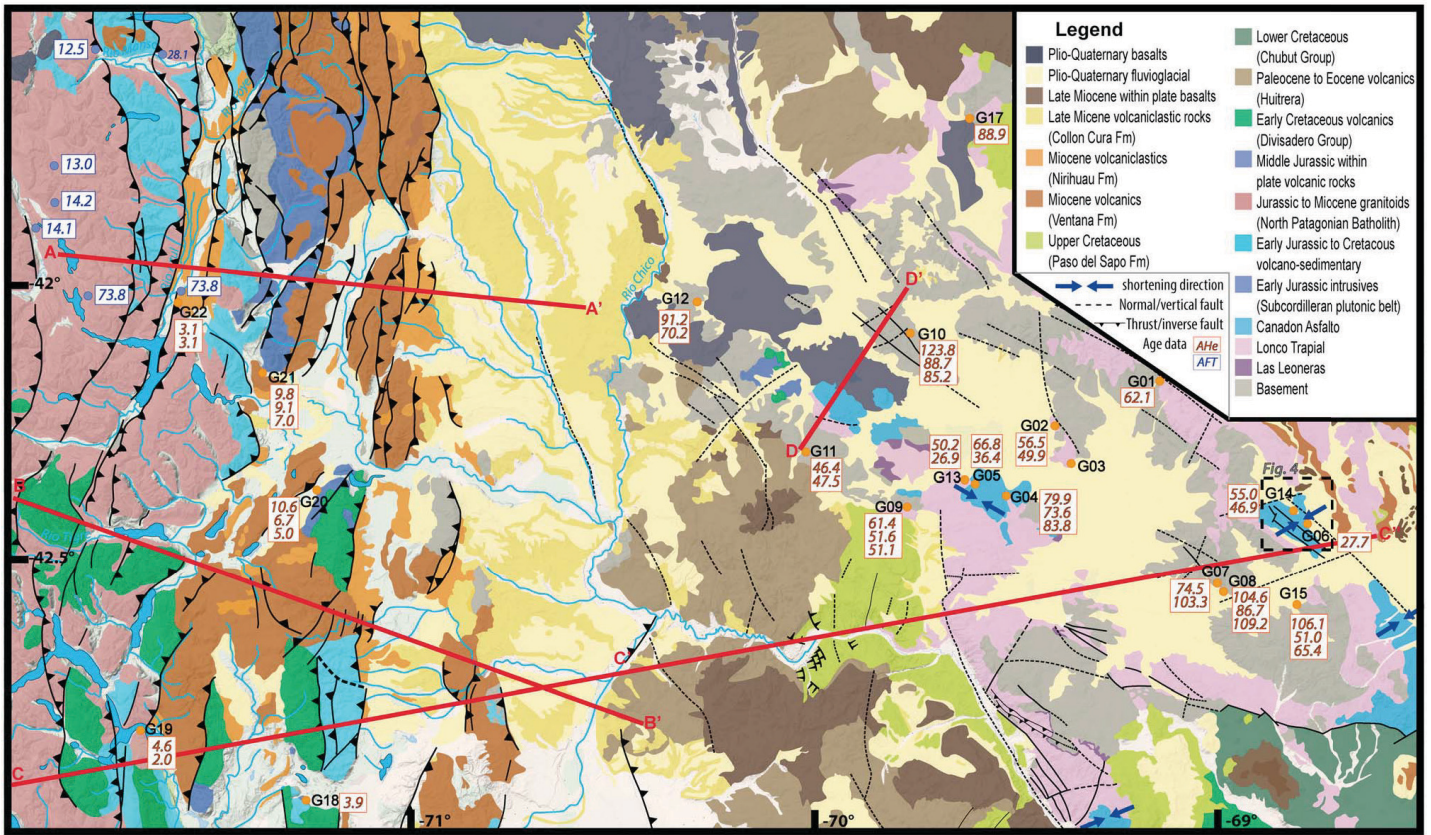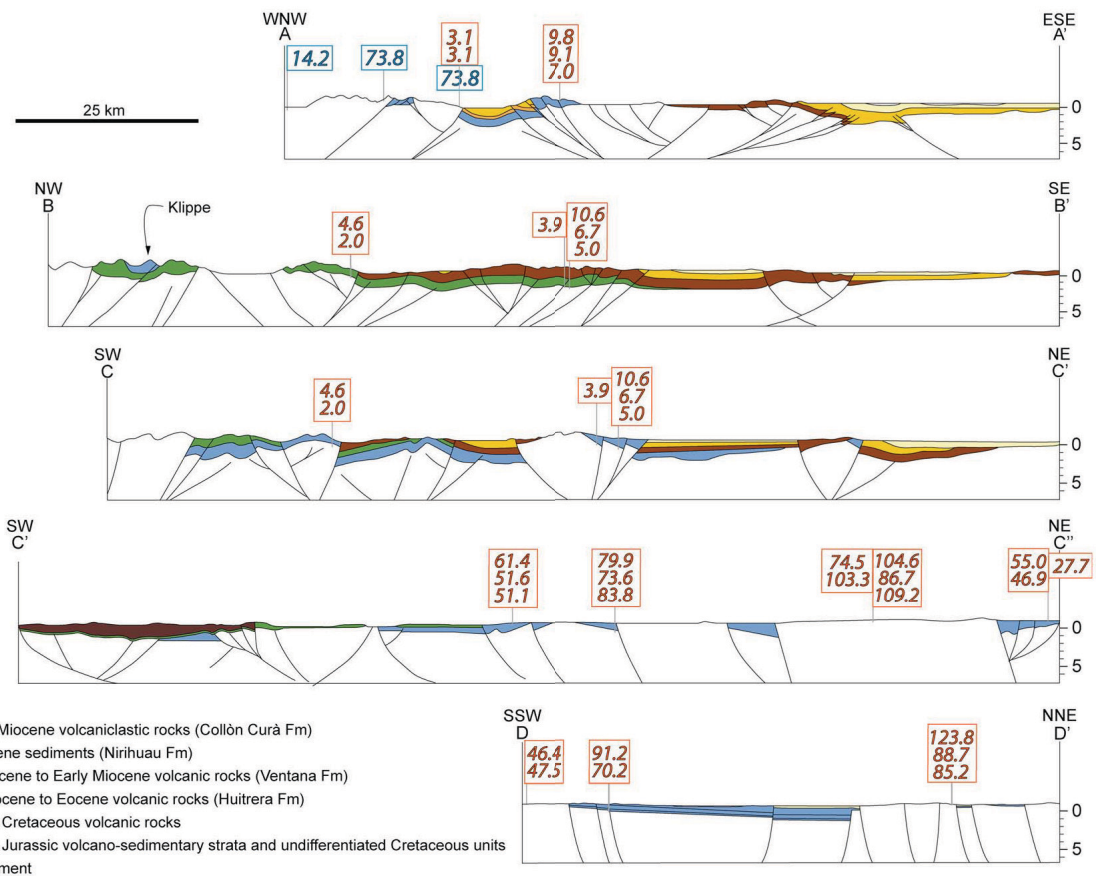
Figure 3.3 (previous page) – (a) Geological map of the study area (based on Ardolino et al. (2009), Lizuaín (2009), Lizuaín and Silva Nieto (2011), Orts et al. (2012), Bilmes et al. (2013), and Orts et al. (2015), integrated with our own field mapping). New apatite (U-Th)/He ages from our samples (G01 to G22; error of 10% at 1σ has to be considered for AHe ages) are shown together with published apatite fission track (AFT) ages (from Thomson et al., 2010). Shortening directions were obtained based on the analysis of the layer-parallel shortening-related structural assemblage (consisting of pressure solution cleavage, veins, and conjugate faults). (b) Cross sections (from Bilmes et al., 2013; Orts et al., 2015; Echaurren et al., 2016), showing projected low-temperature thermochronometric data. As pointed out by the original authors of these geological sections, the structure is dominated by reverse-slip reactivation of preexisting normal faults. Depending on the degree of tectonic inversion, faults may show variable reverse/normal fault separation at different stratigraphic levels. The thickness of the stratigraphic units can also change between footwall and hanging wall blocks of original, synsedimentary normal faults.
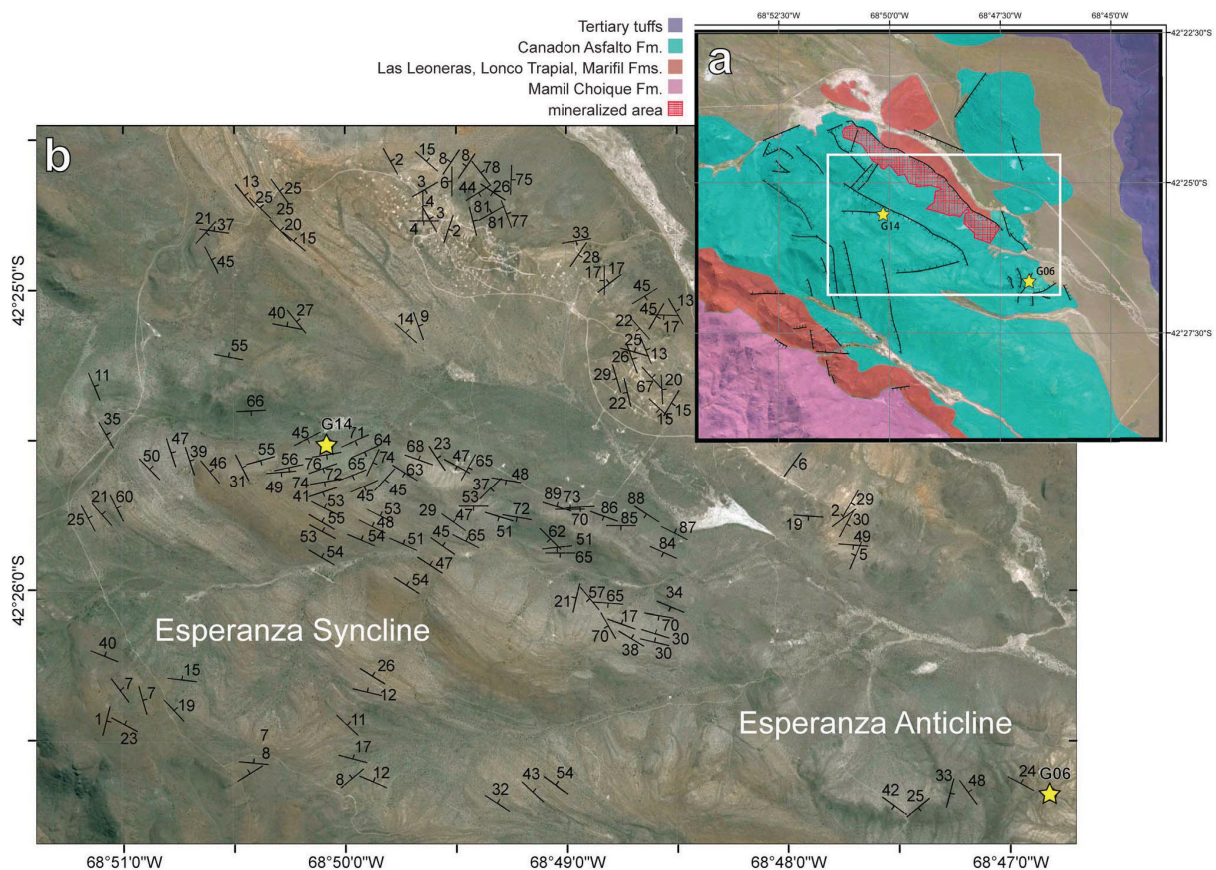
Figure 3.4 – (a) Geological map of the Navidad Project (modified after Williams (2010)), showing location of samples collected in the ore deposit area and (white box) that of the satellite image reporting bedding data gathered in the (b) folded zone of Navidad.

The P-B-T method, based on plane orientation, slip orientation, and kinematics of each single fault, furnishes the three principal axes of strain: P (direction of maximum shortening), T (direction of maximum stretching), and B (intermediate axis, orthogonal to the P-T plane). In order to calculate the orientation of each strain axis, this method uses a common defined fracture angle θ for all fault-slip data. P-B-T axes were determined using FaultKin v.7.4.3 software (Marrett and Allmendinger, 1990; Allmendinger et al., 2012), which utilizes the right dihedra geometrical method of paleostress analysis of Angelier and Mechler (1977) and Pfiffner and Burkhard (1987) (for small-offset faults such as those analyzed in this study, and accepting the Wallace-Bott hypothesis that the slip is parallel to the resolved shear stress [Wallace, 1951; Bott, 1959], the obtained strain axes can be assumed to approximate infinitesimal strain and therefore to represent paleostress principal axes). The analysis unraveled an extensional tectonic regime characterized by a subvertical P axis and a subhorizontal, SW-NE trending T axis (Figure 3.6d). Hydrothermal veins, up to tens of centimeters thick and mainly composed of barite (Figure 3.5c), also occur as dominant NW-SE and NE-SW striking sets (Figures 3.6e and 3.6f). This whole composite fault-vein system appears to control the mineralization in the ore deposit of Navidad, which can be confidently ascribed to the Mesozoic (Jurassic), as already suggested by Williams (2010). The analysis of bedding data from the Cañadón Asfalto Fm. indicates that this is dominated by subhorizontal to gentle dips, although folding is clearly recorded by the distribution of poles to bedding (Figures 3.6g and 3.6h). Bedding attitudes record folding of the Cañadón Asfalto Fm. around a subhorizontal statistical axis at a regional scale. The analysis of bedding distribution around single folds (e.g., Esperanza Syncline and Esperanza Anticline in Figure 3.4) shows how adjacent individual structures may be characterized by slightly different mean axial trends (Figures 3.6i–3.6l). These folds are clearly the result of shortening of the sedimentary succession, as testified by tectonic stylolites (i.e., spaced pressure solution cleavage) at a high angle to bedding in limestones (Figure 3.5f), the bedding-cleavage intersection being roughly parallel to the local fold axis. Calcite-filled extension veins occur perpendicular to the tectonic styolites. The two sets of shortening and extension structures show mutually crosscutting relationships, indicating that they are essentially coeval. Small normal faults also strike parallel to the extension veins.
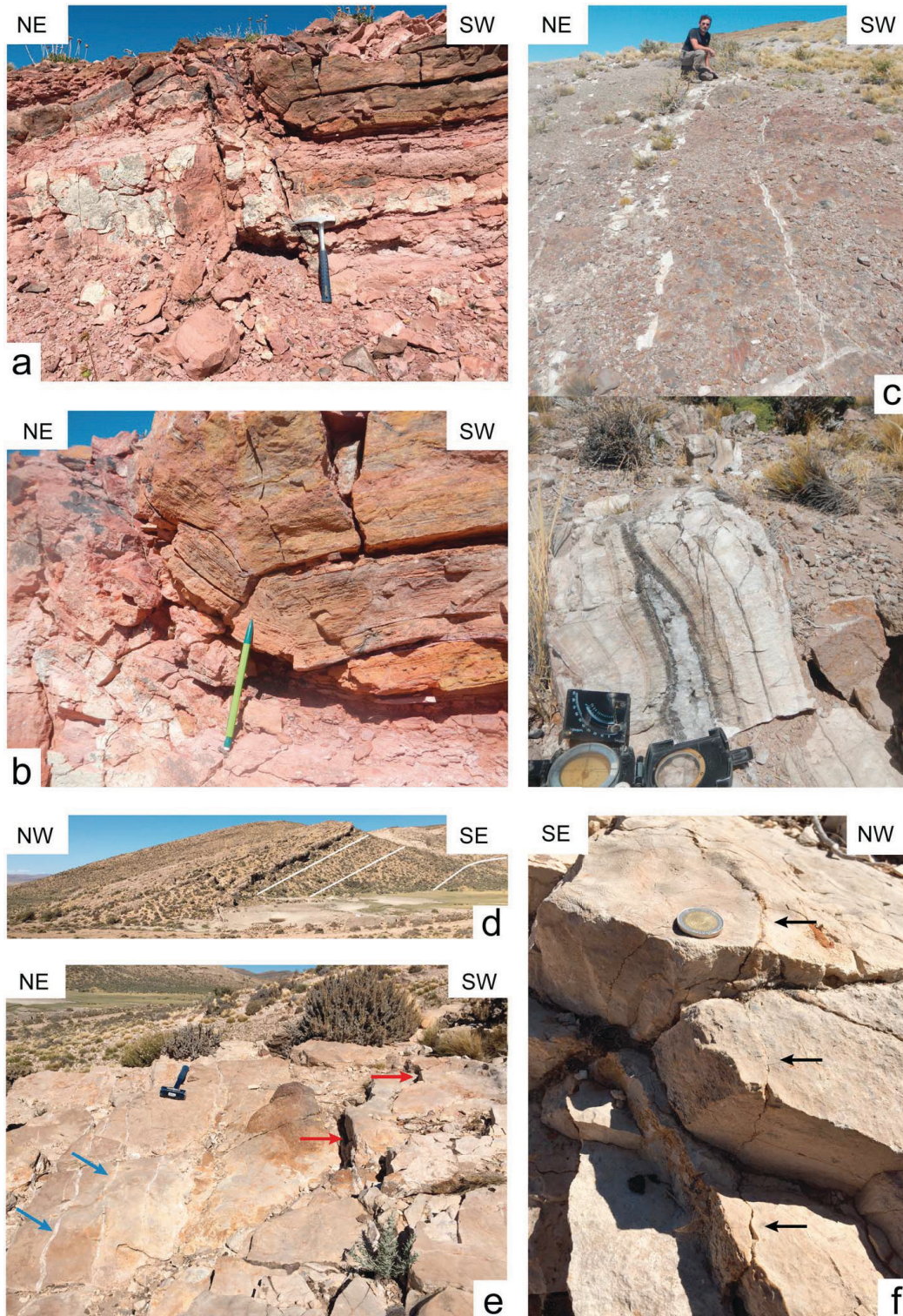
Figure 3.5 – Examples of outcrop structures from the Cañadón Asfalto Fm. (a) Jurassic minor fault showing silicified fault core testifying hydrothermal circulation (Navidad area). (b) Detail of fault hanging wall from Figure 3.5a, showing folded and partially disrupted laminated bed. (c) Barite-bearing hydrothermal veins (Navidad area). (d) NW dipping fold limb in Upper Jurassic limestone beds (about 30 km WSW of Gastre). (e) Outcrop of Upper Jurassic limestone beds on NW dipping fold limb of Figure 3.5d, showing NW striking calcite-filled extension veins (blue arrows) normal to bedding and minor normal faults (red arrows) at a high angle to bedding. (f) Detail of previous outcrop, showing NE striking spaced pressure solution cleavage surfaces (arrowed) normal to bedding.

The tension gashes are parallel to the acute bisector of conjugate normal faults, thus suggesting that these features form part of a single structural association. The whole cleavage-vein-normal fault structural assemblage records mutually orthogonal horizontal maximum ($\sigma 1$) and minimum ($\sigma 3$) compression during layer-parallel shortening preceding fold amplification, a stress configuration that is typical of prethrusting foreland shortening (Tavani et al., 2015) and is also consistent with the evidence of syncontractional, perpendicular extension in the foreland of the Patagonian Andes at a more regional scale (Gianni et al., 2015a). The layer-parallel shortening-related structural assemblage has been used to obtain shortening directions for various sites within the study area (displayed in Figure 3.3a). Although bedding data are somewhat dispersed (Figures 3.6g–3.6l), individual folds are relatively simple, subcylindrical (Ramsay and Huber, 1987) structures accompanied by a single generation of related cleavage. Therefore, variable fold trends appear not to be the result of superposed folding events. Rather, it may envisaged that shortening of the Cañadón Asfalto Basin occurred by buttressing of the sedimentary infill against basement blocks representing the footwall of Mesozoic rift-related normal faults, thus resulting in variable fold trends being controlled by the inherited, complex basin architecture. This style of shortening and the related variability of maximum shortening directions (Figure 3.3a) are consistent with the tectonic inversion already documented for this foreland sector, which is termed broken foreland because of this type of deformation dominated by double-vergent structures controlled by the reactivation of preexisting normal faults (e.g., Folguera and Ramos, 2011; Orts et al., 2012, 2015) (refer to the cross sections in Figure 3.3b).
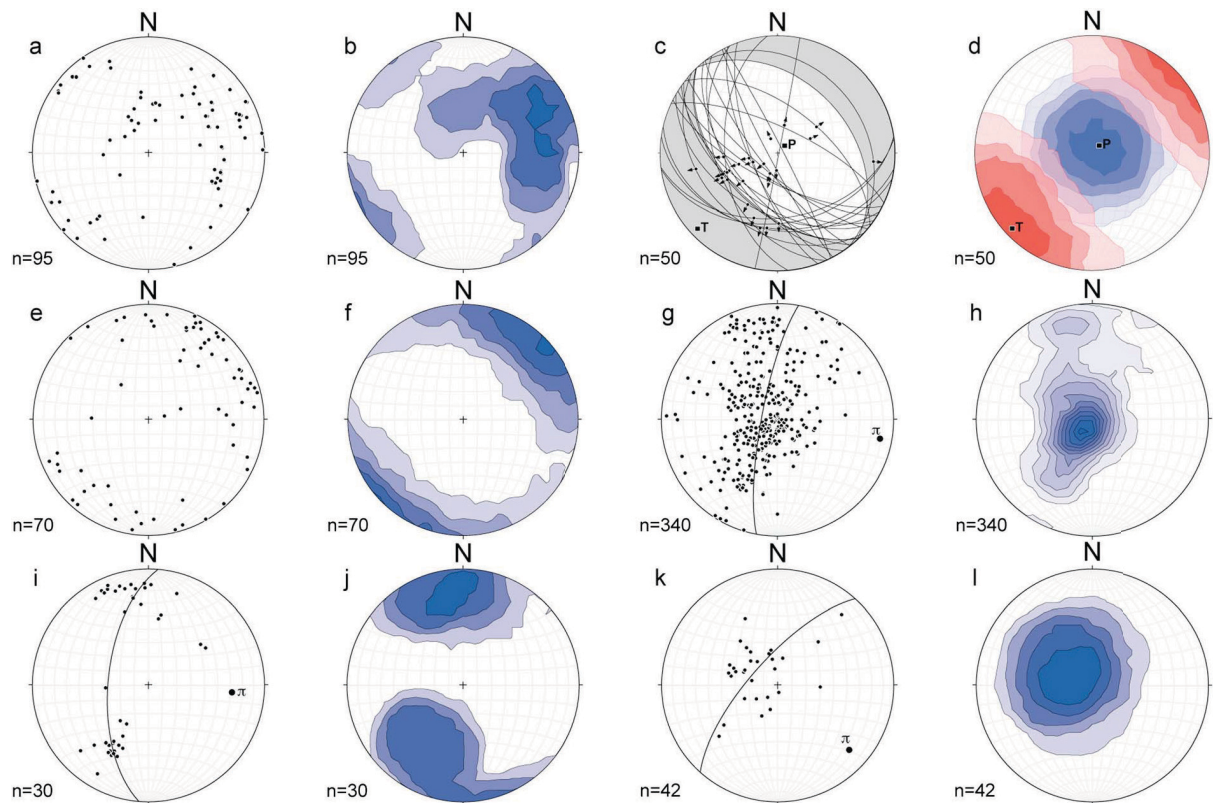
Figure 3.6 – Orientation data (lower hemisphere, equal area projections of poles to planes drawn using Stereonet v.9.5.1 software) (Allmendinger et al., 2012; Cardozo and Allmendinger, 2013) for the Gastre area. All contours are drawn using the Kamb method with intervals at 2σ and significance level of 3σ. (a) Extensional faults showing evidence of synsedimentary/syndiagenetic activity. (b) Contour plot of data shown in Figure 3.6a. (c) Subset of the fault population plotted in Figure 3.6a, showing faults preserving slickenlines (arrows) and reliable shear sense indicators. Fault plane solution obtained by kinematic analysis performed with FaultKin v.7.4.3 software (Marrett and Allmendinger, 1990; Allmendinger et al., 2012) is also shown (grey shaded "beach ball"). (d) Contours of P (blue) and T (red) axes obtained from the kinematic analysis shown in Figure 3.6c. (e) Hydrothermal veins. (f) Contour plot of data shown in Figure 3.6e. (g) Bedding in the Cañadón Asfalto Fm. (h) Contour plot of data shown in Figure 3.6g. (i) Bedding from the Esperanza Syncline (refer to Figure 3.3). (j) Contour plot of data shown in Figure 3.6i. (k) Bedding from the Esperanza Anticline (refer to Figure 3.3). (l) Contour plot of data shown in Figure 3.6k. For diagrams in Figures 3.6g, 3.6i, and 3.6k, the best fit great circle approximating data distribution is shown, together with its pole (π) representing the statistical fold axis.

3.4 Apatite (U-Th)/He Thermochronometry

In order to analyze and compare the tectonic evolution and exhumation of the frontal part of the east vergent northern Patagonian Andes and of the adjacent foreland, a transect has been selected from the eastern slope of the Cordillera to the area of the Gastre Basin (reaching a longitude of ~68.5°W), thereby including the Navidad silver deposit.

3.4.1 Materials and Methods

Collected samples can be included into two main groups (see Table 3.1 for details). A first group comprises the samples gathered from the foreland area. Samples G01, G02, G04, G07, G08, G10, G11, G12, G15, and G17 were collected from basement rocks cropping out in uplifted fault blocks bounding the Gastre Basin (Figure 3.3a). These granitoid samples are from the Lipetren Fm. (Lower Paleozoic) and the Mamil Choique Fm (Permo-Triassic). Samples G5, G6, G9, G13, and G14 were collected from the Cañadón Asfalto Fm. (Upper Jurassic). In particular, samples G6 and G14 are from the ore deposit district of Navidad. A second group of samples (G18, G19, G20, G21, and G22) includes those gathered in the western part of the study area, from the Leleque and El Maiten Ranges, constituting the frontal part (i.e., the so-called Precordillera System) of the northern Patagonian Andes.

(U-Th)/He (AHe) ages have been obtained from carefully selected apatite grains with a minimum width of 60 μm, which have been measured along the two axes on two faces and then placed into a Niobium basket. One to three replicates have been analyzed per sample. Sphere equivalent radius, weight, and ejection factors have been determined, assuming a homogeneous distribution of U and Th in apatite, using dedicated software (Gautheron and Tassan-Got, 2010; Ketcham et al., 2011; Gautheron et al., 2012). The Niobium baskets have been heated twice using a diode laser at 1030 ± 50°C for 5 min, allowing for total He degassing and to check the presence of He trapped in small inclusions (see Fillon et al. [2013] for more details). After He extraction, Nb baskets were placed into single-used polypropylene vials. Apatite grains were dissolved for 3 hours at 70°C in a 50 μL HNO_3 5N- solution containing a known content of 235U, 230Th, and 149Sm, and additional 50 μL HNO_3 5N- and then filled with 0.9 mL of ultrapure MQ water.

Sample name	Coordinates		Elevation	Lithology	Formation	Stratigraphic Age
	Latitude	Longitude				
G01	42°11'34"	69°09'56"	1134	granite	Lipetren	(Permo-)Triassic
G02	42°15'57"	69°24'31"	929	granite	Mamil Choique	Lower Paleoz. to Lower Permian
G03	42°20'17"	69°22'32"	958	granite	Lipetren	Permo-)Triassic
G04	42°23'16"	69°31'19"	997	granite	Mamil Choique	Lower Paleoz. to Lower Permian
G05	42°22'10"	69°37'45"	963	conglomerate	Cañadón Asfalto	Upper Jurassic
G06	42°26'40"	68°46'49"	1150	arkose	Cañadón Asfalto	Upper Jurassic
G07	42°33'35"	69°00'14"	1070	granite	Mamil Choique	Lower Paleoz. to Lower Permian
G08	42°33'50"	69°00'15"	1043	granite	Mamil Choique	Lower Paleoz. to Lower Permian
G09	42°24'47"	69°46'56"	995	arkose	Cañadón Asfalto	Upper Jurassic
G10	42°05'43"	69°46'30"	1060	granite	Mamil Choique	Lower Paleoz. to Lower Permian
G11	42°18'41"	70°02'12"	999	granite dyke	Mamil Choique	Lower Paleoz. to Lower Permian
G12	42°02'07"	70°17'57"	976	granite	Mamil Choique	Lower Paleoz. to Lower Permian
G13	42°22'25"	69°36'14"	973	sandstone	Cañadón Asfalto	Upper Jurassic
G14	42°25'31"	68°50'05"	1177	sandstone	Cañadón Asfalto	Upper Jurassic
G15	42°35'10"	68°48'46"	1103	granite	Mamil Choique	Lower Paleoz. to Lower Permian
G16	42°35'18"	69°44'05"	534	sandstone	Passo del Sapo	Upper Cretaceous
G17	41°42'43"	69°37'09"	1275	granite	Mamil Choique	Lower Paleoz. to Lower Permian
G18	42°55'50"	71°15'38"	617	granite	Subcordilleran Plutonic Belt	Lower Jurassic
G19	42°48'23"	71°39'39"	576	granitoid	Batolite Patagonico	Upper Cretaceous
G20	42°23'05"	71°14'43"	663	granite	Leleque	Upper Jurassic
G21	42°10'02"	71°21'26"	616	granodiorite	Subcordilleran Plutonic Belt	Lower Jurassic
G22	42°01'49"	71°34'34"	275	granite	Batolite Patagonico	Upper Cretaceous

Table 3.1 – Sample Location (With Formation and Stratigraphic Age)

The final solution was measured for U, Th, and Sm concentrations by quadrupole inductively coupled plasma (ICP-quadrupole) mass spectrometry (CCT Thermo-Electron at LSCE, Gif/Yvette, France). The analysis was calibrated using external age standards, including Limberg Tuff and Durango apatites. A mean AHe age of 16.0 ± 1.4 Ma and 31.1 ± 2.1 Ma has been measured for the Limberg Tuff and yellow Durango apatite, respectively, which are in agreement with published data (i.e., 16.8 ± 1.1 Ma and 31.0 ± 1.0) (Kraml et al., 2006; McDowell et al., 2005). An error at 10% at 1σ should be considered, reflecting the sum of ejection factor FT correction and standard dispersion. The HeFTy software (Ketcham, 2005) was used to generate an inverse thermal modeling based on AHe data of four representative samples (G07, G13, G15, and G22), in order to test plausible thermal histories. We chose three samples belonging to the broken foreland area, for which there

is a complete lack of low-T thermochronological studies, and one from the Precordillera. Two to three AHe replicates were used for each modeled sample. The RDAAM model of Flowers et al. (2009) was adopted for the calibration of kinetic parameters, and Ketcham et al. (2011) was considered for the approximation of stopping distances. However, similar results would have been obtained by the use of the damage and annealing model from Gautheron et al. (2009). Surface temperature was assumed to be 10℃. The only constrains used were the following: (i) temperatures between 0 and 20° C during the depositional age for the sedimentary sample (G13) and (ii) temperatures between 0 and 20℃ for basement samples (G07 and G15), corresponding to their near-surface exposure during Triassic times (marked by an unconformity followed by the deposition of the volcano-sedimentary succession of the Garamilla Fm.). No constraints were imposed for sample G22, as its intrusion age is much older than the recorded AHe age.

Sample name	Rs (µm)	Weight (µg)	FT	⁴He (nncc/g)	U (ppm)	Th (ppm)	Sm (ppm)	eU (ppm)	Th/U	AHe age (Ma)	AHe age c FT (Ma)	S (Ma)
G01-01	*48*	*2.7*	*0.73*	*187819.6*	*5*	*26*	*258*	*12*	*4.9*	*113.9*	*155.4*	*14.0*
G01-02	38	1.7	0.64	481259.6	91	31	151	98	0.3	40.0	**62.1**	**5.6**
G01-03	*43*	*1.8*	*0.72*	*361294.1*	*7*	*25*	*281*	*13*	*3.7*	*203.3*	*282.3*	*25.4*
G02-01	*37*	*1.2*	*0.71*	*171320.0*	*38*	*126*	*177*	*68*	*3.4*	*20.5*	*29.0*	*2.6*
G02-02	41	1.8	0.72	159254.4	18	59	82	32	3.3	40.6	**56.5**	**5.1**
G02-03	35	0.9	0.66	70897.9	9	20	486	14	2.2	33.0	**49.9**	**4.5**
G04-01	53	3.8	0.79	204917.2	21	22	66	27	1.0	62.7	**79.9**	**7.2**
G04-02	41	1.4	0.71	257276.9	32	33	97	40	1.0	51.9	**73.6**	**6.6**
G04-03	44	1.6	0.68	729467.2	83	96	17	105	1.2	57.3	**83.8**	**7.5**
G05-01	50	2.9	0.79	268589.4	45	46	75	56	1.0	39.5	**50.2**	**4.5**
G05-03	46	1.8	0.75	116142.7	43	20	65	47	0.5	20.1	**26.9**	**2.4**
G06-01	*64*	*6.0*	*0.83*	*75773.9*	*5*	*19*	*62*	*10*	*3.5*	*59.9*	*72.2*	*6.5*
G06-02	*51*	*3.2*	*0.75*	*59613.4*	*5*	*37*	*184*	*14*	*7.0*	*31.8*	*42.2*	*3.8*
G06-03	55	3.5	0.78	70495.9	22	19	66	27	0.9	21.6	**27.7**	**2.5**
G07-01	52	2.6	0.73	1256944.8	134	3	152	135	0.0	76.5	**104.6**	**9.4**
G07-02	43	2.2	0.68	473128.2	65	3	106	66	0.1	58.8	**86.7**	**7.8**
G07-03	55	3.4	0.75	1587006.9	159	9	66	161	0.1	81.4	**109.2**	**9.8**
G08-01	39	1.9	0.69	113056.0	15	8	133	17	0.5	51.4	**74.5**	**6.7**
G08-03	31	0.9	0.65	245288.5	26	11	155	29	0.4	66.9	**103.3**	**9.3**
G09-01	32	0.5	0.57	260075.3	33	89	933	54	2.7	35.1	**61.4**	**5.5**
G09-02	33	0.9	0.63	124150.0	19	50	141	31	2.7	32.3	**51.6**	**4.6**
G09-03	43	1.6	0.68	149903.5	19	67	58	36	3.4	34.6	**51.1**	**4.6**
G10-01	90	15.2	0.86	207920.9	14	7	48	16	0.5	106.5	**123.8**	**11.1**
G10-02	77	8.8	0.85	172830.1	17	6	29	19	0.3	75.1	**88.7**	**8.0**
G10-03	60	4.5	0.79	163455.5	18	7	83	19	0.4	67.6	**85.2**	**7.7**
G11-02	38	1.3	0.69	89896.4	17	22	98	23	1.2	31.8	**46.4**	**4.2**
G11-03	43	1.6	0.72	40621.0	8	3	114	9	0.4	34.1	**47.5**	**4.3**
G12-01	53	3.9	0.78	170929.5	15	17	104	19	1.1	71.4	**91.2**	**8.2**

G12-02	52	3.3	0.76	348509.6	50	13	159	53	0.3	53.3	**70.2**	**6.3**
G13-02	58	3.9	0.80	239706.7	27	40	51	37	1.5	53.3	**66.8**	**6.0**
G13-03	70	7.0	0.82	28134.2	3	15	79	7	4.4	30.0	**36.4**	**3.3**
G14-01	58	3.9	0.79	291854.3	35	83	61	56	2.4	43.3	**55.0**	**4.9**
G14-03	54	4.1	0.77	357806.4	64	74	89	82	1.2	36.1	**46.9**	**4.2**
G15-01	38	0.9	0.63	180970.1	10	44	204	21	4.4	67.2	**106.1**	**9.5**
G15-02	41	4.1	0.77	26296.8	3	11	52	5	4.3	39.2	**51.0**	**4.6**
G15-03	45	1.6	0.69	65107.3	5	23	135	11	4.3	44.9	**65.4**	**5.9**
G17-01	*40*	*1.4*	*0.70*	*191922.0*	*23*	*70*	*139*	*40*	*3.1*	*39.3*	*56.1*	*5.0*
G17-02	*52*	*3.7*	*0.78*	*353668.2*	*27*	*7*	*93*	*29*	*0.3*	*99.4*	*127.9*	*11.5*
G17-03	35	1.1	0.65	206061.0	25	13	126	28	0.5	58.1	**88.9**	**8.0**
G18-01	*35*	*0.9*	*0.65*	*36311.0*	*18*	*47*	*355*	*29*	*2.6*	*9.4*	*14.5*	*1.3*
G18-02	47	2.5	0.73	42608.5	103	83	208	123	0.8	2.8	**3.9**	**0.4**
G19-02	42	1.8	0.71	20037.8	26	95	249	49	3.6	3.3	**4.6**	**0.4**
G19-03	39	1.3	0.69	11635.1	53	61	236	68	1.1	1.4	**2.0**	**0.2**
G20-01	42	1.5	0.67	20451.3	11	50	164	23	4.7	7.2	**10.6**	**1.0**
G20-02	36	0.9	0.68	12081.7	13	33	140	21	2.5	4.5	**6.7**	**0.6**
G20-03	51	3.3	0.73	5681.2	6	24	85	12	3.8	3.7	**5.0**	**0.5**
G21-01	20	0.9	0.61	41763.5	51	25	152	57	0.5	5.9	**9.8**	**0.9**
G21-02	37	1.1	0.64	32364.8	38	30	237	45	0.8	5.8	**9.1**	**0.8**
G21-03	44	1.9	0.73	16467.8	23	14	79	26	0.6	5.1	**7.0**	**0.6**
G22-01	*33*	*0.6*	*0.58*	*77499.1*	*87*	*188*	*300*	*133*	*2.2*	*4.8*	*8.2*	*0.7*
G22-02	45	1.5	0.69	33055.7	84	185	70	129	2.2	2.1	**3.1**	**0.3**
G22-03	46	2.0	0.73	19459.8	45	109	127	71	2.4	2.2	**3.1**	**0.3**

Table 3.2 – Apatite (U-Th-Sm)/He Analytical Data; FT is the ejection correction factor and Rs is the sphere equivalent radius of hexagonal crystal with the same surface/volume ratio, which are both determined by using a dedicated code (Gautheron and Tassan-Got, 2010; Ketcham et al., 2011; Gautheron et al., 2012). AHe ages are corrected for the FT factor and an error at 1σ is considered.

3.4.2 Results and Thermal Modeling

The determined AHe data for each replicate are reported in Table 3.2. AHe ages and effective uranium content (eU = U + 0.24 Th) present a broad distribution ranging from 2.0 ± 0.2 to 282.3 ± 25.4 Ma and eU range from low to quite high values (3 to 159 ppm). Most of the samples gave ages that will be considered in the following discussion. On the other hand, a few replicates have been rejected because they yielded critically high Th/U values,

probably due to U or Th-rich (i.e., uraninite or thorite) undetectable inclusions.

The data set presents two different AHe age trends, with a sample group (G18 to 22, sampled along the Precordillera mountain front) characterized by "young" ages (~2 to 10 Ma) and a second one (G1 to 17, sampled in the foreland) characterized by "old" ages (reaching ~110 Ma; Table 3.2).

The foreland samples, from both Permian-Triassic plutonic rocks and Mesozoic continental sediments of the Cañadón Asfalto Formation, present for a few replicates some dispersion in AHe ages that depends on factors affecting He diffusion kinetics (eU content and crystal size; Figure 3.8b). This AHe age dispersion reflects a long permanence in the He-Partial Retention Zone (HePRZ). In those conditions, He diffusivity can be different for each grain, implicating closure temperatures ranging from 40 up to 120°C (Reiners and Farley, 2001; Gautheron et al., 2009; Flowers et al., 2009; Djimbi et al., 2015). Based on the AHe data, it may be inferred that the samples from the foreland area stayed in the HePRZ since at least ~110 Ma, with a final exhumation phase at ~30–50 Ma. More information could be extracted from thermal modeling performed using the HeFTy software. Figure 3.7 shows the possible scenarios of thermal paths experienced by samples G07 and G15 (Mamil Choique Fm.), G13 (Cañadón Asfalto Fm.), and G22 (North Patagonian Batholith). The first two samples consist of Paleozoic basement rocks that, based on stratigraphic constraints (Lizuaín and Silva Nieto, 2011), probably experienced burial since ~250 Ma. These two samples show similar path envelopes characterized by a long residence in the HePRZ (between 40 and 80°C), and possibly below it, followed by slow exhumation since ~120 Ma (Figures 3.7a and 3.7c). The Cañadón Asfalto sample (G13) experienced a shorter residence after its burial, with subsequent exhumation starting at ~100 Ma (Figure 3.7b). All these modeled samples do not show any evidence of more recent substantial reheating.
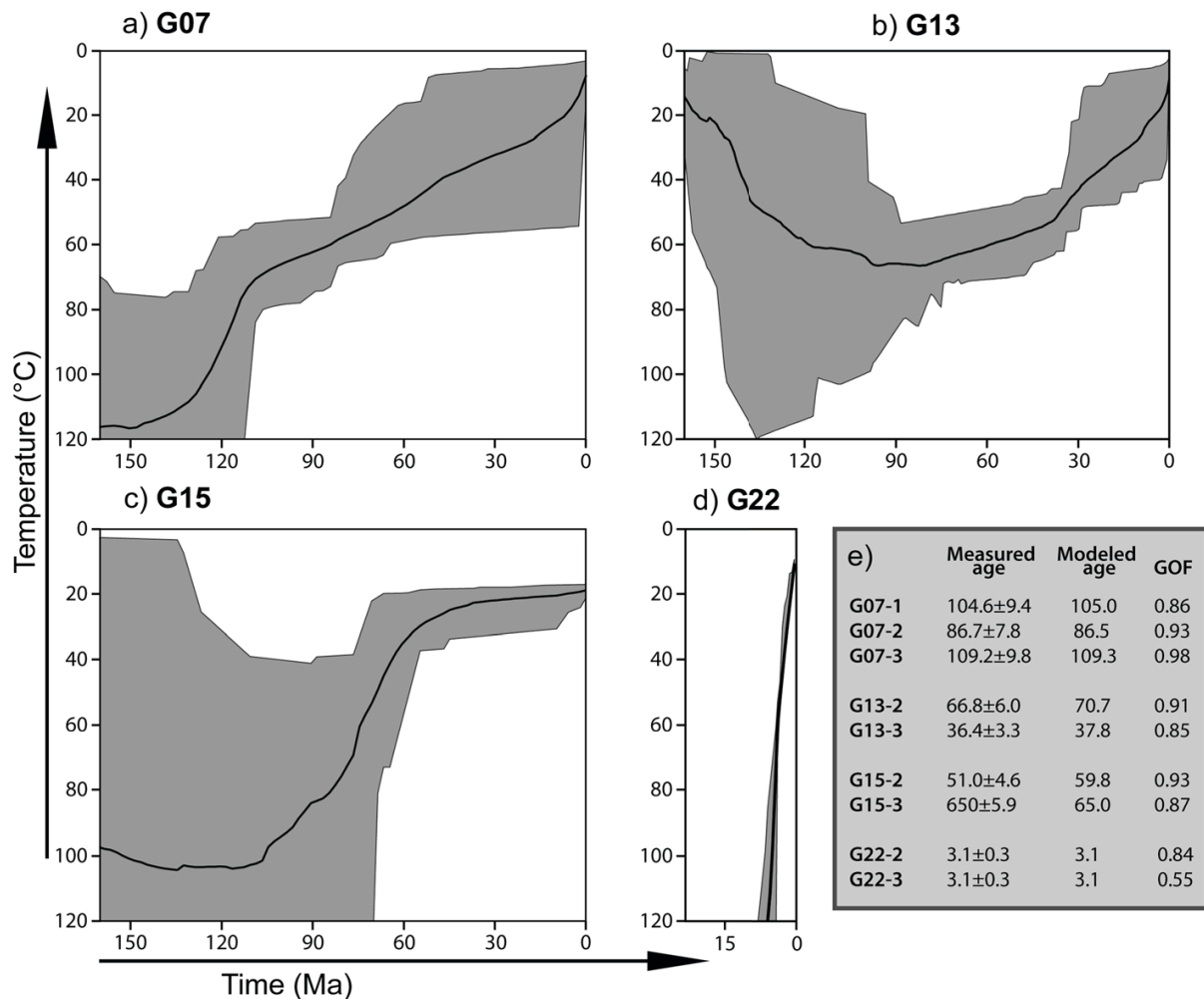
Figure 3.7 – Thermal modeling (performed with the HeFTy software) (Ketcham, 2005) for foreland samples (a) G07, (b) G13, and (c) G15, and (d) Precordilleran sample G22. Good path envelope (supported by the data) and best fitting path are indicated with dark grey areas and a black solid line, respectively. (e) Table summarizing measured age, modeled age, and goodness of fit (GOF) for each considered grain. Age GOF provides an indication of the fit between observed and predicted data (values close to 1 are best).

On the other hand, the thrust belt samples (G18 to G22), collected from Early Jurassic magmatic rocks of the Subcordilleran Plutonic Belt, show a more recent exhumation phase between 10 Ma and 2 Ma, as indicated also by the thermal modeling performed for sample G22 (Figure 3.7d). The long permanence in the HePRZ of some samples is confirmed by the age-elevation relationships (AER; Figure 3.8a). A first group of data cluster around 650 m of elevation and are characterized by ages younger than 10 Ma. A second subset of ages are localized at elevations between ~ 900 and 1250 m and are characterized by very dispersed ages, spanning from 30 to 120 Ma. The main difference between these two groups of ages can be ascribed to the time spent by the samples in the

HePRZ: a rapid cooling though this zone characterized the Precordilleran samples, while a prolonged residence is recorded by the broken foreland samples. In other words, the analyzed foreland area represents a paleo-HePRZ that was brought to surface by exhumation.

Figure 3.8 – (a) Age-elevation relationships (AERs) for AHe data; samples used for thermal modeling are highlighted. (b) AHe ages plotted against effective uranium concentration (eU = [U] + 0.235 × [Th]).

3.5 Discussion

The foreland sector at the latitudes of our study area exposes Late Paleozoic to Jurassic successions that were affected by rifting during Jurassic times (e.g., Folg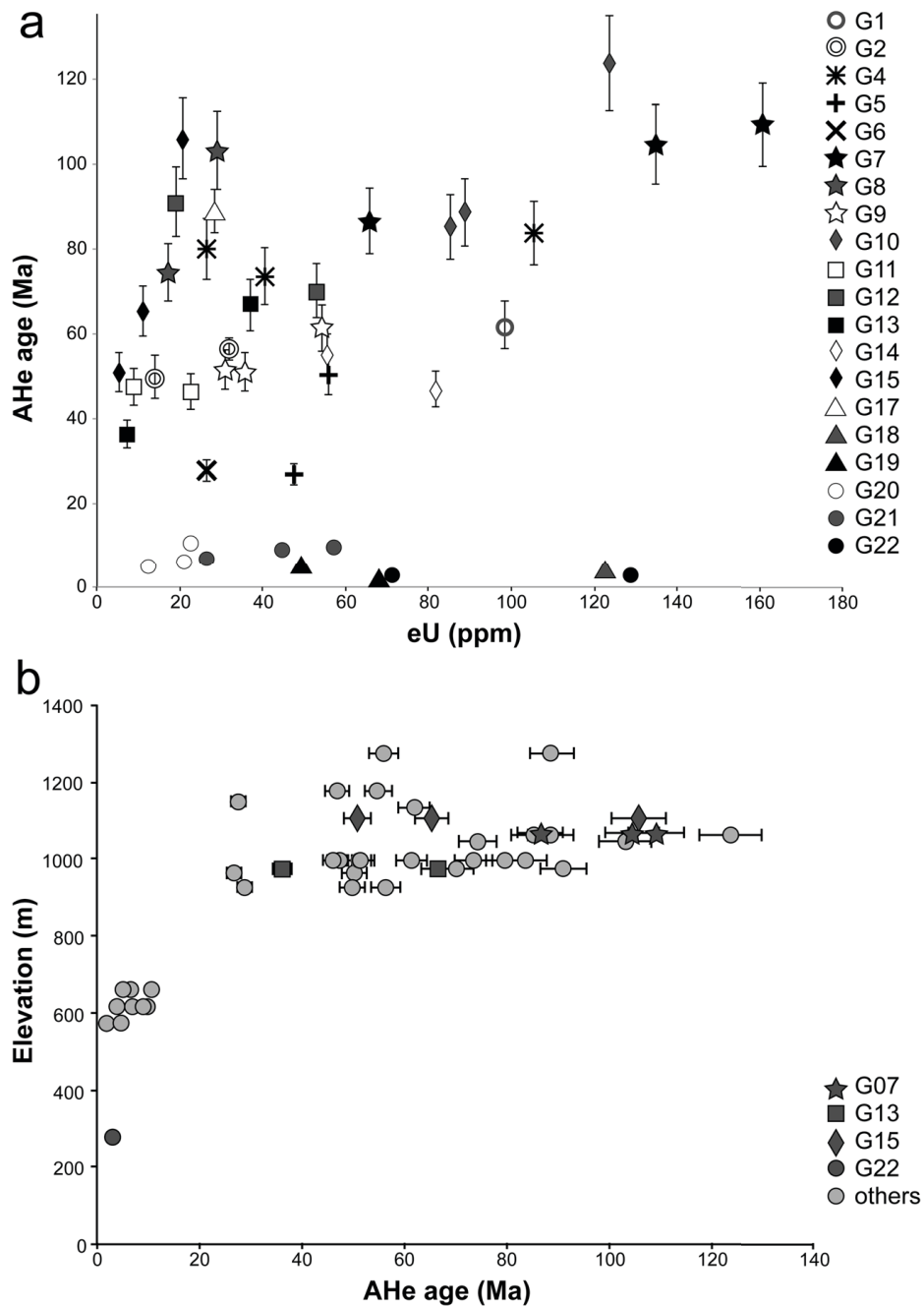uera and Ramos, 2011). Synsedimentary normal faults and hydrothermal veins, also controlling the mineralization in the Navidad ore deposit, provide a structural record of such Mesozoic extension in the study area (refer to Figures 3.5 and 3.6). Subsequent shortening of this foreland sector has been widely documented (e.g., Folguera and Ramos, 2011; Bilmes et al., 2013; Gianni et al., 2015a, 2015b; Echaurren et al., 2016) and has resulted in the folds affecting the succession of the Cañadón Asfalto Basin analyzed in this study (refer to the section on structural data). The new AHe ages obtained in this study, being consistently younger than stratigraphic age of the sampled units (Tables 3.1 and 3.2), provide evidence for burial conditions sufficient to completely reset the AHe system that is in the range of 2.5–3.5 km (see below). Indeed, the presence of a few thousands of meters of burial is consistent with tectonic stylolite formation and folding of competent units of the Cañadón Asfalto succession (refer to Figures 3.5 and 3.6). Had such folding occurred during the Miocene, the removal of the overlying burial would be recorded by recent (i.e., Miocene or younger) AHe ages. Yet AHe ages obtained in this study point to a Late Cretaceous to Paleogene major tectonic inversion and exhumation stage, in agreement with a regional shortening stage that has been documented for the whole Patagonian Andes and its foreland, which lasted from circa 125 Ma to circa 56 Ma at the latitudes of this study (Gianni et al., 2015b). The plate-scale extent of this major shortening stage is testified by fault reactivation and mild inversion occurring in Cretaceous times over various parts of the foreland area, as far as the Atlantic offshore (Continanzia et al., 2011; Micucci et al., 2011). This suggests that the Cretaceous-Eocene inversion has been by far the dominant shortening event in the Gastre foreland sector and that the role and extent of Miocene inversion (e.g., Bilmes et al., 2013) are rather subordinate. The reduced role of Miocene inversion is in good agreement with a recent study by Gianni et al. (2015b), who suggested that the latest stages of Andean deformation and broken foreland reactivation during the Neogene (19.0–14.8 Ma) proposed by Bilmes et al. (2013) may have not been as strong as the Cretaceous-Paleogene event. Moreover, slightly tilted and locally gently folded 21.0 to 16.1 Ma old Miocene sediments documented by Bilmes et al. (2013) are unconformable with respect to intensely shortened Cañadón Asfalto strata that lower

down in the succession, and the inferred reverse faults involving Miocene sediments drawn by the same authors in the Gastre area display vertical separations of a few hundreds of meters at most. Indeed, normal faulting appears to have mostly controlled the development of the various depocenters – including Miocene ones – in the Gastre area, whose structure has been consistently interpreted by von Gosen and Loske (2004) as "the result of (several stages of) downfaulting of different blocks that led to the formation of distinct young basins." On the other hand, preserved Late Cretaceous apatite fission track ages in the northern Patagonian Andes (Thomson et al., 2010) (Figure 3.3a) confirm that the regional Cretaceous-Paleogene shortening stage produced exhumation over the entire thrust belt-foreland system at these latitudes, despite being partially obliterated by Neogene rejuvenation of thrusting and unroofing in the frontal part of the thrust belt sector of the study area.

The AHe ages obtained from the thrust belt sector of the study area, ranging from 8.2 ± 0.9 Ma to 2.4 ± 0.2 Ma, are consistent with the regional Neogene exhumation event described by Folguera and Ramos (2011). AHe ages are generally younger than apatite fission track ages available for the study area (Figures 3.3a and 3.3b), thus being fully consistent with published thermochronological results. These two thermochronological methods provide information related to depths from 2.5 to 5 km, assuming geothermal gradient values of 20–25° C km 1 (Jordan et al., 1989; Coughlin et al., 1998; Carrapa et al., 2008; Collo et al., 2011; Dávila and Carter, 2013) and well-established closure temperatures for the two systems (Ketcham, 1999; Gautheron et al., 2009; Flowers et al., 2009; Djimbi et al., 2015). Therefore, our data provide an effective record of the previously unconstrained final stages of exhumation in the study area. The integration of our AHe data with published apatite fission track ages indicates that, in the thrust belt sector of the study area, exhumation from 4.5 to 6.0 km depths started mainly during the Middle Miocene and continued through the uppermost 2.5–3.5 km of the crust mostly in Late Miocene to Pliocene times. Exhumation rates can be roughly estimated at 0.3 km/Myr for the Middle Miocene and then they raised at about 1.5 km/Myr. The recorded exhumation in the frontal part of the east vergent orogen correlates well with the Neogene shortening event well documented for this area (Ramos et al., 2011; Folguera and Ramos, 2011; Orts et al., 2012, 2015; Echaurren et al., 2016).
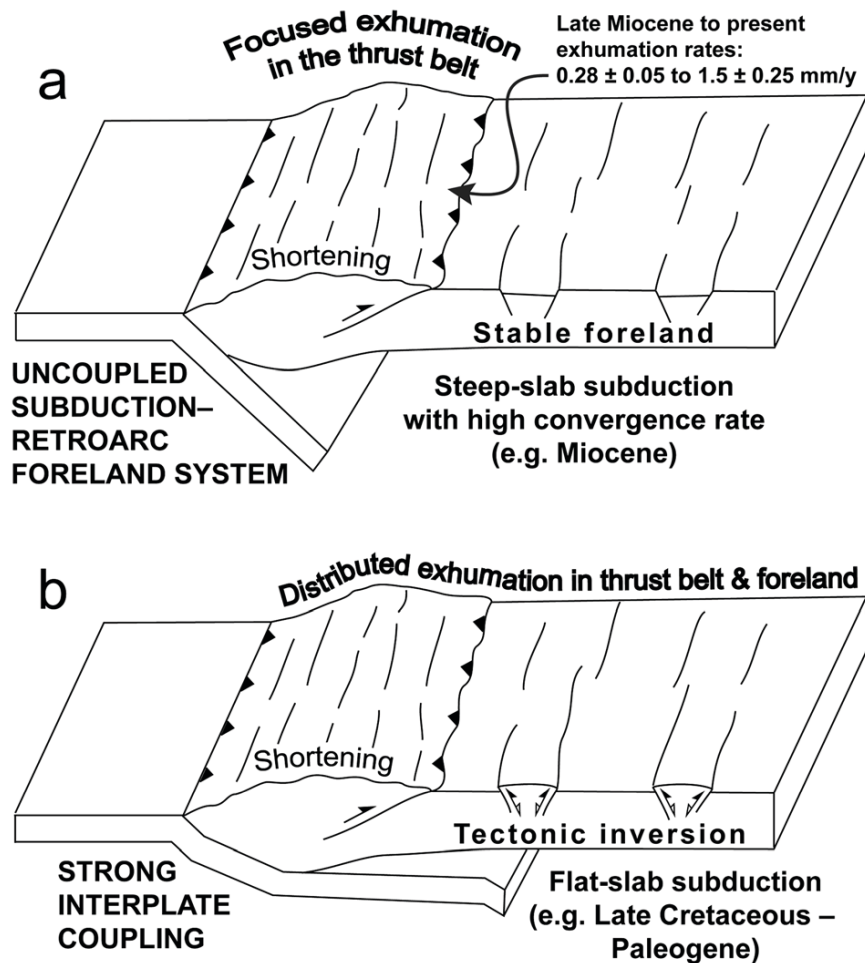
Figure 3.9 – Interpretative cartoon. (a) Uncoupling of the deformation: steep slab subduction and rollback at high convergence rate produce shortening, tectonic inversion and exhumation in the fold-thrust belt but little or no shortening in the foreland area. (b) Coupling of the deformation: flat-slab subduction produces shortening, tectonic inversion and exhumation over both the fold-thrust belt and the foreland area, leading to the development of the broken foreland.

Taking into account the relatively simple tectonic setting of the outer Patagonian Andes and the lack of major structures (e.g., low-angle extensional detachments) that could control exhumation, this process is best interpreted as a result of thrust-related rock uplift and coeval erosion (that is known to have occurred at a rate of ~1 km/Myr since the Late Miocene at 41–42°S) (Glodny et al., 2006, and references therein). Therefore, AHe ages are likely to record reverse fault activity – and related hanging wall uplift – in the study area. If this is the case, the exhumation pattern revealed by the projected cooling ages onto the cross-sections of Figure 3.3b points to a lack of systematic sequential propagation of the deformation in the frontal part of the thrust belt. This is consistent with the thick-skinned tectonic inversion style of deformation widely documented for the Patagonian Andes (e.g.,

Folguera and Ramos, 2011; Orts et al., 2012, 2015). By such style of crustal shortening, reverse faulting is controlled by the reactivation of inherited structures rather than progressively younger thrust propagation in the footwall of previously developed thrusts. Therefore, within the general framework of eastward growth of the Andean fold and thrust belt documented by the analysis of synorogenic sediments (Ramos et al., 2011; Morabito and Ramos, 2012; Orts et al., 2012; Echaurren et al., 2016), individual fault activity and related block uplift are likely to vary irregularly both in space and time. The complex interactions between local block uplift and erosion may result in an irregular unroofing pattern such as that shown in Figure 3.3a, which, however, is bracketed in time by the overall duration of a bulk regional shortening event (of Middle Miocene to Pliocene age in our instance).

Exhumation in the thrust belt sector of the study area appears to be related with an eastward migration of the magmatic arc between 15 and 11 Ma, marked by a series of satellite magmatic bodies throughout the eastern Andean side; this was accompanied by enlargement and deepening of the foreland basin, associated with the highest shortening rates recorded for this segment of the Patagonian Andes (Orts et al., 2015). More to the south, between 45° and 48°S, Guillaume et al. (2013) interpreted a Miocene-Pliocene acceleration of exhumation, also unraveled by Thomson et al. (2001), as driven by mantle flow associated with slab window opening. There, the shortening stage started at around 32 Ma and ceased at 16–14 Ma (Lagabrielle et al., 2004). During this period, close to the Chile Triple Junction, the South Chile Ridge did not enter the subduction zone and exhumation was only linked to the approach of the ridge close to the subduction zone (Lagabrielle et al., 2004). At 16–14 Ma, ridge subduction started south of 52°S and opening of a slab window marked the end of the shortening event. At the Chile Triple Junction, a slab window developed at around 5–3 Ma, inducing extensional deformation (Scalabrino et al., 2010, 2011) and probably thermal doming-linked exhumation. On the other hand, a different explanation for Pliocene exhumation recorded more to the north (around 30°S) was provided by Fosdick et al. (2015), who related exhumation to out-of-sequence thrusting produced by a change in stress regime during Pampean flat-slab subduction.

The variability of deformation along the strike of the Andes has been related to the alternation of flat and steep slab segments (e.g., Jordan et al., 1983). For the Central Andes, a large number of studies analyzed the sedimentary, magmatic, and structural evidence of

past changes in the subduction configuration (e.g., Allmendinger et al., 1997; Orts et al., 2015, and references therein). Orogeny in mid-Cretaceous times affected most of the South American margin, possibly being controlled by an acceleration of the continent motion during its westward drifting (Somoza and Zaffarana, 2008). However, recently, Gianni et al. (2015b), using Maloney et al. (2013) data to reconstruct the average trench normal convergence and absolute velocity of the South American plate from 140 Ma to the present, pointed out close spatial and temporal relations among deformation of the broken foreland sector, development of the Chubut Group Basin, magmatic arc migration, and a series of mid-ocean ridge collisions. All of these processes appear to have converged to enhance orogeny, as indicated by the synorogenic sedimentation described by Gianni et al. (2015b), with regional shortening being accompanied by vast – though discontinuously distributed – deformation over the whole South American plate from the Andes to the offshore area of the Atlantic passive margin (Gianni et al., 2015b).

The onset of shortening at around 100 Ma coincided with the change in absolute motion of South America related to the final breakup of western Gondwana (Ramos, 2010). In late Eocene to early Miocene, trench normal absolute velocity of the South American plate remained particularly low (Maloney et al., 2013). However, plate convergence increased again at 23 Ma (above 4 cm/y), with a peak of 6 cm/yr from ~20 to 15 Ma (Pardo-Casas and Molnar, 1987; Maloney et al., 2013). This peak velocity is coincident with the latest stages of Andean shortening, triggering exhumation in the thrust belt sector of our study area (Figure 3.3), where final cooling through the ~65°C isotherm reaches the Pliocene (Table 3.2). On the other hand, the Neogene broken foreland reactivation at 19.0–14.8 Ma (Bilmes et al., 2013) occurred in a period characterized by no general arc expansion (Gianni et al., 2015b, and references therein). This rules out the possibility of a long-standing flat-slab segment during this time span, as already pointed out by Bilmes et al. (2013) themselves. As a matter of fact, our new low-T thermochronometric data provide no evidence for major reverse-slip fault reactivation and tectonic inversion in the Gastre foreland sector at kilometric scale during the Neogene, despite the fact that the closure temperature of the apatite (U-Th)/He system makes the applied geochronological method as the most appropriate to unravel exhumation throughout the uppermost part of the crust. Therefore, Miocene tectonic inversion in the Gastre area must have been very mild and limited, and it did not produce any significant exhumation.

In synthesis, our results suggest that, during periods of steep-slab subduction and rollback, high convergence rates (above 4 cm/yr) (Maloney et al., 2013) are able to produce shortening in the fold and thrust belt, but far-field stress propagation and tectonic inversion in the foreland are relatively minor, the foreland being essentially uncoupled from the thrust belt (Figure 3.9a). On the other hand, a flat-slab configuration, probably associated with thermal weakening of the overriding plate imposed by prolonged mid-ocean ridge subduction (Martinod et al., 2005; Ramos, 2005), leads to regional shortening involving both the thrust belt and the foreland (Figure 3.9b). This is consistent with geological observations and insights from analog modeling, which suggest that the occurrence of horizontal slab segments results in stronger interplate coupling (Martinod et al., 2010). This, besides relatively high shortening rates in the orogen (Guillaume et al., 2009), also produces widespread shortening of continental plate interiors (Martinod et al., 2010). During these stages of flat-slab subduction, the foreland sector may therefore experience tectonic inversion triggering substantial exhumation. This coupling of the deformation may be effective even at very large distances (i.e., many hundreds of kilometers) from the subduction trench, as it occurred during Late Cretaceous to Paleogene times in the Patagonian Andes.

3.6 Conclusions

Our study suggests that configurations of flat-slab versus steep-slab subduction may exert an important role in controlling the coupling versus uncoupling of the deformation between the thrust belt and its foreland in the Patagonian Andes. Of course, the complexity of the structural architecture of this vast area implies that deformation is heterogeneously distributed in both space and time. Within this framework, the simple model depicted in the cartoon of Figure 3.9 is intended to represent just a general rule of thumb. As recently pointed out by Gianni et al. (2015b), throughout the Andean evolution of the Patagonian foreland, extensional basins have acted as anisotropies effectively focalizing strain during shortening. This process led to a localized tectonic inversion of foreland sectors as far as the distal broken foreland of the Atlantic offshore. These shortened sectors are separated by relatively undeformed areas. Such a heterogeneous style of upper plate deformation during Andean orogenesis had been reported previously at a continental scale for the whole South American plate (Cobbold et al., 2007). The

results of this study confirm the complexity and relevance of foreland deformation, probably beyond the simple notion of propagation of horizontal compression into the foreland area during the main stages Andean orogenesis. In particular, the spatial distribution of tectonic inversion and associated exhumation, being focused in the thrust belt or spreading over wide foreland sectors as well, appears to be controlled by deep geodynamic processes (i.e., slab rollback versus flat-slab subduction). Late Miocene to Pliocene AHe ages from the frontal part of the northern Patagonian Andes correlate well with a shortening and exhumation stage documented to have occurred in the thrust belt during steep subduction characterized by high convergence rates (>4 cm/yr). On the other hand, AHe ages obtained for the first time in this study for the broken foreland unraveled final exhumation at near-surface conditions (i.e., through the ~100–50°C HePRZ) during Late Cretaceous to Paleogene times. This is envisaged to have occurred by the upward extrusion of the sedimentary fills of Mesozoic grabens/half-grabens, accompanied by folding of the sedimentary successions caught between rigid basement blocks, and by substantial unroofing produced by erosion of the overlying uplifted sedimentary cover. This process was coeval with a major shortening stage in the thrust belt, associated with a period of flat-slab subduction. Coupling of the deformation during such a period was probably enhanced by thermal weakening of the overriding plate as a result of mid-ocean ridge subduction (Ramos, 2005), resulting in plate-scale heterogeneous shortening.

Acknowledgments

Chapter 4

This chapter is focused on the methodology applied to the sequential restoration that allows us provide the prediction of the low-T thermochronometric ages along the present-day geological cross-section and the evolution of the isotherms through time. This method is also a way to validate the proposed tectonic scenario by comparing the predicted ages resulting from the sequential restoration with the measured ones. This thermo-kinematic model is performed for 3 Profiles. In the following chapter the version of the manuscript ready to be submitted to Lithosphere is presented.

Tectonic evolution of the North Patagonian Andes and its foreland (40°– 42°S): New constraints from thermo-kinematic modeling

E. Savignano[1], M. Zattin[1], S. Mazzoli[2], R. Ketcham[3], C. Gautheron[4] and M. Franchini[5].

[1]Department of Geosciences, University of Padua, Via G. Gradenigo, 6, Padova 35131 Italy; [2]Department of Earth Sciences, University of Naples "Federico II", Largo San Marcellino 10, Napoli, 80138 Italy; [3]Jackson School of Geosciences, The University of Texas at Austin, 1 University Station C1160 Austin, TX 78712; [4]UMR Interactions et Dynamique des Environnements de Surface, CNRS-UPS 8148, Université Paris Sud, 91405 Orsay, France; [5]CONICET- Centro Patagónico de Estudios Metalogenéticos, Universidad Nacional del Comahue, Instituto de Investigación en Paleobiología y Geología, Universidad Nacional de Río Negro.

Abstract

In this paper, a new approach is applied to test a proposed scenario for the tectonic evolution of the North Patagonian fold-and-thrust belt–foreland system. Balanced geological sections were constructed across the Argentinian sector of Patagonia at latitudes of ca. 40° and 42°S, from the foreland to the frontal Andean domain. Their sequential restoration allows us to delineate the tectonic evolution and to predict the cooling history along the sections. In addition, the response of low-temperature thermochronometers (apatite fission-track and apatite (U-Th-Sm)/He) to the changes in the fold-and-thrust belt geometry produced by fault activity and topography evolution are tested. The effective integration of structural and thermochronometric methods provides, for the first time, a high-resolution thermo-kinematic model of the North Patagonian region from the Jurassic to the present day. The different modes and timing of the deformation—and related exhumation—in the thrust belt vs. foreland domain exert a discernible effect on the distribution of cooling ages along the profiles. Our analysis unravels cooling of the frontal part of the Andean thrust belt since ca. 10 Ma. The combination of thrust-related hanging-wall uplift and erosion is interpreted as the dominant exhumation mechanism for the analyzed outer portion of the orogen. Markedly older cooling ages (130-50 Ma) obtained for the foreland domain are mainly associated with localized block uplift and/or sedimentary wedge extrusion within a general framework of inversion tectonics controlled by the reverse-slip reactivation of inherited extensional faults. These results, which help unravel the response of low-temperature thermochronometers to the sequence of tectonic events and topographic changes, allow us to constrain the tectonic scenario that best honors all available data.

4.1 Introduction

Coupling balanced and restored cross-section construction with thermochronological analysis allows to produce detailed studies on deformed areas, providing the possibility to define the various stages of deformation and to quantify both their extent and timing (e.g. Castelluccio et. al., 2015; Mora et. al., 2015; Chapman et al., 2017). Such an integrated approach has been applied in this work along two transects located in North Patagonia (Argentina) at latitudes around 40° and 42°S.

Kinematic restoration of balanced cross sections is a powerful tool in structural geology, as it allows to: (i) draw a reliable picture of the changing geometry of deforming geological structures through time, (ii) determine the original position and dip of the structures, (iii) calculate the amount of shortening, (iv) define timing of basin formation and evolution, and (v) extrapolate rates of tectonic processes, such as exhumation and erosion (Bulness and McClay, 1999; Castelluccio et al., 2015; Mora et al., 2015). Starting from the first works in crustal shortening regime settings (e.g., Bally et al., 1966; Dahlstrom, 1969, 1970; Mitra and Namson, 1989), this method have been applied progressively both in extensional and inverted basin areas (Bulness and McClay, 1999 and references therein). In the oil industry, this technique is routinely used to evaluate the position of source rocks and model hydrocarbon generation, expulsion and migration, as well as to analyze structural traps in terms of timing and geometry (Buchanan, 1996). However, this method alone can be inadequate in cases where intense erosion occurred and syntectonic deposits are not continuously exposed (Almendral et al., 2014; Castelluccio et al., 2015; Mora et al., 2015). On the other hand, thermochronometric ages cannot be directly translated into time of deformation (Mora et al., 2015). Their modeling in terms of high-resolution t–T histories can help to decipher the sequence of tectonic events. However, the shift from a temperature (i.e. related to the movement of the sample through the isotherms) to a space domain (i.e. the depth of the sample during time) needs to combine kinetic and thermochronological information within a coherent model capable of taking into account variations in the distribution of isotherms in a dynamically active scenario. Another issue to take into account is the role of topographic evolution during the time and the way in which it interacts with isothermal surfaces. In fact, the wavelength of the relief, exhumation rate and heat advection strongly perturb the isotherm state (Stüwe et al., 1994; Mancktelow and Grasemann, 1997; Braun, 2002; Reiners and Brandon, 2006).

In the last few years, successful results have been obtained with FetKin (Almendral et al., 2014), a software dedicated to the forward modeling of thermochronometric ages calculated starting from kinematic restoration integrated with thermal parameters. The output is a calculation of low-temperature thermochronometric ages along a geological cross section, which can be compared with measured ages on samples collected along the profile. The comparison with measured and modeled ages allows in turn the improvement through an iterative process of the structural model.

In the last decade, the North Patagonian Andes have been the subject of an intense debate concerning the tectonics phases that, during the last 100 Ma, led to the formation of one the most classic mountain belts on Earth. Although the main deformation stages affecting the Cordillera have been defined by various studies (i.e. Mpodozis and Ramos, 1989; Charrier et al, 2007; Ramos and Folguera, 2009; Folguera and Ramos, 2011; Echaurren et al., 2016), the correlation between building of the North Patagonian Andes and the far-field response, in terms of uplift and exhumation processes affecting the foreland, has not been fully addressed. The aim of this work is to provide thermochronological constraints on the main tectonic events that occurred in North Patagonia, both in the orogenic belt and in the adjacent foreland. These are included in an integrated evolutionary model covering Meso-Cenozoic times.

4.2 Geological setting

The study area is located in the northern sector of the Southern Andes (sensu Folguera et al., 2016), a relatively young mountain belt representing the product of the magmatic and tectonic activity related to the subduction of the Pacific oceanic lithosphere beneath the South American plate (e.g. Mpodozis and Ramos, 1989; Hervè, 1994; Folguera and Ramos, 2011). This sector of the Andes, roughly placed between the Pampean flat slab zone to the north and the Chilean triple junction to the south, is characterized by lower elevations, thinner continental crust and narrower width with respect to the other segments of the chain (Hervè, 1994; Folguera et al., 2016). At these latitudes, a series of morphotectonic elements can be recognized, including, from west to east (e.g., Orts et al., 2015), (i) the Coastal Cordillera, (ii) the Chilean Central Valley, (iii) the northern Patagonian Cordillera, and (iv) the foreland (Figure 4.1).
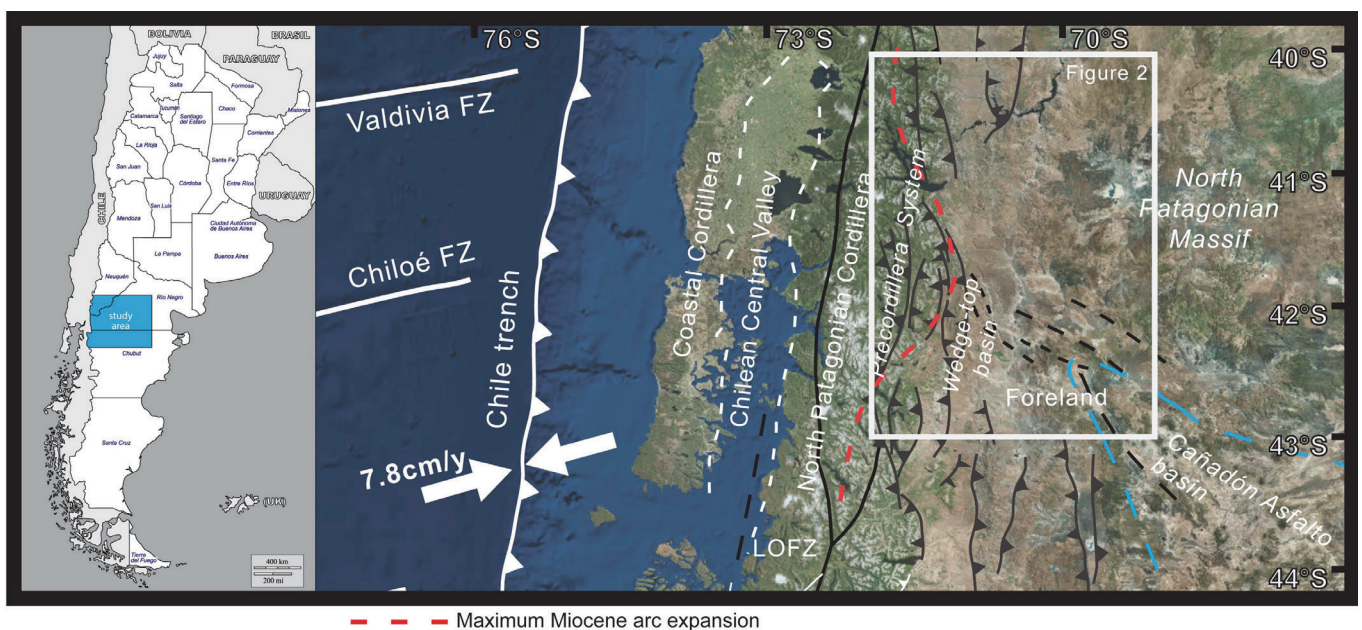
Figure 4.1 – Present tectonic setting of the North Patagonian Andes, showing major structural lineaments, morpho-tectonic units and location of Figure 4.2; LOFZ: Liquiñe-Ofqui Fault Zone. Inset shows the study area with relation to South America.

In this work, we focus our attention on the Argentinian sector located east of the Liquiñe-Ofqui Fault Zone (LOFZ), a dextral trench-linked strike-slip structure that accommodates the oblique convergence between the Nazca and South America plates and controls the emplacement of the volcanic arc, here represented by the Southern Volcanic Zone (Hervé, 1994; Cembrano et al., 1996; Rosenau et al., 2006; Ramos and Ghiglione, 2008; Vargas Easton et al., 2013).

More in detail, the northern Patagonian Cordillera between 40°S and 43°S is characterized by a mid- to high-grade metamorphic basement associated with Late Paleozoic granitoids. These rocks are overlain by marine sedimentary and volcanic successions of Jurassic age in isolated outcrops, which in turn are covered by thick successions of volcanic, volcaniclastic and marine rocks of Paleogene age. All of these rocks are intruded by the Patagonian Batholith, which at these latitudes had is main peak of activity during the Cretaceous (Ramos and Ghiglione, 2008). The deformation associated with development of the North Patagonian fold-and-thrust belt, started in the late Cretaceous (Folguera and Ramos, 2011), also propagated east, into the foreland domain. This is testified in the NE sector of the study area by uplifted Paleozoic basement blocks (constituting the North Patagonian, or Somuncura, Massif; Windhausen, 1931) with minor outcrops of Mesozoic successions, and to the SE by inverted, WNW trending (Late Triassic) to NW trending (Early Jurassic) rift systems. In this area, shortening of the Mesozoic cover produced the so-called Chubut broken foreland (Folguera and Ramos, 2011; Orts et al., 2012; Bilmes et al., 2014; Gianni et al., 2015; Echaurren et al, 2016).

4.2.1 Deformation history

The geodynamic evolution of the North Patagonian Andes started immediately after the break-up of Western Gondwana in Jurassic times (Gianni et al., 2016). Early structures controlled subsequent building of the mountain chain (Ramos and Ghiglione, 2008). The subsequent stages of the tectonic evolution of the Patagonian Andes are well preserved in this sector of the chain (Ramos, 1981; Folguera and Iannizzotto, 2004; Suárez et al., 2009; Ghiglione et al., 2013; 2016) and are summarized below.

In the Early Cretaceous to Paleocene, a switch in the tectonic regime caused the initial uplift of the North Patagonian Andes and the fragmentation of the foreland area. During

this time, an eastward magmatic arc expansion is documented in the retroarc zone, while a series of mid-ocean ridges collided one after another against the Patagonian margin.

During the Eocene to Early Miocene, a westward retraction of the magmatic arc occurred, possibly related to slab rollback. To the east, extensive intraplate magmatism began in the Patagonian foreland, partially covering the broken foreland.

During the following part of the Miocene, an acceleration of the convergence rate between the Nazca and South American plates caused renewed uplift of the Patagonian Andes and reactivation of the broken foreland system. A marked acceleration of erosion occurred at 7–5 Ma, coeval with the onset of major Patagonian glaciation and the retreat of deformation from the easternmost thrust front, as suggested by recent thermochronological data from 38° to 49°S provided by Thomson et al. (2010). These authors proposed that intense glaciation at the core of the Patagonian Andes deactivated the easternmost deformation front, leading to out-of-sequence thrusting and orogenic shrinkage during Pliocene-Pleistocene time.

4.3 Materials and methods

In this study, we integrate low-temperature thermochronometric data with structural modeling, in order to analyze and compare the tectonic evolution and exhumation in the North Patagonian fold and thrust belt and in the adjacent foreland. Two transects located around 40°S and 42°S have been selected (Figure 4.3). Along the two transects, samples have been collected and dated by using both (U-Th)/He and fission-track methods on apatite. Subsequently, three balanced and restored cross-sections have been produced— dividing the southern profile in two separate sections. Steps of the restoration have been then processed, combined with appropriate thermal parameters, to perform the thermo-kinematic model. Samples sites have been projected onto our cross section according to the formation of pertinence, implying in some cases a change in depth with respect to the actual sampling site. The southern section was separated into two profiles for several reasons: (i) the absence of thermochronometric constraints in the middle part of the section, (ii) the necessity to focus on the Neogene evolution in the fold-and-thrust belt and on the Mesozoic history in the foreland, and (iii) to simplify and accelerate model setup and calculation while omitting only a minor number of structures in the model.
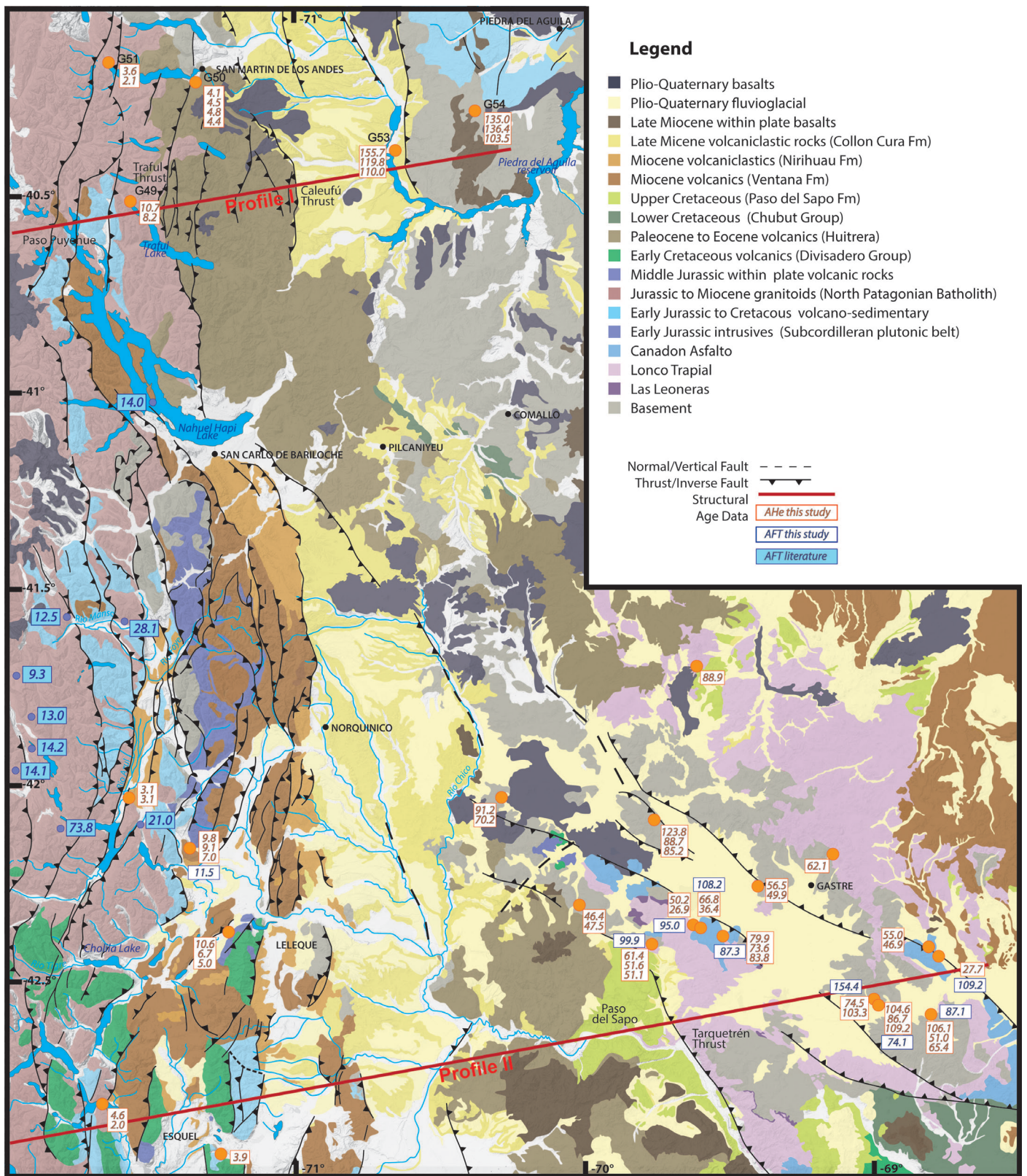
Figure 4.2 – Detailed geological map of the study area (based on Ardolino et al. (2009), Lizuaín (2009), Lizuaín and Silva Nieto (2011), Orts et al. (2012), Bilmes et al. (2013), and Orts et al. (2015) Echaurren (2016), Savignano et al. (2016) and integrated with our own field mapping). New apatite (U-Th)/He ages (samples G49, G50, G51, G53, G54; error of 10% at 1σ has to be considered for AHe ages) and published ones (Thomson, 2010; Savignano et al., 2016) are shown together with published apatite fission track (AFT) ages (from Thomson et al., 2010).

69

Sample	Latitude	Longitude	Elevation (m)	Lithology	Formation	Stratigraphic Age
G04	42°23'16"	69°31'19"	997	Granite	Mamil Choique	Lower Paleozoic to upper Paleozoic (lower Permian)
G06	42°26'40"	68°46'49"	1150	Arkose	Cañadón Asfalto	Upper Jurassic
G07	42°33'35"	69°00'14"	1070	Granite	Mamil Choique	Lower Paleozoic to upper Paleozoic (lower Permian)
G09	42°24'47"	69°46'56"	995	Arkose	Cañadón Asfalto	Upper Jurassic
G20	42°23'05"	71°14'43"	663	Granite	Leleque	Upper Jurassic
G49	40°29'07"	71°35'22"	910	Granodorite/tonalite	Los Machis	Upper Jurassic to Cretaceous
G50	40°11'44"	71°21'41"	948	Granodiorite	Complejo Colohuincul	Devonian to Carboniferous
G51	40°07'44"	71°38'40"	640	Tonalite	Los Machis	Upper Jurassic to Cretaceous
G53	40°22'06"	70°39'43"	653	Granite	Cushamen	Devonian to Carboniferous
G54	40°16'56"	70°22'49"	1009	Granodiorite	Mamil Choique	Carboniferous to Permian

Tab. 4.1 – Overview of samples.

4.3.1 Low-temperature thermochronology

A set of 5 new samples was collected from different outcrops located along the analyzed sections at 40.5°S to perform (U-Th)/He (AHe) dating, while 9 samples already dated with the same technique and presented in Savignano et al. (2016) were reprocessed to perform apatite fission track (AFT) analysis. The location of the samples is shown in Figure 4.2, while the main characteristics of the samples are summarized in Table 4.1.

(U-Th)/He (AHe) ages have been obtained using the procedure described in Savignano et al. (2016). Apatite grains were chosen with the following characteristics: a minimum width of 60 μm, absence of fractures, visible inclusions and coating. Each apatite was measured along the two axes in order to determine sphere equivalent radius, weight, and ejection factors by means of dedicated software (Gautheron and Tassan-Got, 2010; Ketcham et al., 2011; Gautheron et al., 2012). Subsequently, the replicates were placed into a Niobium basket and sent to be analyzed at the University of Paris Sud to determine He, U, Th, and Sm concentrations. Limberg Tuff and Durango apatites were used as external age standards.

Sample Name	Rs (μm)	Weight (μm)	FT	⁴He (nncc/g)	U (ppm)	Th (ppm)	¹⁴⁷Sm (ppm)	eU (ppm)	Th/U	Raw AHe age (Ma)	Corrected AHe Age (Ma)	s
G49-01	32.9	0.70	0.590	37522	35.1	55.4	143.2	48.5	1.6	6.3	10.7	0.9
G49-02	39.0	1.60	0.650	23932	22.5	58.1	133.8	36.5	2.6	5.3	8.2	0.7
G50-01	32.6	0.90	0.620	23618	73.1	8.6	245.2	75.3	0.1	2.5	4.1	0.3
G50-02	48.9	2.50	0.720	18111	43.5	6.5	144.8	45.2	0.1	3.2	4.5	0.4
G50-03	41.0	1.40	0.660	45107	106.4	31.2	283.7	114	0.3	3.2	4.8	0.4
G50-04	51.7	2.90	0.730	39855	93.5	30.2	181.1	100.8	0.3	3.2	4.4	0.4
G51-01	45.9	2.26	0.730	6474	15.2	18.7	57.6	19.7	1.2	2.7	3.6	0
G51-02	53.0	3.73	0.759	2563	9.7	12.7	36.9	12.8	1.3	1.6	2.1	0
G53-01	41.0	1.30	0.660	359909	26.8	2.4	177.2	27.4	0.1	103.4	155.7	12.5
G53-02	51.1	3.00	0.760	452404	38.2	8.6	142.1	40.3	0.2	90.5	119.8	9.6
G53-03	51.0	2.40	0.730	274011	25.8	5.1	157.2	27.1	0.2	79.9	110	8.8
G54-01	35.9	1.30	0.680	317232	25.2	6.3	213.4	26.8	0.3	92.2	135	10.8
G54-02	40.9	1.80	0.700	455912	33.3	18.6	217.5	37.9	0.6	95.4	136.4	10.9
G54-03	46.0	2.30	0.730	413900	34.8	37.8	224.8	44	1.1	75.1	103.5	8.3

Table 4.2 – Apatite (U–Th–Sm)/He analytical data. FT is the ejection correction factor and Rs is the sphere equivalent radius of hexagonal crystal with the same Surface/Volume ratio, which are both determined by a using dedicated code (Gautheron and Tassan-Got, 2010; Ketcham et al., 2011; Gautheron et al., 2012). AHe ages are corrected for the F_T factor and an error at 1 σ is considered.

Apatite fission-track (AFT) analysis was performed at the FT laboratory of the University of Padua. A CN5 glass was used to monitor neutron fluence during irradiation at the Oregon State University Triga Reactor (Corvallis, USA). Central age calculation (Galbraith and Laslett, 1993) was performed with the TRAKKEY software (4.2 version; Dunkl, 2002, http://www.sediment.uni-goettingen.de/staff/dunkl/software/). Chi-square (χ^2) testing assessed the homogeneity of age populations: a population is considered homogeneous for $P(\chi^2)$ higher than 5%. D_{par} (i.e. the diameter of etch figures parallel to the crystallographic c-axis; Ketcham et al., 1999) of single crystals was measured and used as a kinetic parameter. For each sample, track densities were measured at least on 20 grains whereas track length measurement was carried out only if possible, as a function of the U content.

Sample name	No. of crystals	Spontaneous		Induced		$P(\chi^2)$	Dosimeter		Age (Ma) ± 1s	Mean confined track lenght (mm) ± std. err.	Std. dev.	No. of tracks measured
		r_s	N_s	r_i	N_i		r_d	N_d				
G04	20	10.86	867	24.27	1938	98.3	11.39	4798	87.3±4.3	11.95±0.23	1.87	66
G05	16	4.15	155	7.55	282	96.7	11.51	8875	108.2±11.2	-	-	-
G06	36	3.23	352	5.73	625	100.0	11.34	8875	109.2±7.8	13.75±0.25	1.29	26
G07	19	39.86	2211	51.05	2832	99.9	11.60	4798	154.4±6.0	12.47±0.23	1.30	100
G08	20	12.01	643	31.20	1670	73.5	11.22	4798	74.1±4.0	11.97±0.23	2.27	96
G09	40	5.81	602	11.11	1152	91.0	11.17	8875	99.9±5.6	12.02±0.27	2.01	56
G13	34	15.71	1475	30.93	2904	0.6	10.94	8875	95.0±4.8	11.73±0.19	1.45	61
G15	20	3.19	147	6.80	313	99.0	10.83	4798	87.1±9.0	-	-	-
G21	20	2.08	92	33.06	1464	100.0	10.60	4798	11.5±1.3	-	-	-

Table 4.3 – Apatite Fission Track Analytical Data. AFT ages were obtained using the standard external detector method and the zeta calibration approach. Ages presented in this table are central ages calculated using dosimeter glass CN5 and ζ-CN5 = 344.99±7.8 (Elisa Savignano). The zeta valuehave been obtained on Durango and Fish Canyon apatite standards (Hurford and Green 1983). r_s: spontaneous track densities (x 10^5 cm^{-2}) measured in internal mineral surfaces; N_s: total number of spontaneous tracks; ri and rd: induced and dosimeter track densities (x 10^6 cm^{-2}) on external mica detectors (g = 0.5); N_i and N_d: total numbers of tracks; $P(\chi^2)$: probability of obtaining χ^2-value for n degrees of freedom (where n = number of crystals-1); a probability >5% is indicative of an homogenous population.

4.3.2 Thermal modeling

The HeFTy software (Ketcham, 2005) was used to generate inverse thermal modeling based on AFT and AHe single-grain ages and AFT track lengths, where available (insets in Figure 4.3).

Two to three AHe replicates were used for each modeled sample. The RDAAM model of Flowers et al. (2009) was adopted for modeling the AHe data, using stopping distances from Ketcham et al. (2011). Surface temperature was assumed to be 10°C. No constraints were imposed for samples coming from the Cordillera area, as their stratigraphic and formation ages are much older than the recorded AHe ages. For samples belonging to the foreland, temperatures between 0 and 20 °C were imposed around 250 Ma, corresponding to their near-surface exposure during Lower Triassic times (marked by an unconformity followed by the deposition of the volcano-sedimentary succession of the Garamilla Fm.; Savignano et al., 2016).
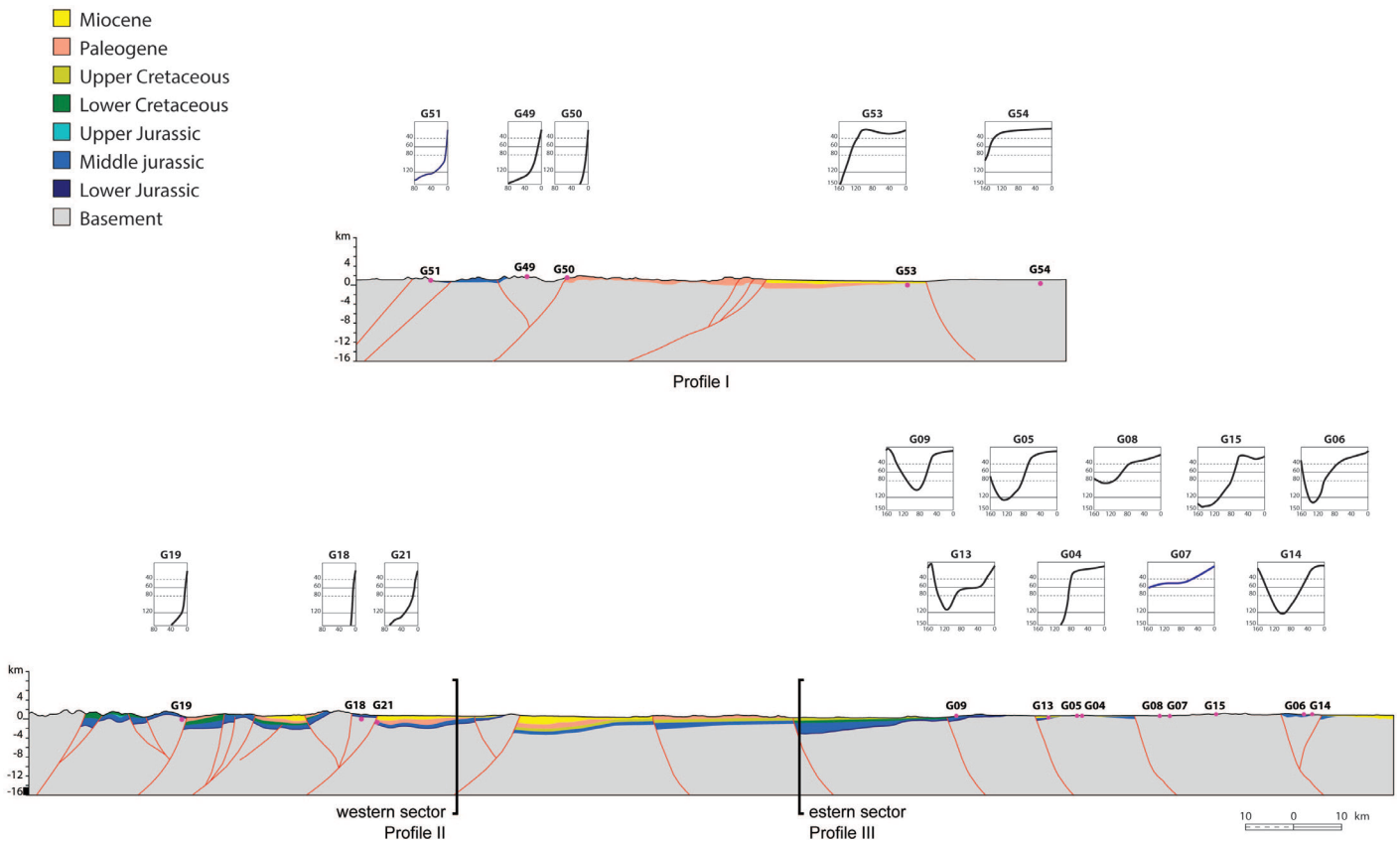
Figure 4.3 – Balanced cross sections from the Andean Cordillera axis to the foreland zone between 40°30' and 42°30'S (see Figure 4.2 for location) showing temperature-time (T-t) paths resulting from HeFTy inverse modeling weighted mean path based on AFT and AHe data; The depth represented in the model is that obtained by the finite element method with FetKin. (A) Northern cross-section from the Puyehue area to the foreland area (modified after Orts et al., 2016). (B) Southern cross-section from the Esquel area to the foreland area where Gastre Basin is located (modified after Echaurren et al., 2016); Note that this section is discussed separately for the two profiles (i.e. western and eastern).

4.3.3 Cross-section building and sequential restoration

Two WSW-ENE transects across the Patagonian Andes and their foreland were chosen parallel to the tectonic transport direction and perpendicular to the general trend of the regional structures. Balanced geological sections along the selected transects have been constructed and sequentially restored using Move, a dedicated software developed by Midland Valley Exploration Ltd. The northern transect is located at a latitude around 40°S, whereas the southern one, on which Profiles II and III lie, is roughly located at 42°S (Figure 4.2).

73

The balanced sections extend from the Argentinian side of the North Patagonian Andes across the Precordillera and the wedge-top basins, to the foreland zone. Structural data and observations were integrated with published data sets and geological maps (see details below), allowing us to constrain the surface geology and the geometry of deep structures. Flexural-slip and simple shear algorithms for restoration, coupled with 2-D forward kinematic modeling were performed to check the geometries at depth. Erosion has been applied in the model after each sequential step of restoration whenever relevant. Surface data have been extracted from 1:750000 scale geological maps of Chubut (Lizuaín, 1995) and Rio Negro (Gonzalez, 1994) and 1:250000 scale geological maps (San Martin the los Andes, Piedra del Aguila [Cucchi, 1998], Esquel [Lizuaín, 2009], Gastre [Lizuaín and Silva Nieto, 2011], and Gan Gan [Ardolino et al., 2009]; sheets published by SAGEMAR). Geological maps together with information regarding the thickness and geometry of the sedimentary successions and deep basement architecture were also obtained from the recent works of Echaurren et al. (2016) and Orts et al. (2015). This was integrated with our own fieldwork, which allowed us to increase the density of bedding readings for cross-section building, gather structural data and reinterpret some tectonic contacts (see also Savignano et al., 2016).

In the regional cross-sections, lithostratigraphic units have been grouped and simplified on the basis of their stratigraphic age. However, differentiations have been maintained where different sandstone/shale ratios occur (i.e. in the Jurassic part of the succession). Once the cross sections were constructed, flexural-slip restoration or simple shear restoration was performed on each structure. Both these algorithms preserve bed area and length. The restored sections resulting from the sequential restoration were then deformed forward in time (from the Jurassic to the present day for the foreland sector, profile III; from the Paleogene to the present-day for the thrust belt sectors, profiles I and II) in order to validate the structural interpretation and define the geometry and thickness of the eroded successions.

4.3.4 Thermo-kinematic modeling

The balanced and sequentially restored cross-sections were processed using FetKin. This is a finite element solver that takes as input a series of detailed balanced cross-sections created using dedicated software such as Move, and solves the heat flow equation along

with predicted thermochronometric ages which can be compared against measured data; it also performs an independent analysis of the cross-sections and flags aspects that are structurally out of balance (Ketcham et al., 2013). This is an iterative procedure during which several combinations of erosion rate, paleotopography, fault geometry and activity, and lithostatic load can be tested in order to reach the best fit between modeled and measured data. FetKin provides the evolution of the isotherms through time, allowing estimating the maximum temperatures experienced by the studied successions. This study follows the workflow already applied in different convergent settings such as the Eastern Cordillera of Colombia (Mora et al., 2014) and the Western Carpathians (Castelluccio et al., 2015).

The real data are projected onto the section according to the formation of pertinence. Thermal parameters and timing of the deformation were obtained from published datasets. Thermal parameters were set as follows: (i) geothermal gradient: 30°/km; (ii) thermal conductivity: 2.2 W/m·°C; (iii) density: 2.7 g/cm^3; and (iv) specific heat: 1000 kcal/kg·°C for the horizons (Nelson et al., 1982; Carrapa et al., 2008; Collo et al., 2011; Davila and Carter, 2013). Parameters that define top and bottom boundary conditions are: (i) mean sea-level temperature: 10 °C; (ii) depth of the lower boundary: 16 km below sea level (bsl); and (iii) basal temperature: 460 °C. A maximum depth for the model of 16 km was chosen as that of a major detachment level for the upper crustal faults shown in the section (Ramos et al., 2004; Orts et al. 2015) of transition to homogeneous, diffuse strain in the lower crust. The occurrence of reactivated extensional faults suggests that this mid-crustal detachment level is a reactivated inherited extensional decollement (Marshak et al., 2000; Tavani, 2012). Based on literature studies (e.g. Folguera and Ramos, 2011), inherited ages—Cretaceous and Paleogene for the foreland and the Precordillera areas, respectively—were assigned at the modeled horizons, as corresponding to the well testified major tectonic events occurred in the area, so that the differences between fully reset and inherited ages could be clearly visualized.

Different time steps were chosen for the three geological sections on the basis of the most important tectonic events that affected the thrust belt and the foreland domains. For each section, FetKin was used to perform the forward modeling of the thermochronometric ages (both AFT and AHe; annealing kinetics from Ketcham et al. [2007] and Flowers et al. [2009], respectively) in each point of the present-day topographic profile.

4.4 Results and discussion

4.4.1 Profile I

This profile (Figure 4.3A), located at ca. 40°30' and oriented WSW-ENE (see Figure 4.2 for location), runs from Paso Puyehue, north of the Nahuel Huapi Lake, to the hydric reservoir of Piedra del Aguila and includes all the various morpho-structural domains of the area, from the main axial part of the orogen to the "broken foreland". The general structural architecture of the area is characterized by high-angle reverse faults producing long-wavelength anticlines (Orts et al., 2015). The westernmost part of the section includes Jurassic-Cretaceous volcano-sedimentary successions (Pilquitron Fm. and equivalents) and Cretaceous to Cenozoic granitoids of the Patagonian batholith, locally intruding the Paleozoic basement. Moving to the east, the Traful Thrust superposes the Paleozoic-Mesozoic series over Paleocene-Eocene volcanic rocks of the Huitrera Fm. This latter belongs to the Pilcaniyeu magmatic belt, which covers a large portion of the central part of the profile. This central sector is bounded to the east by an emergent deformation front, the Caleufú Thrust, associated with a narrow synorogenic accumulation of the Collón Curá basin. The easternmost portion of the section exposes again the Paleozoic basement, here constituted by the Mamil Choique Fm., and isolated Miocene within-plate basaltic flows. Five new samples (from west to east: G51, G49, G50, G53, G54) were collected along this section to perform thermochronometric analyses. Three AHe ages and two AFT ages from the literature (Thomson, 2010) were also used and constrain the minimum burial depth for the basement. Thermochronometric ages in this sector can be divided clearly into two groups (Table 4.2). A first group of younger AHe ages—characterizing samples gathered in the western part of the area—range between 2.1±0.0 and 10.7±0.7 Ma, with a broad distribution of effective uranium content (eU: 12.8 to 114 ppm) and no evident correlation between age versus eU or equivalent spherical radius. Coherently with these results, published AFT data in this area also record Miocene cooling ages. Differently, eastern samples from basement rocks record older AHe ages, ranging from 103.5±8.3 to 136.4±10.9 Ma. Slight age dispersions for these samples may be inferred to be related with a long-term exhumation experienced during their thermal history (see inset of Figure 4.3A for thermal modeling).
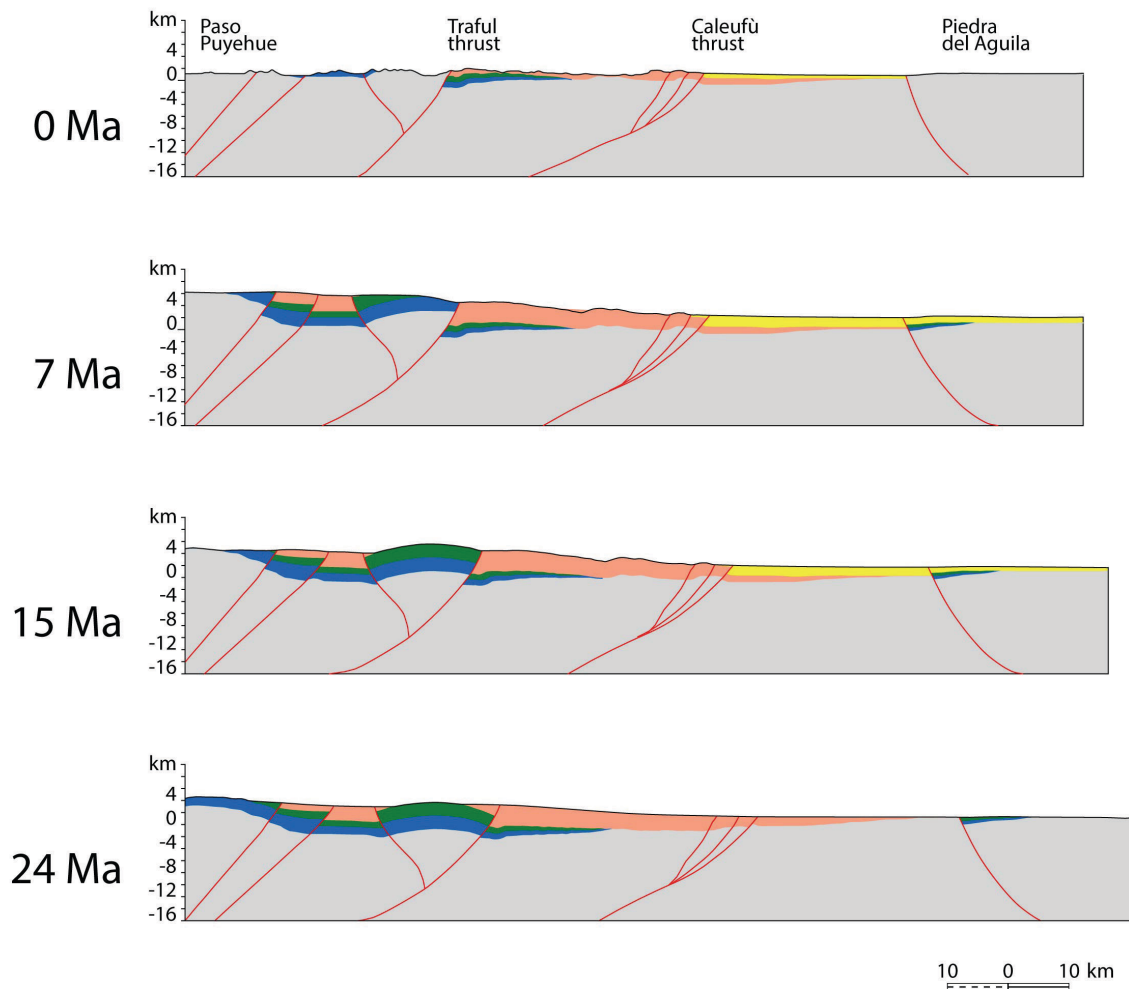
Figure 4.4 – Two-dimensional (2-D) sequential restoration of the northern profile (located at 40°30′ S from present-day to 23 Ma (A to D), performed using Move software, developed by Midland Valley Ltd. Simple shear and fault-parallel flow algorithms were used to restore the normal faults and the reverse faults, respectively. The flexural slip algorithm was applied to simulate the flexure of the lower plate. For unit colors see legend in Figure 4.3.

Thus, two marked unroofing patterns are recorded at these latitudes: Miocene exhumation involving the western part, probably controlled by the Traful Thrust, while east of this structure an Early Cretaceous event is recorded. Figure 4.4 shows the sequential restoration from the beginning of the Miocene to the present-day configuration. Faults movement in the western part of the section is mainly controlled by a major reverse fault (the Traful Thrust) and occurred during the Miocene Andean shortening stage. The role of this major fault is also clearly marked by a sharp break displayed by both measured and modeled ages across it (Figure 4.5).
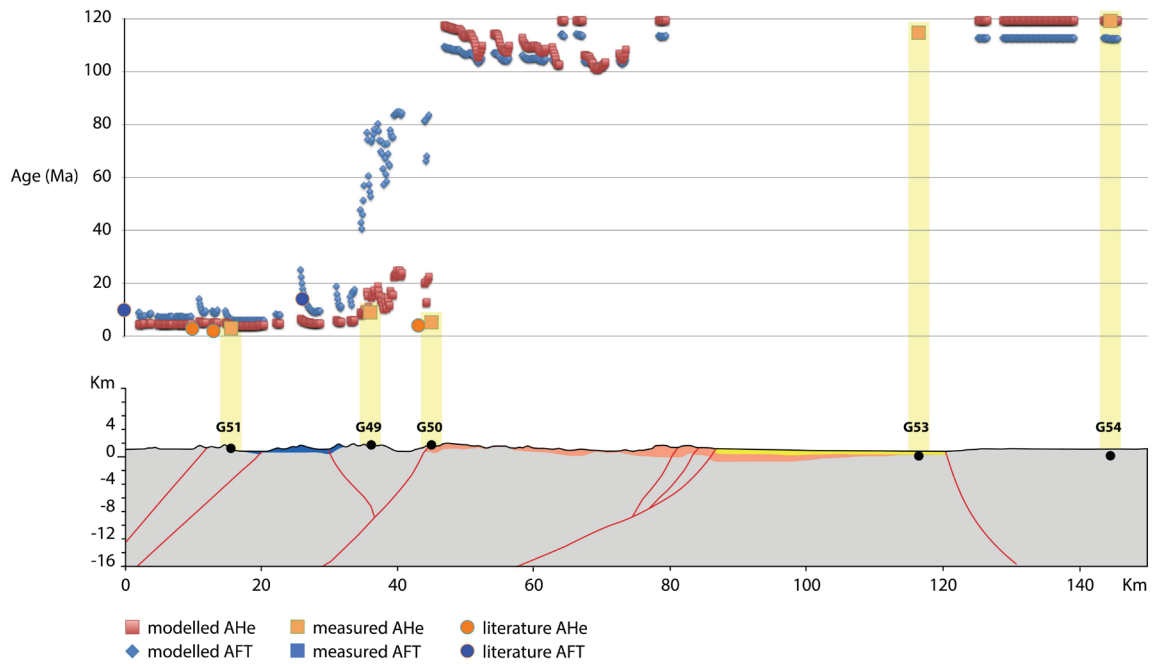
Figure 4.5 – Comparison between apatite U-Th/He (AHe) and apatite fission-track (AFT) thermochronometric ages resulting by FetKin forward model according to our structural scenario and measured AHe and AFT ages obtained in this study and taken from Thomson et al. (2010) and Savignano et al. (2016) along profile I.

Minor structures more to the east do not record substantial movements during the Neogene. Although no thermochronometric ages are available for the central part of this section, outcropping rocks, reconstructed stratigraphy (Orts et al., 2015) and our thermo-kinematic modeling all suggest that Paleogene–Miocene volcano-sedimentary products covering this area did not provide a sufficient thickness and/or thermal perturbation able to reset AHe ages (see modeled ages in Figure 4.5) and thus preserve ages related to the main Cretaceous Andean pulse in basement rocks in the easternmost part of the section (Table 4.2, Figure 4.5).

4.4.2 Profile II

Profile II (Figure 4.3B) is located at the latitude of the town of Esquel (c. 42°30′S); it encompasses the eastern slope of the Main Cordillera, the Precordillera and the western part of the wedge-top basin area (refer to Figure 4.2 for location). The profile is oriented WSW-ENE, normal to the main structural lineaments. The western part of the section is characterized by large outcrops of Paleozoic igneous-metamorphic basement, intruded by Mesozoic to Miocene magmatic bodies (Subcordilleran Batholith, Central Patagonian Batholith and North Patagonian Batholith), and by isolated Mesozoic volcanic successions (Lago la Plata Fm., Divisadero Fm.). Moving to the east, Oligocene to early Miocene tholeiitic volcanic products (Ventana Fms.) form the elongated "El Maiten magmatic belt"; associated with east-verging structures, topographic depressions preserve in their frontal part the record of the synorogenic Miocene sedimentation of the Ñirihuau (and akin Norquinico) and Collón Curá Fms. (Orts et al., 2012). Nine AHe ages (from Savignano et al., 2016, and Thomson, 2010), and two AFT ages from Thomson (2010) and a new age from sample G20 were projected onto the section and used to constrain the timing of exhumation of the geological units. AHe ages in this sector range between 2.0±0.2 and 10.6±0.1 Ma, while AFT ages range between 3.1±1.0 and 69.81±4.2 Ma, pointing to a general exhumation during the last 10 Ma for the whole area. This exhumation occurred at relatively fast rates, as is fairly clear looking at the thermal history inversion results plotted in Figure 4.3B. Exhumation rates extracted from these thermal histories, assuming geothermal grandient of c. 30°C/km (Nelson et al., 1982; Carrapa et al., 2008; Collo et al., 2011; Davila and Carter, 2013), range between 0.3 and 1.5 km/y. As for the profile discussed previously, Figure 4.6 shows the sequential restoration for the period spanning from the beginning of the Miocene to the present-day configuration. Inner (i.e. westernmost) thrusts are linked to the inversion of Early Jurassic syn-extensional wedges that occurred during the main Andean phase (Cretaceous pulse). At these latitudes, Lower Cretaceous rocks of the Divisadero Group are widely present in the Cordillera and Precordillera morpho-tectonic sectors, at variance with the northern area (Figure 4.2; Orts et al., 2012). The wedge-top area in the eastern part of the profile is characterized by condensed Jurassic-Cretaceous successions, while a thick succession of synorogenic strata is deposited in a broad flat zone next to the adjacent Precordilleran eastern slope (Giacosa et al., 2005).

Figure 4.6 – Two-dimensional (2-D) sequential restoration of the south-western profile (located at 42°30′ S from present-day to 23 Ma (A to D), performed using Move package, developed by Midland Valley Ltd. Simple shear and fault-parallel flow algorithms were used to restore the normal faults and the reverse faults, respectively. The flexural slip algorithm was applied to simulate the flexure of the lower plate. Refer to the legend of Figure 4.3 For unit colours.

Figure 4.7 – Comparison between apatite U-Th/He (AHe) and apatite fission-track (AFT) thermochronometric ages resulting by FetKin forward model according to our structural scenario and measured AHe and AFT ages obtained in this study and taken from works of Thomson et al. (2010) and Savignano et al. (2016) along profile II.

The structural model (Figure 4.6), supported by thermal modeling of the basement samples (insets in Figure 4.3), suggests exhumation in this sector was driven by a shortening and mountain building phase, accompanied and followed by intense erosion during Late Miocene-Pliocene times, leading to the exposure of the uplifted basement rocks and the strong lowering of the altitudes reached during the Miocene stage of mountain building.

4.4.3 Profile III

Profile III (Figure 4.3B) represents the continuation toward the foreland of Profile II (Figures 4.2 and 4.3B). From the Paso del Sapo area, where continental to transitional sedimentary rocks of Campanian age crop out, moving to the east and crossing the Taquetren Thrust, this section crosses the southern edge of the Neogene to Quaternary Gastre Basin (Bilmes et al., 2014, and references therein). This is characterized by the prevalent exposure of

81

basement rocks and isolated Jurassic strata belonging to the Middle-Upper Jurassic Cañadon Asfalto Fm. (Stipanicic et al., 1968). The present-day architecture of this sector is controlled by Mesozoic, high-angle, rift-related normal faults offsetting the Paleozoic Basement.
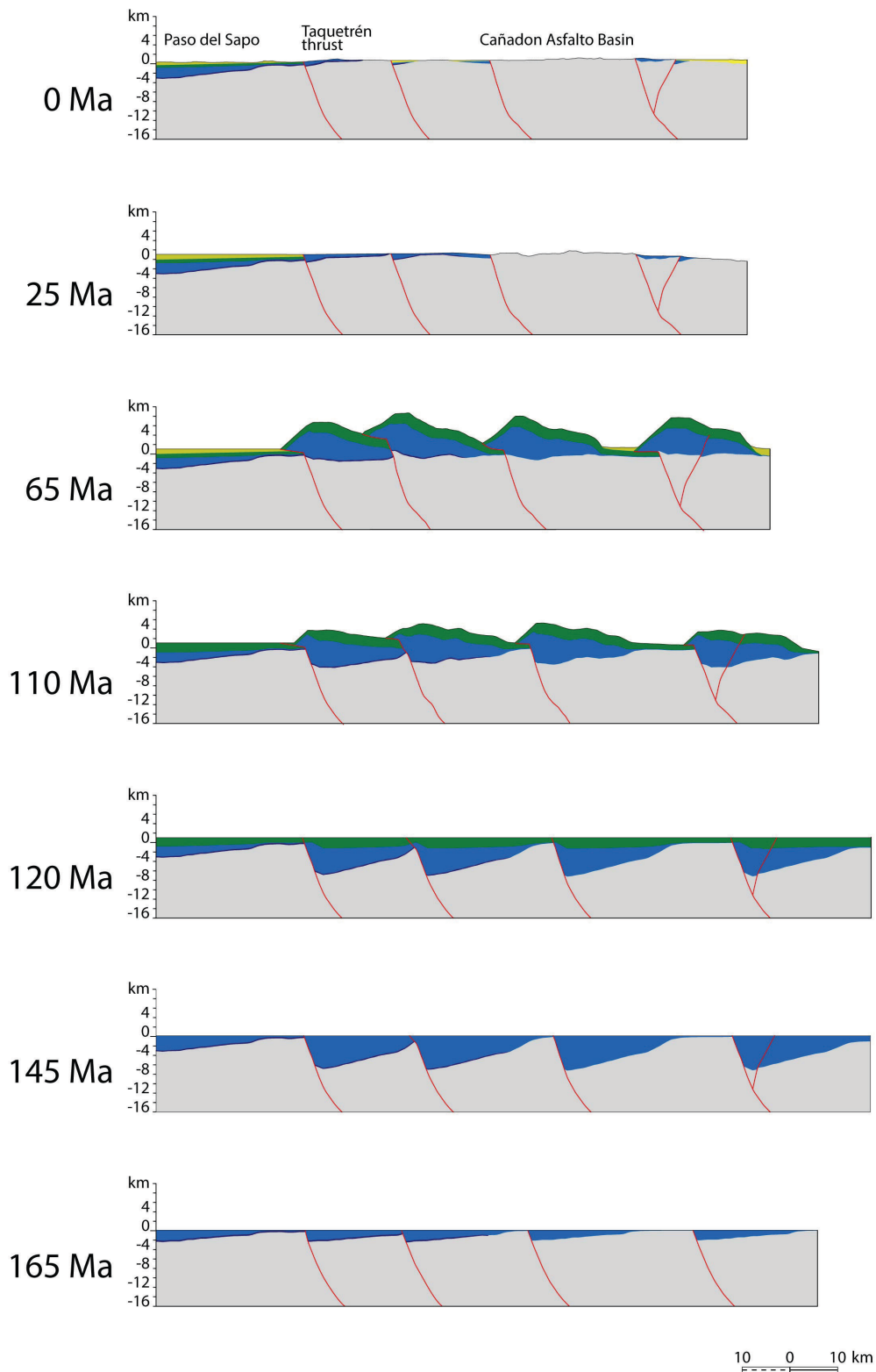
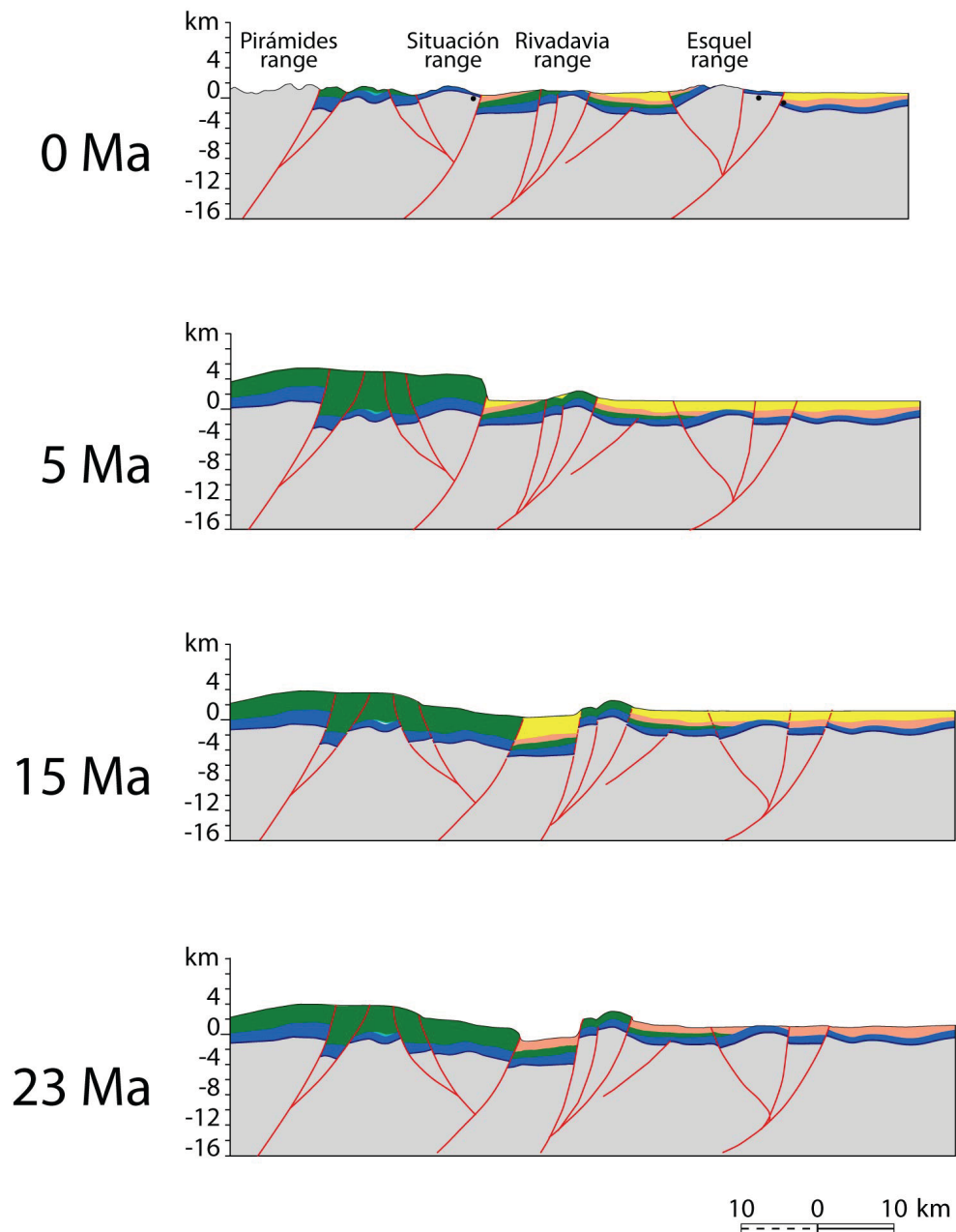Figure 4.8 (previous page) – Two-dimensional (2-D) sequential restoration of the south-eastern profile (located at 42°30' S from present-day to 165 Ma (A to G), performed using Move package, developed by Midland Valley Ltd. Simple shear and fault-parallel flow algorithms were used to restore the normal faults and the reverse faults, respectively. The flexural slip algorithm was applied to simulate the flexure of the lower plate. Erosion starting after complete basin inversion is assumed for simplicity. Refer to the legend ofFigure 4.3 for unit colours.

Data from nine samples lying along this section (Savignano et al., 2016) were used to model this transect and to constrain its Meso-Cenozic uplift history. The sampled units belong both to basement rocks cropping out in uplifted fault blocks bounding the Gastre Basin and to the Mesozoic syn-rift infill, i.e. the Cañadón Asfalto Fm.
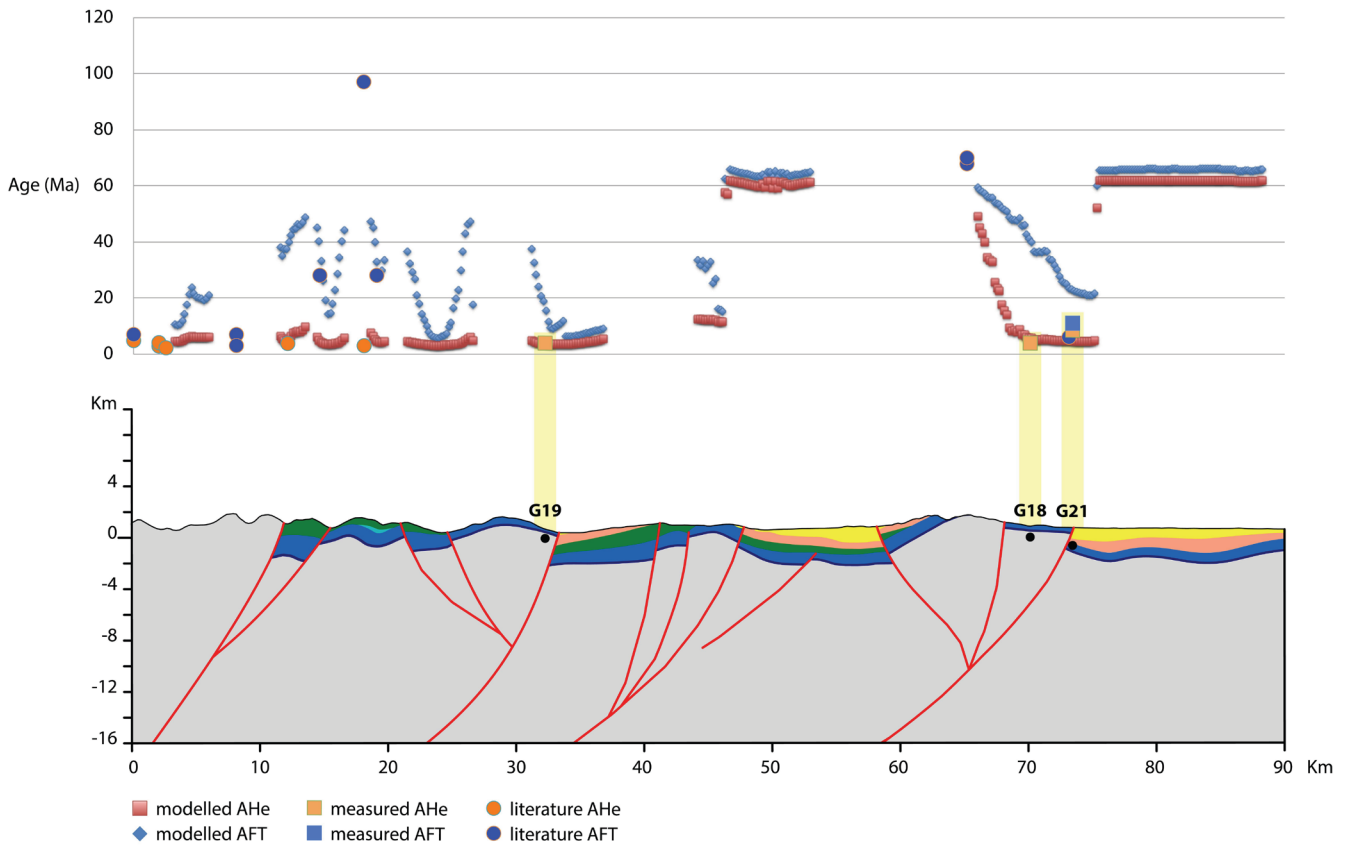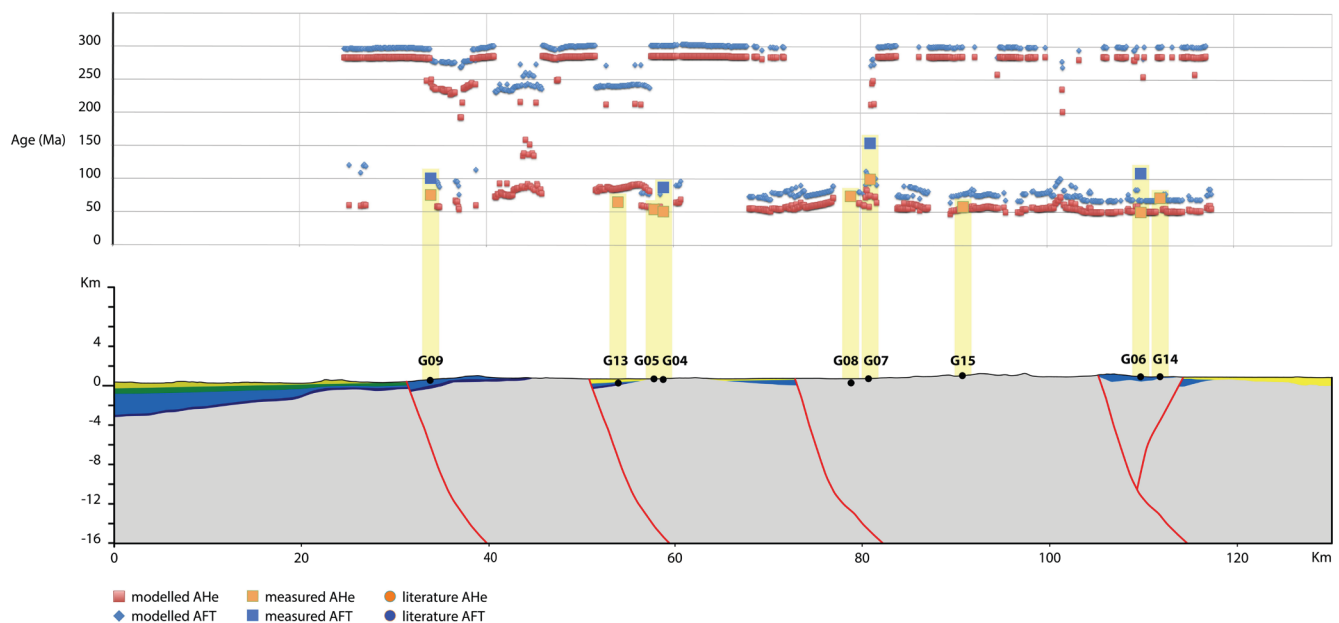

Figure 4.9 – Comparison between apatite U-Th/He (AHe) and apatite fission-track (AFT) thermochronometric ages resulting by FetKin forward model according to our structural scenario and measured AHe and AFT ages obtained in this study and taken from works of Thomson et al. (2010) and Savignano et al. (2016) along profile III.

The AHe cooling ages obtained for these samples, representing the first LT-thermochronological data published for the retroarc zone of the North Patagonian Andes (Savignano et al., 2016), range between 36.4 and 109.2. In all cases, cooling ages are younger than stratigraphic age. The broad dispersion in cooling ages reveal a prolonged stay in the HePRZ since the late Early Cretaceous, with a final exhumation phase during the Paleogene (Savignano et al., 2016). In this study, new AFT data were produced for the same samples (Table 4.3). AFT cooling ages range from the Late Jurassic to the Late

Cretaceous (74.1±4.0 to 154.4±6.0 Ma). A significant number of track lengths have been measured in all these samples (mean lengths range between 11.73±1.45 to 13.75±1.29 µm). Insets in Figure 4.3B show the results of thermal modeling for all these samples (constrained by both AHe and AFT data whenever available). All T-t paths show thermal histories characterized by a long residence (tens of Myr) in both HePRZ and AFT PAZ, followed by slow exhumation since ~120 Ma and no evidence of more recent, substantial reheating. This information was used to constrain the restored sections shown in Figure 4.8. The present-day deep architecture of the basement is dominated by half-grabens bounded by ENE dipping Mesozoic normal faults. The depth and general structure of the basement in this area is constrained by recent works of Bilmes et al. (2013), Orts et al. (2015), and Echaurren et al. (2015), which integrate seismic interpretation and well information. Asymmetric rift basins record the deposition, since the Middle Jurassic, of wedge-shaped infills here constituted by the volcano-sedimentary rocks of the Cañadon Asfalto Fm. This is related to a rifting stage that is well documented over the entire Patagonia. Subsequent shortening, acting since c. 110 Ma with a peak in the Late Cretaceous, involved these depocenters, producing inversion of preexisting extensional structures and thrusting of Lower Cretaceous successions (Barremian; Cerro Barcino Fm.). Crustal shortening continued throughout the Cretaceous. Between Late Cretaceous and Oligocene times, mountain building is essentially terminated in the western regions, and relief lowering and basement exposure result only by prolonged erosion with no substantial fault reactivation. The structural model is supported by the forward modeling of ages presented in Figure 4.9, which is characterized by the absence of ages younger than ca. 50 Ma and by a high variability of AHe and AFT ages along the whole sector, resulting from slow exhumation since the Cretaceous.

4.4.4 Meso-Cenozoic evolution in the retroarc region

The structural evolution of the retroarc region of the North Patagonian Andes was controlled by geodynamic events that occurred in the last 200 Ma. The present-day deep architecture of the basement in the studied area is dominated by grabens controlled by N-S striking conjugate faults in the western region and half-grabens bounded by ENE-dipping faults to the east. These structures are related to the Middle Jurassic rifting stage that affected the whole South American plate (Giacosa et al., 2010; Ramos, 1999; 2005). Both in the Cordillera and in the foreland, the volcano-sedimentary record of this extensional stage is preserved in the typical wedge-shaped depositional bodies (i.e. Ibáñez-Lago La Plata Fms., Cañadon Asfalto Fm; Echaurren et al. 2016). Generalized regional extension and development of basins in the continental interiors are probably related with the opening of the Atlantic Ocean (Franzese et al., 2003) and concomitant slab-roll back to the west (Ramos, 1999). Subsequent Andean shortening, that acted at these latitudes since 110 Ma with a peak at 90 Ma (Franzese et al., 2003; Somoza & Zaffarana, 2008), involved these depocenters, producing the inversion of preexisting extensional structures and the thrusting of Lower Cretaceous successions (Barremian; Cerro Barcino Fm.). Between Late Cretaceous and Eocene times, magmatic arc migrations reached the adjacent Precordillera area, forming the Pilcaniyeu volcanic belt (González Díaz, 1979; Rapela et al., 1988; Mazzoni et al., 1991; Folguera and Ramos, 2011). More to the west, the El Maitén belt represents the westward retirement of this arc in Oligocene times (Rapela et al., 1988). Coeval within-plate volcanism, mainly represented by the Somoncurà Fm, covered extensively the foreland zone (Figure 4.2). Late Oligocene to Early Miocene intraplate eruptions took place in a similar longitudinal belt to the Somuncura plateau basalts and coexisted with short-lived foreland extension (Folguera and Ramos, 2011).

During the latest Oligocene and Early Miocene, a combination of increase in relative plate convergence (Maloney et al., 2013) and a phase of slab shallowing (Echaurren et al., 2016) produced the reactivation of the fold and thrust belt in the western area (as testified by growth strata of the Ñirihuau Fm.). On the other hand, coeval Oligocene-Miocene tectonic activity appears to have been relatively weak in the foreland sector, as no major movement of fault blocks is recorded by high-sensitivity, low-temperature thermochronometers such as the AHe system. This suggests that Miocene tectonic

inversion in the foreland sector (Figures 4.3B, 4.6 and 4.9) must have been very mild and limited, and it did not lead to substantial exhumation. However, a significant episode of exhumation and creation of relief occurred in the last 7 Ma, when the Main Andes were strongly affected by glacial erosion (Thomson et al., 2002).

4.5 Conclusions

In this work, an effective integration of thermal modeling and kinematic restoration has been applied to the case study of the North Patagonian Andes and their related foreland. This study confirms that FetKin is an efficient tool for predicting thermochronometric ages (AHe and AFT) and calculating t-T paths along a sequentially restored balanced cross-section. The applied iterative workflow, based on the progressive modification of the structural model until it reaches the best fit between predicted and real thermochronological data, allows one to refine the tectonic reconstruction and produce the most suitable model for a given area. These results provide new, fundamental information on the tectonic evolution and lithosphere behavior of the South American continent.

Chapter 5

This chapter represent a synthesis of apatite (U-Th)/He data obtained in the whole studied area. The age distribution in the Argentinean part of the North Patagonia (between 40° and 44°S) is here summarized considering both the main axial part of the orogen and the adjacent foreland. This work results from the two sampling fieldworks that allow us to cover for thermochronological study a vast area (approximately 500 x 300 km) enlarging the work done in the first part of this Ph.D. The following manuscript is still in preparation.

Meso-Cenozoic exhumation history of the North Patagonian Andes constrained by low-temperature thermochronometry

E. Savignano[1], S. Mazzoli[2], M. Zattin[1], M. Franchini[3] and C. Gautheron[4].

[1]*Department of Geosciences, University of Padua, Via G. Gradenigo, 6, Padova 35131 Italy;* [2]*Department of Earth Sciences, University of Naples "Federico II", Largo San Marcellino 10, Napoli, 80138 Italy;* [3]*CONICET- Centro Patagónico de Estudios Metalogenéticos, Universidad Nacional del Comahue, Instituto de Investigación en Paleobiología y Geología, Universidad Nacional de Río Negro;* [4]*UMR Interactions et Dynamique des Environnements de Surface, CNRS-UPS 8148, Université Paris Sud, 91405 Orsay, France.*

Abstract

Apatite (U-Th)/He (AHe) thermochronology has been applied to investigate the denudation history of the Argentinian North Patagonia between 40° and 44°S. These data provide a comprehensive low-temperature thermochronologic study throughout the whole Argentinian fold-and-thrust belt–foreland system, until now well studied under this point of view only in its internal zones. This region experienced a complex Meso-Cenozoic evolution with alternating stages of flat- and steep-slab subduction, which resulted in compressive and extensional stages in the upper plate. However, as suggested by our data, other issues have to be considered as proxies to explain the uplift pattern recorded, such as convergence velocities, aseismic ridge subduction, inherited structures and partitioning along major crustal structures. We use Helium cooling ages to assess the role of the different Andean tectonic stages—and the related compressive stress transmission—at different position of the retroarc area correlating them with geodynamic settings that followed since the late Cretaceous.

5.1 Introduction

In the last two decades there has been an increasing appreciation of how deformation at convergent plate boundaries can be transferred downward and ahead of the orogen's thrust front, leading to the development of shortening-related structures in the sub-thrust region of fold-and-thrust belts and even in adjacent cratonic forelands. Understanding the factors controlling the coupling of deformation in fold-and-thrust belts–foreland basin systems is fundamental in order to unravel both their short- and long-term evolution in relation to the interaction between deep and surface processes. Low-temperature (low-T) thermochronology is one of the best methods to provide constraints on paleo-burial, exhumation, and vertical movements in the upper kilometers of the crust. Within this framework, the Patagonian Cordillera, which developed in the retro-wedge zone of the Andes, provide a unique opportunity to analyze the relationships among deep processes affecting the subducting slab, crustal deformation in the mountain belt and in the adjacent foreland, and exhumation processes. The evolution of the Patagonian Cordillera appears to have been characterized by alternating flat- and steep-slab subduction stages. These, in turn, are interpreted to have controlled several shortening and overriding plate

extension episodes (Ramos and Folguera, 2009; Folguera & Ramos, 2011; Orts et al., 2012, 2015; Echaurren et al., 2016; Savignano et al., 2016). This complex tectonic setting influenced not only the thrust belt, but also a large sector of the foreland ahead of it. According to Folguera and Ramos (2011), non-steady-state shortening and extensional processes acted in several pulses during Late Cretaceous, Late Eocene, and Late Miocene times. Deformation in the Andean retro-wedge sector varied not only in time (i.e. with major 'cycles' of mountain building and orogenic collapse), but also in space, due to the variable degree of coupling between the orogen and the adjacent foreland. The variable transmission of horizontal compressive stress away from the orogen produced heterogeneous deformation that resulted in the present day complex structural architecture of the so-called 'broken foreland' of the Patagonian region (Dávila and Astini, 2003; Folguera & Ramos, 2011; Orts et al., 2012; Bilmes et al., 2014; Gianni et al., 2015; Echaurren et al, 2016). In this work, we want to compare how the deformation is distributed in the retroarc zone in the different structural domains (slightly coincident with longitudinal sectors) and at different latitudes considering an area encompassing the entire North Patagonia and link this variation in time of deformation to the Meso-Cenozoic geodynamic framework.

5.2 Geological framework

Compared with the central segments of the Andes, the Patagonian Cordillera is a relatively narrow fold-and-thrust belt. The northern portion of this belt, known as North Patagonian Andes extends approximately from 39°00' to 44°. This orogenic system can be subdivided in a series of morphostructural domains characterized by distinctive geology and structure, which are, from west to east: the Coastal Cordillera, the Central Valley, the North Patagonian Andes, the Precordillera, the wedge top-basin area and a wide so-called "broken foreland" (Orts et al., 2015; Echaurren, 2016; Figure 5.1).
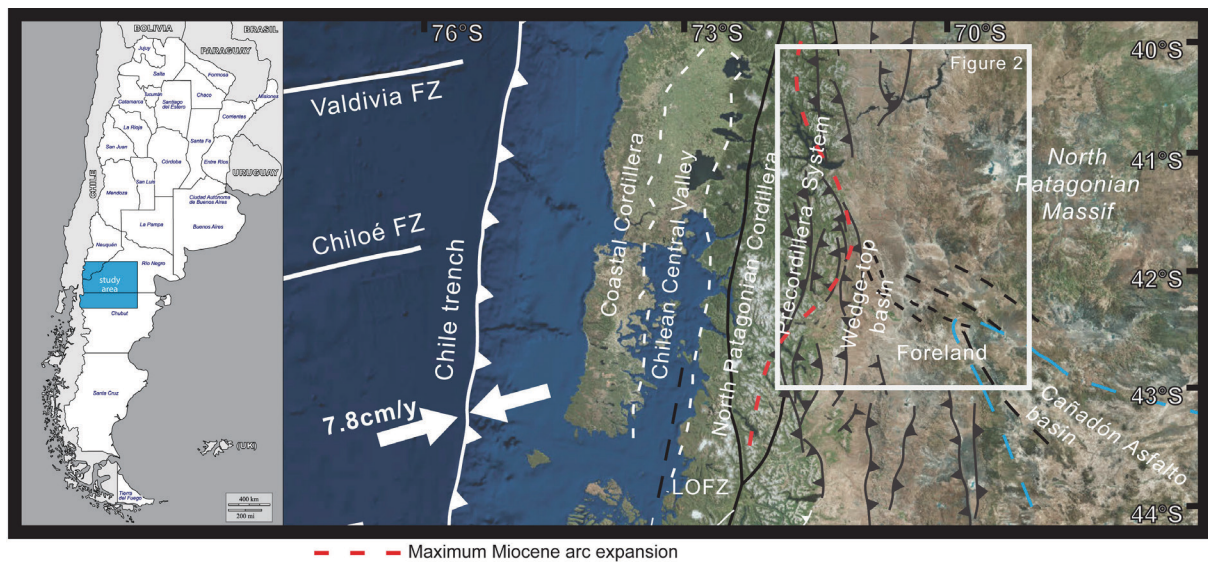
Figure 5.1 – Present tectonic setting of the North Patagonian Andes, showing major structural lineaments, morpho-tectonic units and location of Figure 4.2; LOFZ: Liquiñe-Ofqui Fault Zone. Inset shows the study area with relation to South America.

In particular in this work we focused our attention in the area going from the eastern slope of the Main Patagonian Andes to the east, in the area corresponding with the Argentina State of this latitudinal segment. The North Patagonian Andes are characterized by a mid- to high-grade metamorphic Paleozoic basement (Carboniferous to Early Permian; Basei et al., 2002) associated with Late Paleozoic granitoids (Rapela and Pankhurst, 1992). These rocks are overlain by marine sedimentary and volcanic successions of Jurassic age, preserved as isolated outcrops, which in turn are covered by thick sequences of Paleogene volcano-sedimentary rocks. The backbone of the Cordillera at these latitudes is formed by the distinctive presence of a continuous plutonic belt, the North Patagonian Batholith, predominantly Cretaceous in age in this sector (Ramos and Ghiglione 2008). The Paleozoic metamorphic basement described above continues to the east, in the adjacent North Patagonian (Somuncura) Massif (Chernicoff and Caminos, 1996) and shows age similarities with the basement outcropping in the West (Basei et al., 1999). Most of the foothills are formed by thick sequences of Paleogene volcanic and volcaniclastic rocks, with intercalated marine deposits (Bonorino, 1973) typical of a magmatic arc setting (Dalla Salda et al., 1981; Rapela et al., 1988). Marine deposits of Late Oligocene–Early Miocene age, occurring along both slopes of the Cordillera, indicate that Pacific transgressions were able to extend across the present-day mountain belt, previous to its final uplift (Ramos, 1982). East to the Precordillera, moreover, thick sequences of Miocene syntectonic strata

are preserved (Orts et al. 2015). The "broken foreland" a these latitudes is characterized by basement blocks and NW-elongated Jurassic basins related to the rifting stage affecting the entire Patagonia at the times of Atlantic opening (Bilmes et al., 2014, Echaurren et al., 2016).
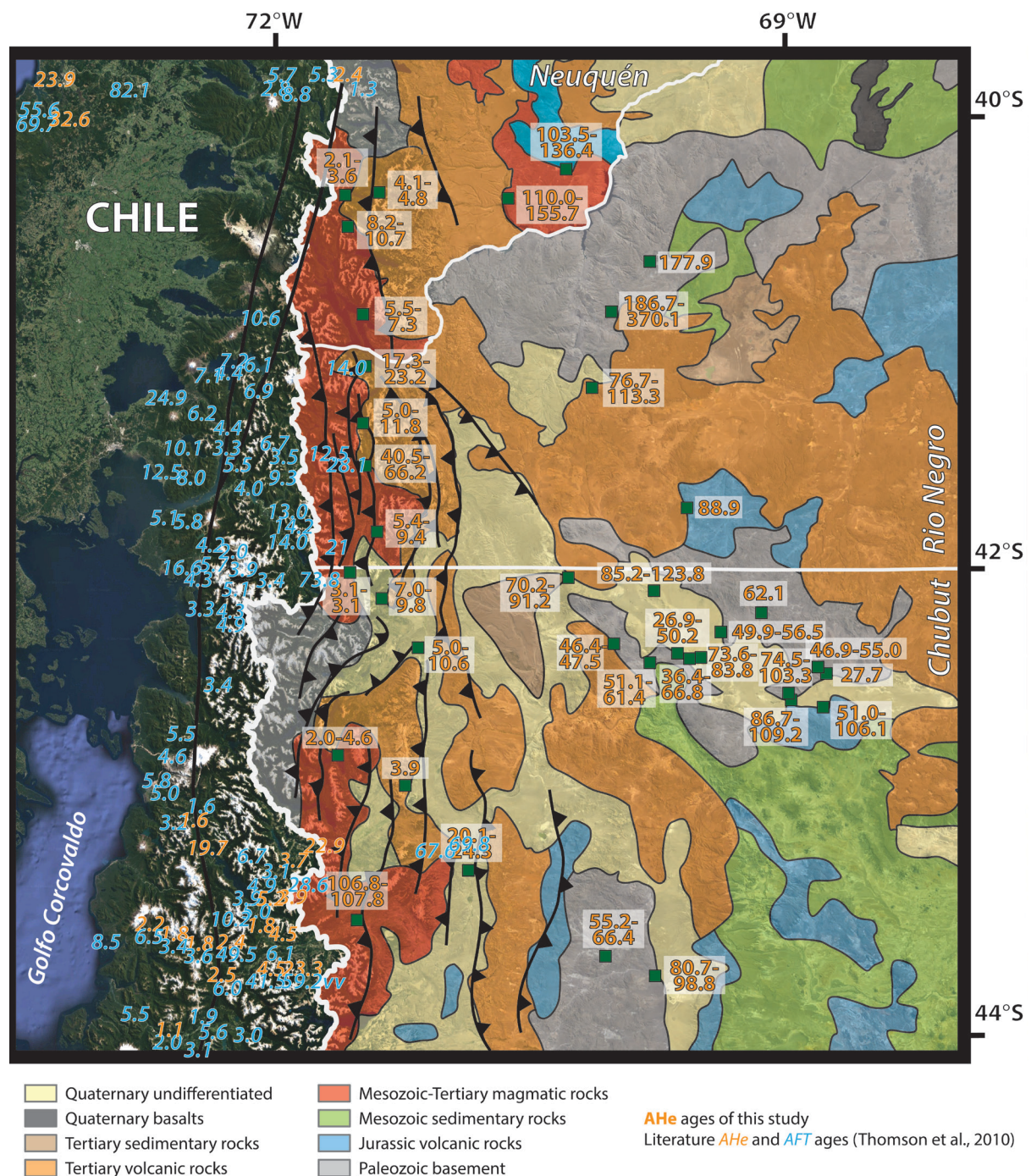
Figure 5.2 – Simplified geological map of the study area (based on Ardolino et al. (2009), Lizuaín (2009), Lizuaín and Silva Nieto (2011), Orts et al. (2012), Bilmes et al. (2013), and Orts et al. (2015) Echaurren (2016), Savignano et al. (2016). New apatite (U-Th)/He ages are shown as range of ages (error of 10% at 1σ has to be considered) and published ones (Thomson, 2010; Savignano et al., 2016) are shown together with published apatite fission track (AFT) ages (from Thomson et al., 2010).

5.3 Apatite (U-Th)/He thermochronology

AHe thermochronology is widely used to constrain the timing and rate at which rocks approach to the surface by cooling through the 40°–80°C temperature window—the partial retention zone (HePRZ) for this system (Stockli et al., 2000; Wolf et al., 1998). Being the Helium particles retained at surface temperature but diffused out of the apatites at shallow crustal temperatures, it makes this method particularly sensitive to investigate denudation processes acting in the upper 3-4 km of the crust (Ehlers and Farley, 2003; Farley, 2002; Stockli et al., 2000; Zeitler et al., 1987). In this paper, a total of 85 AHe ages are discussed, obtained from 48 samples from the Argentinian North Patagonian Andes and their retroarc area (between 40° and 44°S, Figure 5.2). The data are taken from dataset of Savignano et al. (2016) with new 17 samples analyzed for this work (Table 5.1). Samples come mainly from basement outcrops and in minor part from rift-related sedimentary successions. Apatites have been separated and manually picked at the Geosciences Department of the University of Padua and then analyzed at the University of Paris Sud (France), following the procedure described in Savignano et al. (2016).

Sample	Latitude	Longitude	Elevation (m)	Lithology	Formation	Stratigraphic Age
G30	43°44'38"	69°49'07"	670	Osta Arena	sandstone	Lower Jurassic
G31	43°39'54"	70°05'02"	825	Tepuel Group	sandstone	Carboniferous to Permian
G35	43°19'28"	70°53'46"	875	Rio Hielo	granitoid	Cretaceous
G37	43°31'30"	71°31'05"	473	Rio Hielo	granodiorite	Cretaceous
G38	41°51'03"	71°25'19"	627	Complejo Colohuincul	granodiorite	Upper Precambrian to lower Paleozoic
G39	41°33'23"	71°28'50"	731	Batolito Patagonico Cordillerano	granite	Cretaceous
G40	41°20'41"	71°30'23"	898	Complejo Colohuincul	granodiorite	Upper Precambrian to lower Paleozoic
G41	41°06'22"	71°28'59"	849	Batolito Patagonico Cordillerano	granite	Cretaceous
G43	41°02'22"	70°15'21"	904	Comallo Granodiorite	granodiorite	Carboniferous
G44	41°12'32"	70°10'00"	999	Mamil Choique	granodiorite	Ordovician
G46	40°54'06"	70°02'46"	1189	Mamil Choique	granodiorite	Ordovician
G47	40°48'09"	69°53'00"	1298	Mamil Choique	granodiorite	Ordovician
G48	40°53'37"	71°29'42"	805	Los Machis	granodiorite/tonalite	Upper Jurassic to Cretaceous
G49	40°29'07"	71°35'22"	903	Los Machis	granodiorite/tonalite	Upper Jurassic to Cretaceous
G50	40°11'44"	71°21'41"	976	Complejo Colohuincul	granodiorite	Devonian to Carboniferous
G51	40°07'44"	71°38'40"	791	Los Machis	tonalite	Upper Jurassic to Cretaceous
G53	40°22'06"	70°39'43"	645	Cushamen	granite	Devonian to Carboniferous
G54	40°16'56"	70°22'49"	986	Mamil Choique	granodiorite	Carboniferous to Permian

Table 5.1 – Samples information.

5.3.1 AHe results

New AHe ages obtained in this study are reported in Table 5.2. Considering all the samples (G30 to G54), AHe ages show a broad distribution ranging from 2.1±0.0 to 370.1±2.6 Ma. The apatites are characterized by low to quite high both Uranium content (U; 4.3 to 106.4 ppm) and effective uranium content (eU = U + 0.24 Th; 7.6 to 114.0 ppm). In all the cases these ages are younger than stratigraphic ages but among replicates some dispersion exists, especially when samples located in the foreland region are considered (longitudes minor of about 71°S). In this area, in fact, dispersion might be associated with long permanence in the HePRZ (Savignano et al., 2016). No clear correlation between age and eU or grain size has been observed. In all the cases, AHe age replicates show that all grains have undergone sufficient burial temperature to reset them fully or partially.

Table 5.2 (next page) – Apatite (U–Th–Sm)/He analytical data. FT: ejection factor; Rs: sphere equivalent radius of hexagonal crystal with the same Surface/Volume ratio (determined by using a dedicated code Gautheron and Tassan-Got, 2010; Ketcham et al., 2011; Gautheron et al., 2012). AHe ages are corrected for the FT factor and an error at 1σ is considered.

Name	Rs (μm)	Weight(μg)	FT	4He (nncc/g)	U (ppm)	Th (ppm)	Sm (ppm)	eU (ppm)	Th/U	AHe age (Ma)	AHe age c FT (Ma)	s (Ma)
G30-01	78.3	12.37	0.854	126233	4.3	39.3	75.9	13.8	9.1	73.4	85.9	0.7
G30-02	55.6	3.58	0.781	145207	5.9	48.4	209.1	17.6	8.2	63.0	80.7	0.6
G30-03	71.6	8.72	0.822	178090	5.5	50.0	107.2	17.5	9.2	81.2	98.8	0.8
G31-01	59.0	5.46	0.787	0	8.4	20.9	131.3	13.5	2.5	52.3	66.4	5.3
G31-03	43.2	2.95	0.680	0	10.5	44.7	102.0	21.3	4.3	45.2	66.4	5.3
G31-04	56.4	5.25	0.751	0	5.0	31.6	90.9	12.6	6.4	41.4	55.2	4.4
G35-01	46.7	4.23	0.722	22167	5.4	18.4	80.1	9.9	3.4	17.5	24.3	1.9
G35-02	52.4	5.64	0.750	14432	4.3	13.7	50.9	7.6	3.2	15.1	20.1	1.6
G37-01	27.8	0.54	0.562	141653	5.6	44.4	422.2	16.4	8.0	60.0	106.8	8.5
G37-02	28.3	0.67	0.597	149258	9.0	31.3	343.3	16.6	3.5	64.4	107.8	8.6
G37-03	25.7	0.34	0.561	75515								
G38-01	37.4	1.62	0.682	27338	29.6	30.9	89.5	37.1	1.0	6.0	8.8	0.7
G38-02	39.4	1.65	0.677	35968	34.5	48.5	92.1	46.2	1.4	6.4	9.4	0.8
G38-03	50.5	2.77	0.723	16316	24.5	38.6	92.8	33.9	1.6	3.9	5.4	0.4
G39-01	30.3	0.76	0.588	39981	5.6	12.1	242.0	8.7	2.1	31.6	53.7	0.3
G39-02	26.2	0.76	0.588	35918	5.9	17.2	303.1	10.2	2.9	23.8	40.5	0.2
G39-03	25	0.36	0.533	115956	15.0	30.5	601.3	22.6	2.0	35.3	66.2	0.4
G40-01	33.7	0.92	0.636	13772	21.7	58.7	55.4	35.9	2.7	3.2	5.0	0.4
G40-02	29.8	0.6	0.598	32916	23.3	61.7	95.0	38.2	2.6	7.0	11.8	0.9
G40-03	27.5	0.47	0.572		25.5	68.1	68.1	41.9	2.7			
G41-01	31.4	0.85	0.649	103534	59.8	42.8	177.4	70.2	0.7	12.0	18.5	0.1
G41-02	48.7	2.8	0.775	139480	51.8	47.3	142.7	63.2	0.9	18.0	23.2	0.2
G41-03	28.6	0.6	0.572	133871	93.7	67.8	225.6	110.1	0.7	9.9	17.3	0.1
G44-01	42.5	2.33	0.72	142506	13.3	1.7	89.7	13.8	0.1	81.5	113.3	9.1
G44-02	44.8	2.26	0.689	63247	8.8	0.9	95.1	9.1	0.1	53.1	77.1	6.2
G44-03	50.4	3.63	0.722	303657	34.7	40.8	122.6	44.6	1.2	55.4	76.7	6.1
G46-01	38.5	1.65	0.698	838056	21.6	14.9	211.2	25.2	0.7	258.3	370.1	2.6
G46-02	52	3.86	0.777	609994	23.9	9.9	155.6	26.3	0.4	183.4	236.1	1.8
G46-03	57.5	5.24	0.8	612305	28.5	19.1	102.4	33.2	0.7	149.3	186.7	1.5
G47-02	36	1.18	0.62	979987	67.8	12.7	322.9	71.0	0.2	110.3	177.9	14.2
G48-01	42.8	1.79	0.677	22054	34.1	57.0	177.1	47.8	1.7	3.7	5.5	0.4
G48-02	50.3	2.91	0.752	23517	31.3	50.9	136.4	43.5	1.6	4.4	5.8	0.5
G48-03	46.5	2.48	0.729	18720	19.4	37.5	129.8	28.4	1.9	5.3	7.3	0.6
G49-01	32.9	0.74	0.589	37522	35.1	55.4	143.2	48.5	1.6	6.3	10.7	0.9
G49-02	39	1.6	0.647	23932	22.5	58.1	133.8	36.5	2.6	5.3	8.2	0.7
G50-01	32.6	0.93	0.617	23618	73.1	8.6	245.2	75.3	0.1	2.5	4.1	0.3
G50-02	48.9	2.48	0.715	18111	43.5	6.5	144.8	45.2	0.1	3.2	4.5	0.4
G50-03	41	1.41	0.664	45107	106.4	31.2	283.7	114.0	0.3	3.2	4.8	0.4
G50-04	51.7	2.91	0.729	39855	93.5	30.2	181.1	100.8	0.3	3.2	4.4	0.4
G51-01	45.9	2.26	0.73	6474	15.2	18.7	57.6	19.7	1.2	2.7	3.6	0.0
G51-02	53	3.73	0.759	2563	9.7	12.7	36.9	12.8	1.3	1.6	2.1	0.0
G53-01	41	1.27	0.664	359909	26.8	2.4	177.2	27.4	0.1	103.4	155.7	12.5
G53-02	51.1	3.04	0.755	452404	38.2	8.6	142.1	40.3	0.2	90.5	119.8	9.6
G53-03	51	2.36	0.727	274011	25.8	5.1	157.2	27.1	0.2	79.9	110.0	8.8
G54-01	35.9	1.27	0.683	317232	25.2	6.3	213.4	26.8	0.3	92.2	135.0	10.8
G54-02	40.9	1.77	0.699	455912	33.3	18.6	217.5	37.9	0.6	95.4	136.4	10.9
G54-03	46	2.3	0.726	413900	34.8	37.8	224.8	44.0	1.1	75.1	103.5	8.3

5.4 Discussion

AHe ages considered in this study provide information related to depths in the range of ca. 2.5-3.5 km, assuming normal geothermal gradient values relevant for the study area (i.e. 20-40°C km^{-1}; Nelson et al., 1982; Carrapa et al., 2008; Davila and Carter, 2013) and well-established closure temperatures for the AHe system (Ketcham, 1999; Gautheron et al., 2009; Flowers et al., 2009; Djimbi et al., 2015). Our results indicate that two major stages of exhumation occurred in the uppermost crust—and were recorded through the passage in the HePRZ—over the study area: (i) a Late Cretaceous to Eocene one, and (ii) a Miocene-Pliocene one (Figure 5.3A). The former characterizes the foreland domain (Figure 5.3B), while the latter is recorded in the thrust belt (Figure 5.3C). Therefore, AHe cooling ages record markedly different patterns of exhumation over the thrust belt and the foreland domain (Figure 5.4).

The AHe ages obtained from the thrust belt sector of the study area, ranging from 21.0±0.0 Ma to 18.5±0.1, are consistent with the regional Neogene exhumation event described by Folguera and Ramos (2011). The integration of our AHe data with published apatite fission track ages (Thomson et al., 2010) indicates that, in the thrust belt sector of the study area, exhumation from 4.5-6.0 km depths started mainly during the Lower-Middle Miocene, and continued through the uppermost kilometers of the crust until Pliocene times (with rates ranging from 0.28 km/My to 1.5 km/My, based on our AHe ages). The recorded exhumation in the frontal part of the east-vergent orogen correlates well with the Neogene shortening event well documented for this area and possibly related to the high velocity convergence between the Pacific and South American plates (Ramos et al., 2011; Folguera and Ramos, 2011; Orts et al., 2012, 2015; Echaurren et al., 2016; Savignano et al., 2016).
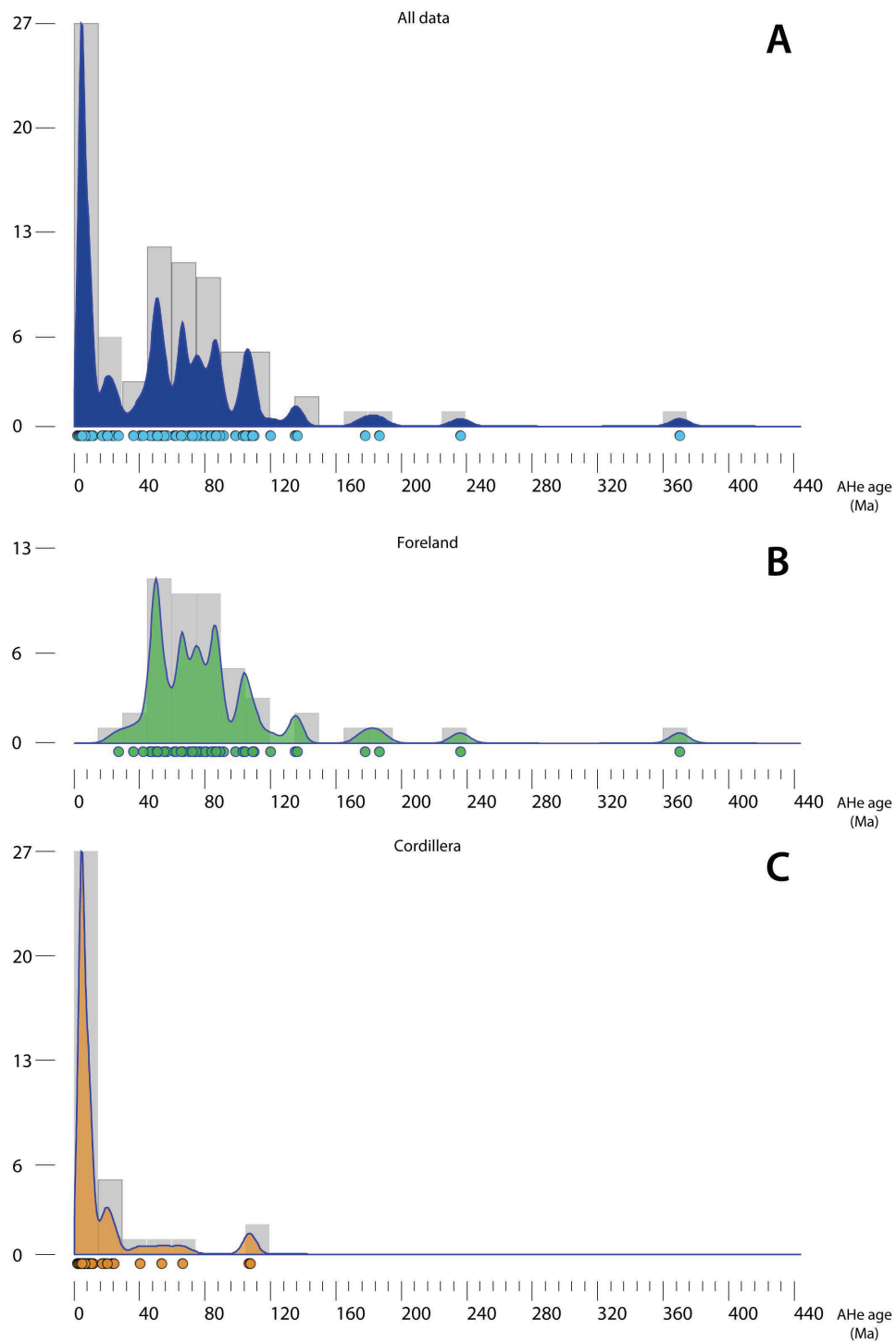
Figure 5.3 – Histogram and kernel density distribution of the apatite (U-Th)/He data set. Both were obtained with the Density Plotter software (Vermeesch, 2012) using a bin width of 15 m.y. for the histogram: (a) all data, (b) foreland data and, (c) cordillera data.

Considering the relatively simple tectonic setting of the outer Patagonian Andes, this process is best interpreted as a result of thrust-related rock uplift and coeval erosion (occurred at a rate of ~1 km/My since the Late Miocene (Glodny et al., 2008). Our data are likely to record reverse fault activity—and related hanging wall uplift—in the study area, which is characterized by a thick-skinned tectonic inversion style of deformation (e.g. Ramos et al., 2005; Folguera and Ramos, 2011).
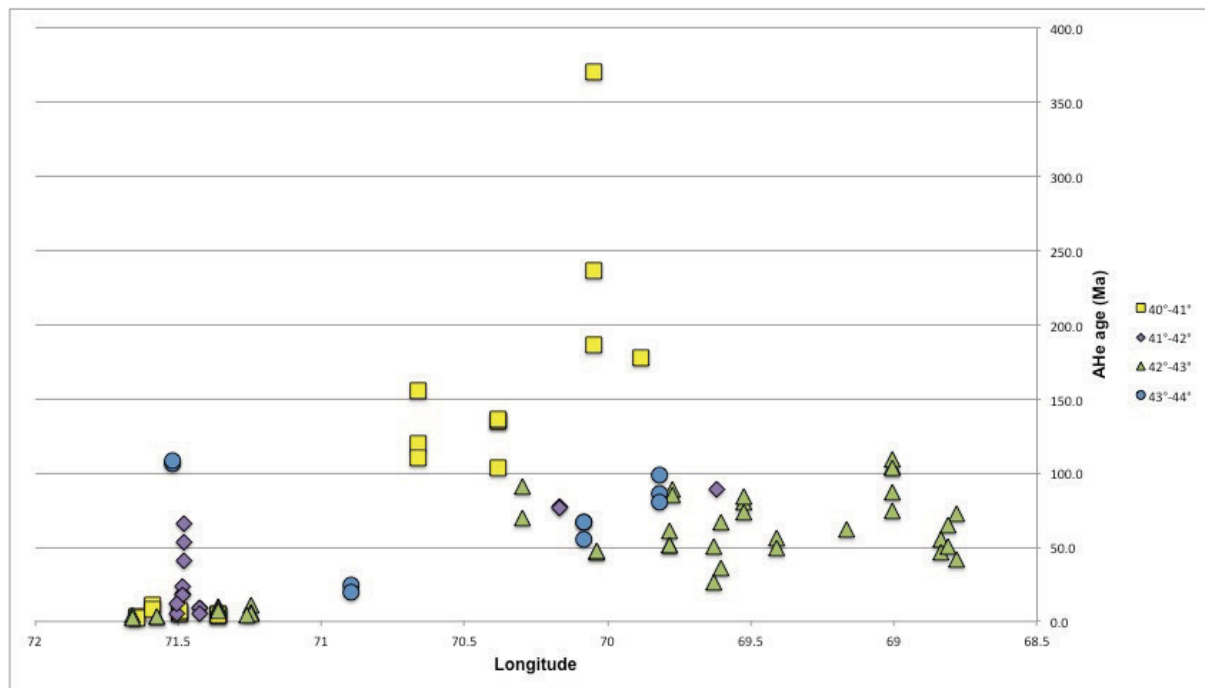

Figure 5.4 – Longitude vs AHe ages subdivided in sectors of latitudes.

 The foreland sector at the latitudes of our study area exposes Late Paleozoic to Jurassic successions that were affected by rifting during Jurassic times (e.g. Folguera and Ramos, 2011). Structural evidences of this Mesozoic event are constituted by synsedimentary normal faults and hydrothermal veins (Savignano et al., 2016). Subsequent shortening of this foreland sector has been widely documented (e.g. Bilmes et al., 2013; Gianni et al., 2015a, 2015b; Echaurren et al., 2016) and has resulted in folds affecting the succession of the Cañadón Asfalto basin (Savignano et al., 2016). Our AHe ages, being consistently younger than stratigraphic age of the sampled units (Tables 5.1 and 5.2), provide evidence for burial conditions sufficient to reset the AHe system. Indeed, the presence of a few thousands of meters of burial is consistent with tectonic stylolite formation and folding of competent units of the Cañadón Asfalto succession (Savignano et al., 2016). AHe ages obtained in this study confirm a Late Cretaceous to Eocene major tectonic inversion and

exhumation stage for this area, consistent with a regional shortening stage that has been documented for the whole Patagonian Andes and its foreland, lasted from ca. 125 to ca. 56 Ma at these latitudes (Gianni et al., 2015b). However, this event was not homogeneously distributed in the foreland zone: as shown in Figures 5.4 and 5.5A, variation in AHe age distribution in this domain can be observed. Samples located between 41° and 43°S record ages clustering between Late Cretaceous to Eocene while between 40° and 41° S older ages are recorded. This suggests that compressional tectonics acted with major effect in specific areas. Latitudes between 41° and 43°S corresponds, in fact, with the northern side of the Toarcian Chubut basin (Suarez and Marquez, 2010). This is in agreement with Gianni et al. (2015), which recently pointed out how extensional basins have acted as anisotropies, effectively focalizing strain during shortening throughout the Andean evolution of the Patagonian foreland. Relatively undeformed areas, such as the sector located in the northern part of our study area, separate these zones, where deformation can focus, reactivating inherited structures and extruding upward and folding the sedimentary infill of Mesozoic grabens/halfgrabens. This area, corresponding with the North Patagonian Massif, should have been a structural high during the Jurassic rifting stage (Scalabrino et al., 2010) and, subsequently, should have not suffered the major Andean compressional stage.

Anyway, Cretaceous-Eocene inversion has been by far the dominant shortening event in the studied foreland sector, and the role and extent of Miocene inversion (e.g. Bilmes et al., 2013) are rather subordinate, as also suggested by Gianni et al. (2015b). On the other hand, preserved Late Cretaceous to Early Paleogene AHe ages (Table 5.2 and Figures 5.2 to 5.5) and Late Cretaceous apatite fission-track ages (Thomson et al., 2010; Figure 5.2) in the Northern Patagonian Andes confirm that the regional Cretaceous-Eocene shortening stage produced exhumation over the entire thrust belt-foreland system, despite being partially obliterated by Neogene rejuvenation of thrusting and unroofing in the frontal part of the thrust belt sector. However, in this region Neogene deformation is unquestionably predominant, as recorded by our (Table 5.2) and literature thermochronometric ages (Thomson et al., 2010; Savignano et al., 2016). Even if a clustering in Miocene ages is recorded in the Cordillera, is possible to note a rejuvenating trend moving from north to south (Figure 5.5). This is in agreement with the model proposed by Cembrano et al. (2000), which recognized younger timing of activity of the

LOFZ in its southern portions, and related nature and timing of deformation, along this structural lineament, to the variation in convergence angles.
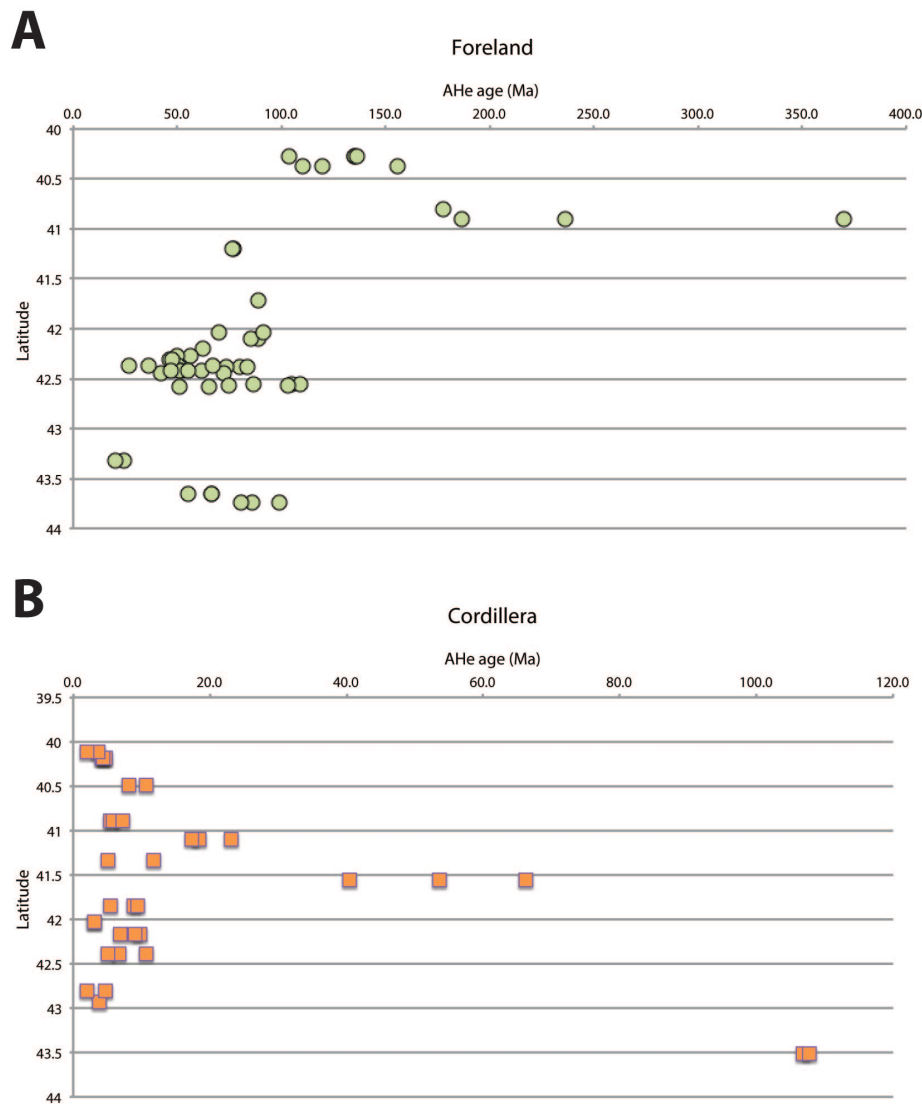
Figure 5.5 – Age vs Latitude plots of data belonging to the (A) foreland and (B) Cordillera regions. Note that the two plots are not in the same horizontal scale to highlight the age distribution recorded in the two different sectors.

The variability of deformation along the strike of the Andes has been related to the alternation of flat- and steep-slab segments (e.g. Jordan et al., 1983). Orogeny in mid-Cretaceous times affected most of the South American margin, possibly being controlled by an acceleration of the continent motion during its westward drifting (Somoza and Zaffarana, 2008). Recently, Gianni et al. (2015b), using Maloney et al. (2013) data to reconstruct the average trench normal convergence and absolute velocity of the South America plate from 140 Ma to the present, pointed out close spatial and temporal

relations among deformation of the 'broken foreland' sector, development of the Chubut Group Basin, magmatic arc migration and a series of mid ocean ridge collisions. All of these processes appear to have converged to enhance orogeny, as indicated by the synorogenic sedimentation (Gianni et al., 2015b), with regional shortening being accompanied by vast—though discontinuously distributed—deformation over the whole South America, reaching the offshore area of the Atlantic passive margin (Gianni et al., 2015b).

The onset of shortening (at ca. 100 Ma) coincided with the change in absolute motion of South America related to the final break-up of western Gondwana (Ramos, 2010). In Late Eocene to Early Miocene, trench-normal absolute velocity of the South American plate remained particularly low (Maloney et al., 2013). However, plate convergence increased again at 23 Ma (above 4 cm/yr), with a peak of 6 cm/year from ~20 to 15 Ma (Pardo-Casas and Molnar, 1987; Maloney et al., 2013). This peak velocity is coincident with the latest stages of Andean shortening, triggering exhumation in the thrust belt sector of our study area (Figures 5.3C and 5.4). On the other hand, the Neogene 'broken foreland' reactivation at 19.0–14.8 Ma (Bilmes et al., 2013) occurred in a period characterized by no general arc expansion (Gianni et al. 2015b, and references therein). As a matter of fact, our low-T thermochronometric data do not provide any evidence for major reverse-slip fault reactivation and tectonic inversion in the foreland domain during the Neogene. Thus, Miocene tectonic inversion in this sector must have been very mild and limited, and incapable to produce any significant exhumation.

Our data confirm the model proposed in the previous work (Savignano et al., 2016) that relate periods of steep-slab subduction and rollback at high convergence rates to the shortening in the fold-and-thrust belt and periods of flat-slab configuration to regional shortening involving both the thrust belt and the foreland as a consequence of a stronger interplate coupling (Martinod et al., 2010). This, besides relatively high shortening rates in the orogen (Guillaume et al., 2009), also produces widespread shortening of continental plate interiors [Martinod et al., 2010) effective even at very large distances from the subduction trench, as it occurred during Late Cretaceous to Eocene times. However, this study highlight how also other factors can introduce variations in stress propagation, that are recorded by sensible low-T thermochronometers such as AHe.

5.5 Conclusions

During the North Patagonian Andes building, the alternation of different slab configurations strongly influenced the inland migration or retreat of both the deformation front and the volcanic arc, and the uplift—and related erosion—of more or less external areas. The interplays between all of these aspects result in a complex tectonic and sedimentary foreland setting, in which inherited paleogeography of external zones exerts an important role in focus the deformation. In particular, the spatial distribution of tectonic inversion and associated exhumation in foreland area seem to depend, in the North Patagonian, on the preexistence of rift-related sedimentary basins that acted as zones of weakness at crustal-scale levels.

Chapter 6

Concluding remarks

In this work an integrated approach has been applied in the North Patagonian Andes in order to reconstruct their debated Meso—Cenozoic evolution. In particular, the Argentinian Patagonia between 40° and 44°S has been investigated. The main results have been summarized here below:

- Two main exhumation stages are recognized and recorded by low-T thermochronometers: (i) a Late Cretaceous to early Paleogene one, and (ii) a Miocene-Pliocene one. These two events are well preserved in the foreland and in the orogen, respectively;

- The broken-foreland shows thick-skin style inversion of inherited rifting-related structures. AHe and AFT ages obtained for this sector unraveled relatively slow exhumation at near-surface conditions occurred since the Late Cretaceous;

- Thermochronometric ages from the frontal part of the northern Patagonian Cordillera document, fast exhumation since the Miocene which can be related to compressive tectonics;

- Miocene compressive stage is not recorded by AHe data in the foreland and, thus, it must have been very mild and limited, without any significant exhumation;

- These two major events correlate well with configurations of flat- and steep slab suggesting that geometry of subducting plate exerts an important role in controlling the coupling vs. uncoupling of the deformation between the thrust belt and its foreland;

- Crustal heterogeneities and major structures of the upper plate, however, play an important role in the transmission of the horizontal stress from the main axis of the orogen, focusing deformation in inherited zone of weakness;

- Thermo-kinematic modeling demonstrates to be a powerful tool both in age prediction and in validating structural models even in complex structural settings.

References

Allard, J.O., Giacosa, R. and Paredes, J.M., 2011. Relaciones estratigráficas entre la Formación los Adobes (Cretácico inferior) y su sustrato Jurásico: implicancias en la evolución tectónica de la cuenca de Cañadón Asfalto, Chubut, Argentina. In XVIII Congreso Geológico Argentino, Neuquén (pp. 988-989).

Allmendinger, R.W., Cardozo, N. and Fisher, D.M., 2011. Structural geology algorithms: Vectors and tensors. Cambridge University Press.

Allmendinger, R.W., Jordan, T.E., Kay, S.M. and Isacks, B.L., 1997. The evolution of the Altiplano-Puna plateau of the Central Andes. Annual review of earth and planetary sciences, 25(1), pp.139-174.

Almendral, A., Robles, W., Parra, M., Mora, A., Ketcham, R.A. and Raghib, M., 2015. FetKin: Coupling kinematic restorations and temperature to predict thrusting, exhumation histories, and thermochronometric ages. AAPG Bulletin, 99(8), pp.1557-1573.

Angelier, J.T. and Mechler, P., 1977. Sur une methode graphique de recherche des contraintes principales egalement utilisables en tectonique et en seismologie: la methode des diedres droits. Bulletin de la Société géologique de France, 7(6), pp.1309-1318.

Angermann, D., Klotz, J. and Reigber, C., 1999. Space-geodetic estimation of the Nazca-South America Euler vector. Earth and Planetary Science Letters, 171(3), pp.329-334.

Aragón, E., D'Eramo, F., Castro, A., Pinotti, L., Brunelli, D., Rabbia, O., Rivalenti, G., Varela, R., Spakman, W., Demartis, M. and Cavarozzi, C.E., 2011. Tectono-magmatic response to major convergence changes in the North Patagonian suprasubduction system; the Paleogene subduction–transcurrent plate margin transition. Tectonophysics, 509(3), pp.218-237.

Ardolino, A. A., F. M. Salani, and A. Lizuaín (2009), Hoja 4166–III, Gan Gan. Escala 1: 250.000, Provincia del Chubut, modificado 2005: Instituto de Geología y Recursos Minerales, Servicio Geológico Minero Argentino, 1-200.

Bally, A.W., Gordy, P.L. and Stewart, G.A., 1966. Structure, seismic data, and orogenic evolution of southern Canadian Rocky Mountains. Bulletin of Canadian Petroleum Geology, 14(3), pp.337-381.

Barazangi, M. and Isacks, B.L., 1976. Spatial distribution of earthquakes and subduction of the Nazca plate beneath South America. Geology, 4(11), pp.686-692.

Basei, M.A., Brito Neves, B.B., Varela, R., Teixeira, W., Siga Jr, O., Sato, A.M. and Cingolani, C., 1999. Isotopic dating on the crystalline basement rocks of the Bariloche region, Río Negro, Argentina. In South American Symposium on Isotope Geology(No. 2, pp. 15-18).

Bechis, F. and Cristallini, E.O., 2006. Inflexiones en estructuras del sector norte de la faja plegada y corrida de Ñirihuau, provincia de Río Negro. Rev Asoc Geol Argentina, Publicación Especial, 6, pp.18-25.

Bechis, F., Encinas, A., Concheyro, A., Litvak, V.D., Aguirre-Urreta, B. and Ramos, V.A., 2014. New age constraints for the Cenozoic marine transgressions of northwestern Patagonia, Argentina (41–43 S): Paleogeographic and tectonic implications. Journal of South American Earth Sciences, 52, pp.72-93.

Bellahsen, N., Jolivet, L., Lacombe, O., Bellanger, M., Boutoux, A., Garcia, S., Mouthereau, F., Le Pourhiet, L. and Gumiaux, C., 2012. Mechanisms of margin inversion in the external Western Alps: Implications for crustal rheology. Tectonophysics, 560, pp.62-83.

Bilmes, A., 2012. Caracterización estratigráfica, sedimentológica y estructural del sistema de bajos neógenos de Gastre, provincias de Río Negro y de Chubut (Doctoral dissertation, Facultad de Ciencias Naturales y Museo).

Bilmes, A., D'Elia, L., Franzese, J.R., Veiga, G.D. and Hernandez, M., 2013. Miocene block uplift and basin formation in the Patagonian foreland: the Gastre Basin, Argentina. Tectonophysics, 601, pp.98-111.

Bohm, M., Lüth, S., Echtler, H., Asch, G., Bataille, K., Bruhn, C., Rietbrock, A. and Wigger, P., 2002. The Southern Andes between 36 and 40 S latitude: seismicity and average seismic velocities. Tectonophysics, 356(4), pp.275-289.

Bonorino, F.G., 1973. Geología del área entre San Carlos de Bariloche y Llao llao (No. 16). Fundacion Bariloche, Departamento de Recursos Naturales y Energía.

Bott, M.H.P., 1959. The mechanics of oblique slip faulting. Geological Magazine, 96(2), pp.109-117.

Braun, J., 2002. Quantifying the effect of recent relief changes on age–elevation relationships. Earth and Planetary Science Letters, 200(3), pp.331-343.

Braun, J., Van Der Beek, P. and Batt, G., 2006. Quantitative thermochronology: numerical methods for the interpretation of thermochronological data. Cambridge University Press.

Buchanan, J.G., 1996. The application of cross-section construction and validation within exploration and production: a discussion. Geological Society, London, Special Publications, 99(1), pp.41-50.

Bucher, W.H., 1939. Deformation of the earth's crust. Geological Society of America Bulletin, 50(3), pp.421-432.

Bulnes, M. and McClay, K., 1999. Benefits and limitations of different 2D algorithms used in cross-section restoration of inverted extensional faults: application to physical experiments. Tectonophysics, 312(2), pp.175-189.

Butler, R.W. and Mazzoli, S., 2006. Styles of continental contraction: A review and introduction. Geological Society of America Special Papers, 414, pp.1-10.

Carlson, W.D., Donelick, R.A. and Ketcham, R.A., 1999. Variability of apatite fission-track annealing kinetics: I. Experimental results. American mineralogist, 84(9), pp.1213-1223.

Carrapa, B. and DeCelles, P.G., 2008. Eocene exhumation and basin development in the Puna of northwestern Argentina. Tectonics, 27(1).

Carrapa, B., Hauer, J., Schoenbohm, L., Strecker, M.R., Schmitt, A.K., Villanueva, A. and Gomez, J.S., 2008. Dynamics of deformation and sedimentation in the northern Sierras Pampeanas: An integrated study of the Neogene Fiambala basin, NW Argentina. Geological Society of America Bulletin, 120(11-12), pp.1518-1543.

Carslaw, H. S. and J. C. Jeager (1986), Conduction of heat in solids (2. utg.) London, UK: Oxford University Press.

Castelluccio, A., Andreucci, B., Zattin, M., Ketcham, R.A., Jankowski, L., Mazzoli, S. and Szaniawski, R., 2015. Coupling sequential restoration of balanced cross sections and low-

temperature thermochronometry: The case study of the Western Carpathians. Lithosphere, 7(4), pp.367-378.

Castro, A., Moreno-Ventas, I., Fernández, C., Vujovich, G., Gallastegui, G., Heredia, N., Martino, R.D., Becchio, R., Corretgé, L.G., Díaz-Alvarado, J. and Such, P., 2011. Petrology and SHRIMP U–Pb zircon geochronology of Cordilleran granitoids of the Bariloche area, Argentina. Journal of South American Earth Sciences, 32(4), pp.508-530.

Cazau, L., Mancini, D., Cangini, J. and Spalletti, L., 1989. Cuenca de Ñirihuau. Cuencas Sedimentarias Argentinas, 30, p.299e318.

Cembrano, J., Hervé, F. and Lavenu, A., 1996. The Liquine Ofqui fault zone: a long-lived intra-arc fault system in southern Chile. Tectonophysics, 259(1-3), pp.55-66.

Cembrano, J., Schermer, E., Lavenu, A. and Sanhueza, A., 2000. Contrasting nature of deformation along an intra-arc shear zone, the Liquiñe–Ofqui fault zone, southern Chilean Andes. Tectonophysics, 319(2), pp.129-149.Chamberlin, R.T., 1910. The Appalachian folds of central Pennsylvania. The Journal of Geology, 18(3), pp.228-251.

Chamberlin, R.T., 1919. The building of the Colorado Rockies. The Journal of Geology, 27(4), pp.225-251.

Chapman, J.B., Carrapa, B., Ballato, P., DeCelles, P.G., Worthington, J., Oimahmadov, I., Gadoev, M. and Ketcham, R., 2017. Intracontinental subduction beneath the Pamir Mountains: Constraints from thermokinematic modeling of shortening in the Tajik fold-and-thrust belt. GSA Bulletin, 129(11-12), pp.1450-1471.

Charrier, R., Baeza, O., Elgueta, S., Flynn, J.J., Gans, P., Kay, S.M., Muñoz, N., Wyss, A.R. and Zurita, E., 2002. Evidence for Cenozoic extensional basin development and tectonic inversion south of the flat-slab segment, southern Central Andes, Chile (33–36 SL). Journal of South American Earth Sciences, 15(1), pp.117-139.

Charrier, R., Pinto, L., and Rodríguez, M.P., 2007. Tectonostratigraphic evolution of the Andean Orogen in Chile. In: Moreno, T., and Gibbons, W. (eds) The Geology of Chile. The Geological Society, London, pp. 21–114.

Chernicoff, C.J. and Caminos, R., 1996. Estructura y relaciones estratigráficas de la Formación Nahuel Niyeu, Macizo Norpatagónico oriental, Provincia de Río Negro. Revista de la Asociación Geológica Argentina, 51(3), pp.201-212.

Cloetingh, S., Beekman, F., Ziegler, P.A., van Wees, J.D. and Sokoutis, D., 2008. Post-rift compressional reactivation potential of passive margins and extensional basins. Geological Society, London, Special Publications, 306(1), pp.27-70.

Cloetingh, S.A.P.L., Ziegler, P.A., Bogaard, P.J.F., Andriessen, P.A.M., Artemieva, I.M., Bada, G., Van Balen, R.T., Beekman, F., Ben-Avraham, Z., Brun, J.P. and Bunge, H.P., 2007. TOPO-EUROPE: The geoscience of coupled deep Earth-surface processes. Global and Planetary Change, 58(1), pp.1-118.

Cobbold, P.R., Rossello, E.A., Roperch, P., Arriagada, C., Gómez, L.A. and Lima, C., 2007. Distribution, timing, and causes of Andean deformation across South America. Geological Society, London, Special Publications, 272(1), pp.321-343.

Coira, B., Nullo, F.E., Proserpio, C.A. and Ramos, V.A., 1975. Tectónica de basamento de la región occidental del Macizo Nordpatagónico (provincias de Río Negro y del Chubut). Revista de la Asociación Geológica Argentina, 30(1), pp.361-383.

Collo, G., Dávila, F.M., Nóbile, J., Astini, R.A. and Gehrels, G., 2011. Clay mineralogy and thermal history of the Neogene Vinchina Basin, central Andes of Argentina: Analysis of factors controlling the heating conditions. Tectonics, 30(4).

Continanzia, J., Manceda, R., Covellone, G.M. and Gavarrino, A.S., 2011, March. Cuencas de Rawson y Valdés: Síntesis del Conocimiento Exploratorio—Visión actual. In Kozlowski E. VIII Congreso de Exploración y Desarrollo de Hidrocarburos, Simposio Cuencas Argentinas Visión Actual (pp. 47-64).

Continanzia, J., Manceda, R., Covellone, G.M. and Gavarrino, A.S., 2011, March. Cuencas de Rawson y Valdés: Síntesis del Conocimiento Exploratorio—Visión actual. In Kozlowski E. VIII Congreso de Exploración y Desarrollo de Hidrocarburos, Simposio Cuencas Argentinas Visión Actual (pp. 47-64).

Coughlin, T.J., O'Sullivan, P.B., Kohn, B.P. and Holcombe, R.J., 1998. Apatite fission-track thermochronology of the Sierras Pampeanas, central western Argentina: Implications for the mechanism of plateau uplift in the Andes. Geology, 26(11), pp.999-1002.

Coward, M., 1994. Continental collision, in Continental deformation, edited by P. L. Hancock, pp.264-288, Pergamon, New York.

Cucchi, R., Espejo, P. y González, R. 1998. Hoja Geológica 4169-I Piedra del Águila. Subsecretaría de Minería de la Nación, Boletín 242: 74 p., Buenos Aires

Cúneo, R., Ramezani, J., Scasso, R., Pol, D., Escapa, I., Zavattieri, A.M. and Bowring, S.A., 2013. High-precision U–Pb geochronology and a new chronostratigraphy for the Cañadón Asfalto Basin, Chubut, central Patagonia: Implications for terrestrial faunal and floral evolution in Jurassic. Gondwana Research, 24(3), pp.1267-1275.

Dahlstrom, C.D., 1970. Structural geology in the eastern margin of the Canadian Rocky Mountains. Bulletin of Canadian Petroleum Geology, 18(3), pp.332-406.

Dahlstrom, C.D.A., 1969. Balanced cross sections. Canadian Journal of Earth Sciences, 6(4), pp.743-757.

Dalla, L. and Franzese, J., 1987. Las megaestructuras del macizo y Cordillera Norpatagonica, Argentina y la genesis de las cuencas volcano-sedimentarias Terciarias. Andean Geology, (31), pp.3-13.

Dávila, F.M. and Carter, A., 2013. Exhumation history of the Andean broken foreland revisited. Geology, 41(4), pp.443-446.

DeMets, C., Gordon, R.G., Argus, D.F. and Stein, S., 1990. Current plate motions. Geophysical journal international, 101(2), pp.425-478.

DeMets, C., Gordon, R.G., Argus, D.F. and Stein, S., 1994. Effect of recent revisions to the geomagnetic reversal time scale on estimates of current plate motions. Geophysical research letters, 21(20), pp.2191-2194.

Dewey, J.F. and Bird, J.M., 1970. Mountain belts and the new global tectonics. Journal of Geophysical Research, 75(14), pp.2625-2647.

Djimbi, D.M., Gautheron, C., Roques, J., Tassan-Got, L., Gerin, C. and Simoni, E., 2015. Impact of apatite chemical composition on (U-Th)/He thermochronometry: An atomistic point of view. Geochimica et Cosmochimica Acta, 167, pp.162-176.

Dodson, M.H., 1973. Closure temperature in cooling geochronological and petrological systems. Contributions to Mineralogy and Petrology, 40(3), pp.259-274.

Donelick, R.A., Donelick Raymond A, 1993. Method of fission track analysis utilizing bulk chemical etching of apatite. U.S. Patent 5,267,274.

Donelick, R.A., Ketcham, R.A. and Carlson, W.D., 1999. Variability of apatite fission-track annealing kinetics: II. Crystallographic orientation effects. American Mineralogist, 84(9), pp.1224-1234.

Donelick, R.A., O'Sullivan, P.B. and Ketcham, R.A., 2005. Apatite fission-track analysis. Reviews in Mineralogy and Geochemistry, 58(1), pp.49-94.

Duhart, P., Haller, M. and Hervé, F., 2002. Diamictitas como parte del protolito de las metamorfitas de la Formación Cushamen en Río Chico, provincias de Río Negro y Chubut, Argentina. In Congreso Geológico Argentino (No. 15, pp. 97-100).

Dunkl, I., 2002. TRACKKEY: a Windows program for calculation and graphical presentation of fission track data. Computers & Geosciences, 28(1), pp.3-12.

Echaurren, A., Folguera, A., Gianni, G., Orts, D., Tassara, A., Encinas, A., Giménez, M. and Valencia, V., 2016. Tectonic evolution of the North Patagonian Andes (41–44 S) through recognition of syntectonic strata. Tectonophysics, 677, pp.99-114.

Ehlers, T.A. and Farley, K.A., 2003. Apatite (U–Th)/He thermochronometry: methods and applications to problems in tectonic and surface processes. Earth and Planetary Science Letters, 206(1), pp.1-14.

Encinas, A., Finger, K.L., Buatois, L.A. and Peterson, D.E., 2012. Major forearc subsidence and deep-marine Miocene sedimentation in the present Coastal Cordillera and Longitudinal Depression of south-central Chile (38 30′ S–41 45′ S). Geological Society of America Bulletin, 124(7-8), pp.1262-1277.

Endignoux, L. and Mugnier, J.L., 1990. The use of a forward kinematic model in the construction of balanced cross sections. Tectonics, 9(5), pp.1249-1262.

Farley, K.A., 2000. Helium diffusion from apatite: General behavior as illustrated by Durango fluorapatite. Journal of Geophysical Research: Solid Earth, 105(B2), pp.2903-2914.

Farley, K.A., 2002. (U-Th)/He dating: Techniques, calibrations, and applications. Reviews in Mineralogy and Geochemistry, 47(1), pp.819-844.

Farley, K.A., Wolf, R.A. and Silver, L.T., 1996. The effects of long alpha-stopping distances on (U-Th)/He ages. Geochimica et cosmochimica acta, 60(21), pp.4223-4229.

Fillon, C., Gautheron, C. and van der Beek, P., 2013. Oligocene–Miocene burial and exhumation of the Southern Pyrenean foreland quantified by low-temperature thermochronology. Journal of the Geological Society, 170(1), pp.67-77.

Fitzgerald, P.G., Baldwin, S.L., Webb, L.E. and O'Sullivan, P.B., 2006. Interpretation of (U–Th)/He single grain ages from slowly cooled crustal terranes: a case study from the Transantarctic Mountains of southern Victoria Land. Chemical Geology, 225(1), pp.91-120.

Fleischer, R.L., Price, P.B. and Walker, R.M., 1965. Ion explosion spike mechanism for formation of charged-particle tracks in solids. Journal of applied Physics, 36(11), pp.3645-3652.

Fleischer, R.L., Price, P.B. and Walker, R.M., 1975. Nuclear tracks in solids: principles and applications. Univ of California Press.

Flowers, R.M., Ketcham, R.A., Shuster, D.L. and Farley, K.A., 2009. Apatite (U–Th)/He thermochronometry using a radiation damage accumulation and annealing model. Geochimica et Cosmochimica Acta, 73(8), pp.2347-2365.

Folguera, A. and Iannizzotto, N.F., 2004. The lagos La Plata and Fontana fold-and-thrust belt: long-lived orogenesis at the edge of western Patagonia. Journal of South American Earth Sciences, 16(7), pp.541-566.

Folguera, A. and Ramos, V.A., 2011. Repeated eastward shifts of arc magmatism in the Southern Andes: a revision to the long-term pattern of Andean uplift and magmatism. Journal of South American Earth Sciences, 32(4), pp.531-546.

Folguera, A., Bottesi, G., Duddy, I., Martín-González, F., Orts, D., Sagripanti, L., Vera, E.R. and Ramos, V.A., 2015. Exhumation of the Neuquén Basin in the southern Central Andes (Malargüe fold and thrust belt) from field data and low-temperature thermochronology. Journal of South American Earth Sciences, 64, pp.381-398.

Folguera, A., Naipauer, M., Sagripanti, L., Ghiglione, M.C., Orts, D.L. and Giambiagi, L., 2016. An Introduction to the Southern Andes (33–50 S): Book Structure. In Growth of the Southern Andes (pp. 1-7). Springer International Publishing.

Fosdick, J.C., Carrapa, B. and Ortíz, G., 2015. Faulting and erosion in the Argentine Precordillera during changes in subduction regime: Reconciling bedrock cooling and detrital records. Earth and Planetary Science Letters, 432, pp.73-83.

Franzese, J., Spalletti, L., Pérez, I.G. and Macdonald, D., 2003. Tectonic and paleoenvironmental evolution of Mesozoic sedimentary basins along the Andean foothills of Argentina (32–54 S). Journal of South American Earth Sciences, 16(1), pp.81-90.

Galbraith, R.F. and Laslett, G.M., 1993. Statistical models for mixed fission track ages. Nuclear tracks and radiation measurements, 21(4), pp.459-470.

Galbraith, R.F., 1981. On statistical models for fission track counts. Mathematical Geology, 13(6), pp.471-478.

Galbraith, R.F., 1988. Graphical display of estimates having differing standard errors. Technometrics, 30(3), pp.271-281.

Gautheron, C. and Tassan-Got, L., 2010. A Monte Carlo approach to diffusion applied to noble gas/helium thermochronology. Chemical Geology, 273(3), pp.212-224.

Gautheron, C., Tassan-Got, L., Barbarand, J. and Pagel, M., 2009. Effect of alpha-damage annealing on apatite (U–Th)/He thermochronology. Chemical Geology, 266(3), pp.157-170.

Gautheron, C., Tassan-Got, L., Ketcham, R.A. and Dobson, K.J., 2012. Accounting for long alpha-particle stopping distances in (U–Th–Sm)/He geochronology: 3D modeling of diffusion, zoning, implantation, and abrasion. Geochimica et Cosmochimica Acta, 96, pp.44-56.

Geiser, P. and Engelder, T., 1983. The distribution of layer parallel shortening fabrics in the Appalachian foreland of New York and 'Pennsylvania: Evidence for two non-coaxial phases of the Alleghanian orogeny. Geological Society of America Memoirs, 158, pp.161-176.

Ghiglione, M.C., Navarrete-Rodríguez, A.T., González-Guillot, M. and Bujalesky, G., 2013. The opening of the Magellan Strait and its geodynamic implications. Terra Nova, 25(1), pp.13-20.

Ghiglione, M.C., Ramos, V.A., Cuitiño, J. and Barberón, V., 2016. Growth of the Southern Patagonian Andes (46–53 S) and Their Relation to Subduction Processes. In Growth of the Southern Andes (pp. 201-240). Springer International Publishing.

Giacosa, R., Zubia, M., Sánchez, M. and Allard, J., 2010. Meso-Cenozoic tectonics of the southern Patagonian foreland: Structural evolution and implications for Au–Ag veins in

the eastern Deseado Region (Santa Cruz, Argentina). Journal of South American Earth Sciences, 30(3), pp.134-150.

Giacosa, R.E. and Heredia, N., 2004. Estructura de los Andes Nordpatagónicos en los cordones Piltriquitrón y Serrucho y en el valle de El Bolsón (41º 30-42 º 00 S), Río Negro. Revista de la Asociación Geológica Argentina, 59(1), pp.91-102.

Giacosa, R.E. and Heredia, N., 2004. Structure of the North Patagonian thick-skinned fold-and-thrust belt, southern central Andes, Argentina (41–42 S). Journal of South American Earth Sciences, 18(1), pp.61-72.

Giacosa, R.E., Afonso, J.C., Heredia, N. and Paredes, J., 2005. Tertiary tectonics of the sub-Andean region of the North Patagonian Andes, southern central Andes of Argentina (41–42 30' S). Journal of South American Earth Sciences, 20(3), pp.157-170.

Gianni, G., Folguera, A., Navarrete, C., Encinas, A. and Echaurren, A., 2016. The North Patagonian Orogen: Meso-Cenozoic Evolution from the Andes to the Foreland Area. In Growth of the Southern Andes (pp. 173-200). Springer International Publishing.

Gianni, G., Navarrete, C., Orts, D., Tobal, J., Folguera, A. and Giménez, M., 2015a. Patagonian broken foreland and related synorogenic rifting: The origin of the Chubut Group Basin. Tectonophysics, 649, pp.81-99.

Gianni, G.M., Navarrete, C.G. and Folguera, A., 2015b. Synorogenic foreland rifts and transtensional basins: A review of Andean imprints on the evolution of the San Jorge Gulf, Salta Group and Taubaté Basins. Journal of South American Earth Sciences, 64, pp.288-306.

Gibbs, A.D., 1983. Balanced cross-section construction from seismic sections in areas of extensional tectonics. Journal of structural geology, 5(2), pp.153-160.

Gleadow, A.J.W., 1981. Fission-track dating methods: what are the real alternatives?. Nuclear Tracks, 5(1-2), pp.3-14.

Gleadow, A.J.W., Duddy, I.R., Green, P.F. and Lovering, J.F., 1986. Confined fission track lengths in apatite: a diagnostic tool for thermal history analysis. Contributions to Mineralogy and Petrology, 94(4), pp.405-415.

Glodny, J., Echtler, H., Figueroa, O., Franz, G., Gräfe, K., Kemnitz, H., Kramer, W., Krawczyk, C., Lohrmann, J., Lucassen, F. and Melnick, D., 2006. Long-term geological

evolution and mass-flow balance of the South-Central Andes. In The Andes (pp. 401-428). Springer Berlin Heidelberg.

Godoy, E., Yáñez, G. and Vera, E., 1999. Inversion of an Oligocene volcano-tectonic basin and uplifting of its superimposed Miocene magmatic arc in the Chilean Central Andes: first seismic and gravity evidences. Tectonophysics, 306(2), pp.217-236.

Gonzales, P., Mapa Geológico de la provincia de Rio Negro, Republica Argentina, escala1:750,000,Serv. Geol.,Buenos Aires,1994.

González Díaz, E.F., 1979. La edad de la Formación Ventana, en el área al norte y al este del Lago Nahuel Huapi. Revista de la Asociación Geológica Argentina, 34(2), pp.113-124.

Gordon, A. and Ort, M.H., 1993. Edad y correlación del plutonismo subcordillerano en las provincias de Río Negro y Chubut (41-42 30'LS). In Congreso Geológico Argentino (Vol. 12, pp. 120-127).

Green, A.G., Weber, W. and Hajnal, Z., 1985. Evolution of Proterozoic terrains beneath the Williston Basin. Geology, 13(9), pp.624-628.

Green, P.F., Duddy, I.R., Laslett, G.M., Hegarty, K.A., Gleadow, A.W. and Lovering, J.F., 1989. Thermal annealing of fission tracks in apatite 4. Quantitative modelling techniques and extension to geological timescales. Chemical Geology: Isotope Geoscience Section, 79(2), pp.155-182.

Gripp, A.E. and Gordon, R.G., 1990. Current plate velocities relative to the hotspots incorporating the NUVEL-1 global plate motion model. Geophysical Research Letters, 17(8), pp.1109-1112.

Groshong Jr, R.H., 2006. 3-D structural geology. Springer-Verlag Berlin Heidelberg.

Guillaume, B., Gautheron, C., Simon-Labric, T., Martinod, J., Roddaz, M. and Douville, E., 2013. Dynamic topography control on Patagonian relief evolution as inferred from low temperature thermochronology. Earth and Planetary Science Letters, 364, pp.157-167.

Guillaume, B., Martinod, J. and Espurt, N., 2009. Variations of slab dip and overriding plate tectonics during subduction: insights from analogue modelling. Tectonophysics, 463(1), pp.167-174.

Gutscher, M.A., 2002. Andean subduction styles and their effect on thermal structure and interplate coupling. Journal of South American Earth Sciences, 15(1), pp.3-10.

Gutscher, M.A., Spakman, W., Bijwaard, H. and Engdahl, E.R., 2000. Geodynamics of flat subduction: seismicity and tomographic constraints from the Andean margin. Tectonics, 19(5), pp.814-833.

Haschke, M.R., Scheuber, E., Günther, A. and Reutter, K.J., 2002. Evolutionary cycles during the Andean orogeny: repeated slab breakoff and flat subduction?. Terra nova, 14(1), pp.49-55.

Hervé, F., 1994. The southern Andes between 39 and 44 S latitude: the geological signature of a transpressive tectonic regime related to a magmatic arc. In Tectonics of the Southern Central Andes (pp. 243-248). Springer Berlin Heidelberg.

Holdsworth, R.E., Handa, M., Miller, J.A. and Buick, I.S., 2001. Continental reactivation and reworking: an introduction. Geological Society, London, Special Publications, 184(1), pp.1-12.

Homovc, J., Navarrete, C., Marshall, P., Masquere, S. and Cerdan, J., 2011. Inversión tectónica intra-cretácica de la Subcuenca de Río Mayo, Chubut, Argentina. In 18th Congreso Geológico Argentino, Neuquén. Abstract Book (pp. 1418-1419).

Humphreys, E., 2009. Relation of flat subduction to magmatism and deformation in the western United States. Geological Society of America Memoirs, 204, pp.85-98.

Hurford, A.J. and Green, P.F., 1982. A users' guide to fission track dating calibration. Earth and Planetary Science Letters, 59(2), pp.343-354.

Hurford, A.J. and Green, P.F., 1983. The zeta age calibration of fission-track dating. Chemical Geology, 41, pp.285-317.

Hurford, A.J., 1990. Standardization of fission track dating calibration: Recommendation by the Fission Track Working Group of the IUGS Subcommission on Geochronology. Chemical Geology: Isotope Geoscience Section, 80(2), pp.171-178.

James, D.E., 1971. Plate tectonic model for the evolution of the Central Andes. Geological Society of America Bulletin, 82(12), pp.3325-3346.

Jordan, T.E., Burns, W.M., Veiga, R., Pángaro, F., Copeland, P., Kelley, S. and Mpodozis, C., 2001. Extension and basin formation in the southern Andes caused by increased convergence rate: A mid-Cenozoic trigger for the Andes. Tectonics, 20(3), pp.308-324.

Jordan, T.E., Isacks, B., Ramos, V.A. and Allmendinger, R.W., 1983. Mountain building in the Central Andes. Episodes, 3, pp.20-26.

Jordan, T.E., Zeitler, P., Ramos, V. and Gleadow, A.J.W., 1989. Thermochronometric data on the development of the basement peneplain in the Sierras Pampeanas, Argentina. Journal of South American Earth Sciences, 2(3), pp.207-222.

Kay, S.M. and Coira, B.L., 2009. Shallowing and steepening subduction zones, continental lithospheric loss, magmatism, and crustal flow under the Central Andean Altiplano-Puna Plateau. Geological Society of America Memoirs, 204, pp.229-259.

Keetley, J.T. and Hill, K.C., 2000. 3D structural modeling of the Kutubu oilfields, Papua New Guinea. In American Association of Petroleum Geologists International Conference and Exhibition; Abstracts (Vol. 84, p. 1446).

Kendrick, E.C., Bevis, M., Smalley, R.F., Cifuentes, O. and Galban, F., 1999. Current rates of convergence across the central Andes: Estimates from continuous GPS observations. Geophysical Research Letters, 26(5), pp.541-544.

Ketcham, R.A., 2005. Forward and inverse modeling of low-temperature thermochronometry data. Reviews in mineralogy and geochemistry, 58(1), pp.275-314.

Ketcham, R.A., Carter, A., Donelick, R.A., Barbarand, J. and Hurford, A.J., 2007. Improved measurement of fission-track annealing in apatite using c-axis projection. American Mineralogist, 92(5-6), pp.789-798.

Ketcham, R.A., Donelick, R.A. and Carlson, W.D., 1999. Variability of apatite fission-track annealing kinetics: III. Extrapolation to geological time scales. American Mineralogist, 84(9), pp.1235-1255.

Ketcham, R.A., Gautheron, C. and Tassan-Got, L., 2011. Accounting for long alpha-particle stopping distances in (U–Th–Sm)/He geochronology: Refinement of the baseline case. Geochimica et Cosmochimica Acta, 75(24), pp.7779-7791.

Ketcham, R.A., Mora, A., Almendral, A., Parra, M., Casallas, W., and Robles, W., 2013. Integrative interpretation of thermochronometric data: Application to inversion tectonic settings. AAPG Search and Discovery Article 41233.

Kley, J., Monaldi, C.R. and Salfity, J.A., 1999. Along-strike segmentation of the Andean foreland: causes and consequences. Tectonophysics, 301(1), pp.75-94.

Kraml, M., Pik, R., Rahn, M., Selbekk, R., Carignan, J. and Keller, J., 2006. A New Multi-Mineral Age Reference Material for 40Ar/39Ar,(U-Th)/He and Fission Track Dating Methods: The Limberg t3 Tuff. Geostandards and Geoanalytical Research, 30(2), pp.73-86.

Lacombe, O. and Mouthereau, F., 2002. Basement-involved shortening and deep detachment tectonics in forelands of orogens: Insights from recent collision belts (Taiwan, Western Alps, Pyrenees). Tectonics, 21(4).

Lagabrielle, Y., Suárez, M., Rossello, E.A., Hérail, G., Martinod, J., Régnier, M. and de la Cruz, R., 2004. Neogene to Quaternary tectonic evolution of the Patagonian Andes at the latitude of the Chile Triple Junction. Tectonophysics, 385(1), pp.211-241.

Lavenu, A. and Cembrano, J., 1999. Compressional-and transpressional-stress pattern for Pliocene and Quaternary brittle deformation in fore arc and intra-arc zones (Andes of Central and Southern Chile). Journal of Structural Geology, 21(12), pp.1669-1691.

Lesta, P. and Ferello, R., 1972. Región extraandina de Chubut y norte de Santa Cruz. Geología Regional Argentina, 2, pp.602-687.

Lizuain, A., 1995. Mapa Geológico de la Provincia del Chubut, República Argentina. Secretaría de Minería, Dirección Nacional del Servicio Geológico, Buenos Aires, Scale 1:750 000.

Lizuaín, A., 2009, Hoja 4372–II, Esquel. Escala 1: 250.000, Provincia del Chubut: Instituto de Geología y Recursos Minerales, Servicio Geológico Minero Argentino.

Lizuaín, A., 2009. Hoja 4372–II, Esquel. Escala 1: 250.000, Provincia del Chubut: Instituto de Geología y Recursos Minerales, Servicio Geológico Minero Argentino.

Lizuaín, A., and D. Silva Nieto (2011), Hoja 4369-I, Gastre. Escala 1: 250.000, Provincia del Chubut: Instituto de Geología y Recursos Minerales,Servicio Geológico Minero Argentino.

Maloney, K.T., Clarke, G.L., Klepeis, K.A. and Quevedo, L., 2013. The Late Jurassic to present evolution of the Andean margin: Drivers and the geological record. Tectonics, 32(5), pp.1049-1065.

Mancini, D., and M. Serna (1989), Evaluación petrolera de la Cuenca de Ñirihuau. Sudoeste de Argentina, in 1th Congreso Nacional de Exploración de Hidrocarburos (Argentina), pp. 739–762, Buenos Aires.

Mancktelow, N.S. and Grasemann, B., 1997. Time-dependent effects of heat advection and topography on cooling histories during erosion. Tectonophysics, 270(3), pp.167-195.

Marrett, R. and Allmendinger, R.W., 1990. Kinematic analysis of fault-slip data. Journal of structural geology, 12(8), pp.973-986.

Marshak, S., Karlstrom, K. and Timmons, J.M., 2000. Inversion of Proterozoic extensional faults: An explanation for the pattern of Laramide and Ancestral Rockies intracratonic deformation, United States. Geology, 28(8), pp.735-738.

Martinod, J., Funiciello, F., Faccenna, C., Labanieh, S. and Regard, V., 2005. Dynamical effects of subducting ridges: insights from 3-D laboratory models. Geophysical Journal International, 163(3), pp.1137-1150.

Martinod, J., Husson, L., Roperch, P., Guillaume, B. and Espurt, N., 2010. Horizontal subduction zones, convergence velocity and the building of the Andes. Earth and Planetary Science Letters, 299(3), pp.299-309.

Massaferro, G.I., Haller, M.J., D'Orazio, M. and Alric, V.I., 2006. Sub-recent volcanism in Northern Patagonia: A tectonomagmatic approach. Journal of Volcanology and Geothermal Research, 155(3), pp.227-243.

Mazzoli, S., Vitale, S., Delmonaco, G., Guerriero, V., Margottini, C. and Spizzichino, D., 2009. 'Diffuse faulting'in the Machu Picchu granitoid pluton, Eastern Cordillera, Peru. Journal of Structural Geology, 31(11), pp.1395-1408.

Mazzoni, M.M., Kawashita, K., Harrison, S. and Aragón, E., 1991. Edades radimétricas eocenas en el borde occidental del Macizo Norpatagónico. Revista de la Asociación Geológica Argentina, 46(1-2), pp.150-158.

McDowell, F.W., McIntosh, W.C. and Farley, K.A., 2005. A precise 40 Ar–39 Ar reference age for the Durango apatite (U–Th)/He and fission-track dating standard. Chemical Geology, 214(3), pp.249-263.

Meesters, A.G.C.A. and Dunai, T.J., 2002. Solving the production–diffusion equation for finite diffusion domains of various shapes: Part II. Application to cases with α-ejection and nonhomogeneous distribution of the source. Chemical Geology, 186(3), pp.347-363.

Mescua, J. F., Giambiagi L., and Bechis F., 2012, Reply to L.V. Dimieri and M.M. Turienzo, 2012 comment on: "Fault inversion vs. new thrust generation: A case study in the Malargüe fold-and thrust belt, Andes of Argentina" by J. F. Mescua and, L. B. Giambiagi, Journal of Structural Geology, 35 (2012) 51–63, Journal of Structural Geology, 42, 283–287.

Mitra, S. and Namson, J.S., 1989. Equal-area balancing. American Journal of Science, 289(5), pp.563-599.

Mora, A., 2015. Petroleum systems of the Eastern Cordillera, foothill basins, and associated Llanos basin: Impacts on the prediction of large scale foreland and foothill petroleum accumulations. AAPG Bulletin, 99(8), pp.1401-1406.

Morabito, E.G. and Ramos, V.A., 2012. Andean evolution of the Aluminé fold and thrust belt, Northern Patagonian Andes (38 30'–40 30' S). Journal of South American Earth Sciences, 38, pp.13-30.

Mpodozis, C. and Ramos, V., 1990. The Andes of Chile and Argentina. In Geology of the Andes and its Relation to Hydrocarbon and Energy Resources 11,Ericksen, G.E., Cañas Pinochet, M.T. and Reinemund, J.A. (Eds.) 1990.

Nelson, E.P., 1982. Post-tectonic uplift of the Cordillera Darwin orogenic core complex: evidence from fission track geochronology and closing temperature–time relationships. Journal of the Geological Society, 139(6), pp.755-761.

Orts, D.L., Folguera, A., Encinas, A., Ramos, M., Tobal, J. and Ramos, V.A., 2012. Tectonic development of the North Patagonian Andes and their related Miocene foreland basin (41° 30'-43° S). Tectonics, 31(3).

Orts, D.L., Folguera, A., Giménez, M., Ruiz, F., Vera, E.A.R. and Klinger, F.L., 2015. Cenozoic building and deformational processes in the North Patagonian Andes. Journal of Geodynamics, 86, pp.26-41.

Pankhurst, R.J., Rapela, C.W., Fanning, C.M. and Márquez, M., 2006. Gondwanide continental collision and the origin of Patagonia. Earth-Science Reviews, 76(3), pp.235-257.

Pankhurst, R.J., Weaver, S.D., Hervé, F. and Larrondo, P., 1999. Mesozoic-Cenozoic evolution of the North Patagonian batholith in Aysén, southern Chile. Journal of the Geological Society, 156(4), pp.673-694.

Pardo-Casas, F. and Molnar, P., 1987. Relative motion of the Nazca (Farallon) and South American plates since Late Cretaceous time. Tectonics, 6(3), pp.233-248.

Peyton, S.L. and Carrapa, B., 2013. An overview of low-temperature thermochronology in the Rocky Mountains and its application to petroleum system analysis.

Peyton, S.L. and Carrapa, B., 2013. An overview of low-temperature thermochronology in the Rocky Mountains and its application to petroleum system analysis.

Pfiffner, O.A. and Burkhard M., 1987. Determination of paleo-stress axes orientations from fault, twin and earthquake data. In Annales Tectonicae (Vol. 1, pp. 48-57).

Proserpio, C.A., 1978. Descripción geológica de la Hoja 42d, Gastre, Provincia del Chubut: carta geológica-económica de la República Argentina, escala 1: 200.000. Servicio Geológico Nacional.

Radic, J.P., Alvarez, P., Rojas, L., Czollak, C., Parada, R. and Ortiz, V., 2009, November. La cuenca de Valdivia como parte del sistema de antearco de la plataforma continental de Chile Central entre los 36 y los 40 S. In XII Congreso Geológico Chileno (Santiago) (pp. S10-032).

Radic, J.P., Rojas, L., Carpinelli, A. and Zurita, E., 2002. Evolución tectónica de la cuenca terciaria de Cura-Mallín, región cordillerana chileno argentina (36 30'-39 00'S). In Congreso Geológico Argentino (Vol. 15, pp. 233-241).

Ramos, M.E., Folguera, A., Fennell, L., Giménez, M., Litvak, V.D., Dzierma, Y. and Ramos, V.A., 2014. Tectonic evolution of the North Patagonian Andes from field and gravity data (39–40 S). Journal of South American Earth Sciences, 51, pp.59-75.

Ramos, M.E., Orts, D., Calatayud, F., Pazos, P.J., Folguera, A. and Ramos, V.A., 2011. Estructura, Estratigrafía y evolución tectónica de la cuenca de Ñirihuau en las nacientes del río Cushamen, Chubut. Revista de la Asociación Geológica Argentina, 68(2), pp.210-224.

Ramos, V., 1982. Las ingresiones pacíficas del Terciario en el norte de la Patagonia (Argentina). In III Congreso Geológico Chileno (Actas): Concepción, Chile, Departamento de Geociencias, Universidad de Concepción (pp. A262-A268).

Ramos, V., 1999. Plate tectonic setting of the Andean Cordillera. Episodes, 22, pp.183-190.

Ramos, V.A. and Cortés, J.M., 1984. Estructura e interpretación tectónica. Geología y Recursos Naturales de la provincia de Río Negro, 1, p.12.

Ramos, V.A. and Folguera, A., 2009. Andean flat-slab subduction through time. Geological Society, London, Special Publications, 327(1), pp.31-54.

Ramos, V.A. and Ghiglione, M.C., 2008. Tectonic evolution of the Patagonian Andes. Developments in Quaternary Sciences, 11, pp.57-71.

Ramos, V.A., 1981. Descripción Geológica de la Hoja 47 ab, Lago Fontana, Provincia Del Chubut: Carta Geológico-económica de la República Argentina, Escala 1: 200.000 (No. 183). Servicio Geológico Nacional.

Ramos, V.A., 2005. Seismic ridge subduction and topography: Foreland deformation in the Patagonian Andes. Tectonophysics, 399(1), pp.73-86.

Ramos, V.A., 2009. Anatomy and global context of the Andes: Main geologic features and the Andean orogenic cycle. Geological Society of America Memoirs, 204, pp.31-65.

Ramos, V.A., 2010. The tectonic regime along the Andes: Present-day and Mesozoic regimes. Geological Journal, 45(1), pp.2-25.

Ramos, V.A., Zapata, T., Cristallini, E., and Introcaso, A., 2004, The Andean Thrust System—Latitudinal Variations in McClay, K.R., ed., Thrust tectonics and hydrocarbon systems: AAPG Memoir vo. 82, p. 30-50.

Ramsay, J.G. and Huber, M.I., 1987. The techniques of modern structural geology: Folds and fractures (Vol. 2). Academic press, London.

Rapela, C.W. and Pankhurst, R.J., 1992. The granites of northern Patagonia and the Gastre Fault System in relation to the break-up of Gondwana. Geological Society, London, Special Publications, 68(1), pp.209-220.

Rapela, C.W., Spalletti, L.A., Merodio, J.C. and Aragón, E., 1988. Temporal evolution and spatial variation of early Tertiary volcanism in the Patagonian Andes (40 S–42 30' S). Journal of South American Earth Sciences, 1(1), pp.75-88.

Ravazzoli, I.A. and Sesana, F.L., 1977. Descripción geológica de la Hoja 41c, Río Chico. Servicio Geológico Nacional Boletín, 148, p.77.

Reiners, P.W. and Brandon, M.T., 2006. Using thermochronology to understand orogenic erosion. Annual Review of Earth and Planetary Sciences, 34, pp.419-466.

Reiners, P.W. and Farley, K.A., 2001. Influence of crystal size on apatite (U–Th)/He thermochronology: an example from the Bighorn Mountains, Wyoming. Earth and Planetary Science Letters, 188(3), pp.413-420.

Reiners, P.W., Farley, K.A. and Hickes, H.J., 2002. He diffusion and (U–Th)/He thermochronometry of zircon: initial results from Fish Canyon Tuff and Gold Butte. Tectonophysics, 349(1), pp.297-308.

Rosenau, M., Melnick, D. and Echtler, H., 2006. Kinematic constraints on intra-arc shear and strain partitioning in the southern Andes between 38 S and 42 S latitude. Tectonics, 25(4).

Sanderson, D.J., 1982. Models of strain variation in nappes and thrust sheets: a review. Tectonophysics, 88(3), pp.201-233.

Savignano, E., Mazzoli, S., Arce, M., Franchini, M., Gautheron, C., Paolini, M. and Zattin, M., 2016. (Un) Coupled thrust belt-foreland deformation in the northern Patagonian Andes: new insights from the Esquel-Gastre sector (41° 30'–43° S). Tectonics.

Scalabrino, B., Lagabrielle, Y., Malavieille, J., Dominguez, S., Melnick, D., Espinoza, F., Suarez, M. and Rossello, E., 2010. A morphotectonic analysis of central Patagonian Cordillera: Negative inversion of the Andean belt over a buried spreading center?. Tectonics, 29(2).

Scalabrino, B., Ritz, J.F. and Lagabrielle, Y., 2011. Relief inversion triggered by subduction of an active spreading ridge: evidence from glacial morphology in Central Patagonia. Terra Nova, 23(2), pp.63-69.

Shuster, D.L. and Farley, K.A., 2009. The influence of artificial radiation damage and thermal annealing on helium diffusion kinetics in apatite. Geochimica et cosmochimica acta, 73(1), pp.183-196.

Shuster, D.L., Flowers, R.M. and Farley, K.A., 2006. The influence of natural radiation damage on helium diffusion kinetics in apatite. Earth and Planetary Science Letters, 249(3), pp.148-161.

Skármeta, J. and Charrier, R., 1976. Geología del sector fronterizo de Aysén entre los 45 y 46 de latitud sur, Chile. In VI Congreso Geológico Argentino, Actas (Vol. 1, pp. 267-286).

Somoza, R. and Zaffarana, C.B., 2008. Mid-Cretaceous polar standstill of South America, motion of the Atlantic hotspots and the birth of the Andean cordillera. Earth and Planetary Science Letters, 271(1), pp.267-277.

Spalletti, L., Franzese, J., Morel, E., Zúñiga, A. and Fanning, C.M., 2010. Consideraciones acerca de la sedimentología, paleobotánica y geocronología de la formación piedra del águila (jurásico inferior, Neuquén). Revista de la Asociación Geológica Argentina, 66(3), pp.305-313.

Spalletti, L.A. and Dalla Salda, L.H., 1996. A pull apart volcanic related Tertiary basin, an example from the Patagonian Andes. Journal of South American Earth Sciences, 9(3-4), pp.197-206.

Stern, C.R., 2004. Active Andean volcanism: its geologic and tectonic setting. Revista geológica de Chile, 31(2), pp.161-206.

Stipanicic, P.N., Rodrigo, F., Baulies, O.L. and Martínez, C.G., 1968. Las formaciones presenonianas en el denominado Macizo Nordpatagónico y regiones adyacentes. Revista de la Asociación Geológica Argentina, 23(2), pp.67-98.

Stockli, D.F., 2005. Application of low-temperature thermochronometry to extensional tectonic settings. Reviews in Mineralogy and Geochemistry, 58(1), pp.411-448.

Stüwe, K., White, L. and Brown, R., 1994. The influence of eroding topography on steady-state isotherms. Application to fission track analysis. Earth and Planetary Science Letters, 124(1-4), pp.63-74.

Suárez M, De La Cruz R, Bell M, Demant A., 2009. Cretaceous slab segmentation in southwestern Gondwana. Geological Magagazine, 147, pp. 193–205.

Suárez, M. and De la Cruz, R., 2001. Jurassic to Miocene K–Ar dates from eastern central Patagonian Cordillera plutons, Chile (45–48 S). Geological Magazine, 138(1), pp.53-66.

Suárez, M., De la Cruz, R. and Bell, M., 1996. Estratigrafía de la región de Coyhaique (latitud 45-46 S), Cordillera Patagónica, Chile. In Congreso Geológico Argentino (No. 13, pp. 575-590).

Suppe, J., 1983. Geometry and kinematics of fault-bend folding. American Journal of science, 283(7), pp.684-721.

Tagami, T. and O'Sullivan, P.B., 2005. Fundamentals of fission-track thermochronology. Reviews in Mineralogy and Geochemistry, 58(1), pp.19-47.

Tavani, S. and Muñoz, J.A., 2012. Mesozoic rifting in the Basque–Cantabrian Basin (Spain): Inherited faults, transversal structures and stress perturbation. Terra Nova, 24(1), pp.70-76.

Tavani, S., Storti, F., Lacombe, O., Corradetti, A., Muñoz, J.A. and Mazzoli, S., 2015. A review of deformation pattern templates in foreland basin systems and fold-and-thrust belts: Implications for the state of stress in the frontal regions of thrust wedges. Earth-Science Reviews, 141, pp.82-104.

Thomson, S.N. and Hervé, F., 2002. New time constraints for the age of metamorphism at the ancestral Pacific Gondwana margin of southern Chile (42-52 S). Revista geológica de Chile, 29(2), pp.255-271.

Thomson, S.N., 2002. Late Cenozoic geomorphic and tectonic evolution of the Patagonian Andes between latitudes 42 S and 46 S: An appraisal based on fission-track results from the transpressional intra-arc Liquiñe-Ofqui fault zone. Geological Society of America Bulletin, 114(9), pp.1159-1173.

Thomson, S.N., Brandon, M.T., Tomkin, J.H., Reiners, P.W., Vásquez, C. and Wilson, N.J., 2010. Glaciation as a destructive and constructive control on mountain building. Nature, 467(7313), pp.313-317.

Thomson, S.N., Hervé, F. and Stöckhert, B., 2001. Mesozoic-Cenozoic denudation history of the Patagonian Andes (southern Chile) and its correlation to different subduction processes. Tectonics, 20(5), pp.693-711.

Vargas Easton, G., Klinger, Y., Rockwell, T.K., Forman, S.L., Rebolledo, S., Lacassin, R. and Armijo, R., 2013, December. Potential for a large earthquake rupture of the San Ramón fault in Santiago, Chile. In AGU Fall Meeting Abstracts.

Vargas, G., Rebolledo, S., Sepúlveda, S.A., Lahsen, A., Thiele, R., Townley, B., Padilla, C., Rauld, R., Herrera, M.J. and Lara, M., 2013. Submarine earthquake rupture, active faulting and volcanism along the major Liquiñe-Ofqui Fault Zone and implications for seismic hazard assessment in the Patagonian Andes. Andean Geology, 40(1).

Volkheimer, W., 1964. Estratigrafía de la zona extraandina del Departamento de Cushamen (Chubut). Revista de la Asociación Geológica Argentina, 19(2), pp.85-107.

Von Gosen, W. and Loske, W., 2004. Tectonic history of the Calcatapul Formation, Chubut province, Argentina, and the "Gastre fault system". Journal of South American Earth Sciences, 18(1), pp.73-88.

Von Gosen, W., 2009. Stages of Late Palaeozoic deformation and intrusive activity in the western part of the North Patagonian Massif (southern Argentina) and their geotectonic implications. Geological Magazine, 146(1), pp.48-71.

Wagner, G.A., 1988. Apatite fission-track geochrono-thermometer to 60 C: projected length studies. Chemical Geology: Isotope Geoscience section, 72(2), pp.145-153.

Wagner, G.A., Michalski, I. and Zaun, P., 1989. Apatite fission track dating of the Central European basement. Postvariscan thermo-tectonic evolution. In The German Continental Deep Drilling Program (KTB) (pp. 481-500). Springer, Berlin, Heidelberg.

Wallace, R.E., 1951. Geometry of shearing stress and relation to faulting. The journal of Geology, 59(2), pp.118-130.

Williams, D., K.(2010), Geology and Mineralization of the Navidad Ag-Pb-Cu-Zn District, Chubut Province, Argentina. Econ. Geol. Bull. Soc. Inc. Spec. Pub, 15, pp.203-227.

Willner, A.P., Glodny, J., Gerya, T.V., Godoy, E. and Massonne, H.J., 2004. A counterclockwise PTt path of high-pressure/low-temperature rocks from the Coastal

Cordillera accretionary complex of south-central Chile: constraints for the earliest stage of subduction mass flow. Lithos, 75(3), pp.283-310.

Windhausen, A., 1931. Geología Argentina. Casa Jacabo Peuser.

Withjack, M.O. and Peterson, E.T., 1993. Prediction of normal-fault geometries--a sensitivity analysis. AAPG Bulletin, 77(11), pp.1860-1873.

Wolf, R.A., Farley, K.A. and Kass, D.M., 1998. Modeling of the temperature sensitivity of the apatite (U–Th)/He thermochronometer. Chemical Geology, 148(1), pp.105-114.

Woodward, N.B., Gray, D.R. and Spears, D.B., 1986. Including strain data in balanced cross-sections. Journal of Structural Geology, 8(3-4), pp.313-324.

Ziegler, P.A., 1987. Late Cretaceous and Cenozoic intra-plate compressional deformations in the Alpine foreland—a geodynamic model. Tectonophysics, 137(1-4), pp.389-420.

Ziegler, P.A., Cloetingh, S. and van Wees, J.D., 1995. Dynamics of intra-plate compressional deformation: the Alpine foreland and other examples. Tectonophysics, 252(1), pp.7-59.